ABSTRACT

Title of dissertation: DIRECT MEASUREMENT OF THE W BOSON DECAY WIDTH IN PROTON-ANTIPROTON COLLISIONS AT $\sqrt{s}$=1.96 TeV

Junjie Zhu, Doctor of Philosophy, 2004

Dissertation directed by: Professors Nicholas J. Hadley and Sarah C. Eno
Department of Physics

This dissertation describes a direct measurement of the W boson total decay width, Γ_W, using the DØ detector at the Fermilab Tevatron Collider. The measurement uses an integrated luminosity of 177.3 pb^{-1} data, collected during the 2002-2003 run. The width is determined from the shape of the transverse mass distribution, M_T, by fitting the data in the tail region $100 < M_T < 200$ GeV. The result is $\Gamma_W = 2.011 \pm 0.093$ (stat) $\pm$ 0.107 (syst) GeV.

Direct Measurement of the W Boson Decay Width in Proton-Antiproton Collisions at $\sqrt{s}$=1.96 TeV

by

Junjie Zhu

Dissertation submitted to the Faculty of the Graduate School of the
University of Maryland, College Park in partial fulfillment
of the requirements for the degree of
Doctor of Philosophy
2004

Advisory Commmittee:

Professor Nicholas J. Hadley, Chair/Advisor
Professor Sarah C. Eno, Co-Advisor
Assistant Professor Kara Hoffman
Associate Professor Markus A. Luty
Professor Alice C. Mignerey

© Copyright by
Junjie Zhu
2004

To my parents, sister and Qiong

ACKNOWLEDGMENTS

Now it is the right time to thank all the people who have helped me and made my graduate experience so colorful during the last four years!

First of all I would like to thank my two advisors Sarah Eno and Nick Hadley, they are the best advisors I have known so far! The doors of their offices are always open to me, they always took the time to listen to whatever I needed to discuss and allowed me a lot of freedom in my research. Their vast knowledge, deep insights, ability to approach problems from different perspectives and tremendous experience were laid out in front of me to learn from, and I did my best to not let such unique opportunity pass by. I really feel very lucky to have worked with them for the past four years!

I am very proud to share the office with Marco Verzocchi during the past two years, Marco has taught me so much and been like a third advisor to me at Fermilab. Anything I did not understand, I could always turn to him for help, and he always could use the simplest words to explain to me. His knowledge was always astounding to me. Thank you again, Marco!

At Maryland group, I met numerous other people whose help has been indispensable: Drew Baden, Chad Jarvis, Terry Toole, Lei Wang, Matt Wetstein and Ming Yan, thank you all for discussing problems we have at every Monday's group meeting.

There are many people in the DØ collaboration who contributed to this work directly and indirectly, to mention them all would take way too much space, and I have therefore included the current DØ author list in Appendix C. During my two years at Fermilab, I have had the privilege of working with and learing from Volker Buescher, Pierre Petroff, Dean Schamberger and Robert Zitoun. I hope I have contributed half as much to them as they have helped me.

I would also like to thank all members in EB026 (Ela Barberis, Oana Boeriu, Marcel Demarteau, Neeti Parashar and Taka Yasuda) for reading my analysis note, correcting spelling and grammar,

offering insights and hints.

During the two years I spent at Fermilab I met and work with many people, I would particularly like to thank Mike Arov, Douglas Chapin, Silke Duensing, Harald Fox, John Gardner, Ashish Kumar, Sean Mattingly, Heidi Schellman, George Steinbruck, Paul Telford, Kirti Ranjan, Terry Wyatt and all other peoples in DØ EMID group, Electroweak group, W mass group, and Calorimeter Algorithm group. Thank you to everyone who has helped me and answered my questions along the way.

I was also fortunate to get to know a lot of friends at Maryland and at Fermilab, which make life more enjoyable. Rather than mentioning all of them, I would like to thank them all and give special mention to: Tor Chattrapiban, Yung-Fu Chen, Xuefeng Hua, Min-Young Kim, Sheung Wah Ng, Hanhee Paik, Hui Wang, Lixin Wang (Maryland); Huishi Dong, Shaohua Fu, Mingcheng Gao, Chunhui Han, Liang Han, Yuan Hu, Jundong Huang, Yi Jiang, Chunhui Luo, Qichun Xu, Zhongming Wang and Xiaojian Zhang (Fermilab), even though most of them have left DØ, I still remember the lunch meeting and the Chinese Graduate Student Meeting we held every week. Thank you all for your friendship!

I am grateful to have my parents and my younger sister that always supporting and encouraging me to do what I wanted to do. I cannot express how lucky I feel to have found Qiong, the best girl I have ever met in my college, thank you for every moment we have during the past six years and for the years to come!

It is impossible to remember all, and I apologize to those I have inadvertently left out. Lastly, thank you all for your help and for making my graduate experience so wonderful that I will cherish forever!

TABLE OF CONTENTS

List of Tables x

List of Figures xi

1 Introduction and Theory 1

1.1 The Standard Model 1

1.2 W and Z Bosons 3

1.2.1 W/Z in the Standard Model 3

1.2.2 W/Z Boson Production 7

1.2.3 W/Z Boson Decay 10

1.2.4 Generated Quantities for $W \to e\nu$ and $Z \to ee$ Events 11

1.3 Theoretical Predictions of W/Z Production Cross Sections, Masses and Decay Widths 13

1.3.1 W/Z Boson Production Cross Sections time Branching Ratio 13

1.3.2 W/Z Boson Masses 14

1.3.3 W/Z Boson Decay Widths 15

1.4 W Boson Transverse Mass 17

1.5 Measurements of the W Boson Width 18

1.5.1 Indirect Measurement of Γ_W 19

1.5.2 Direct Measurement of Γ_W 19

2 Fermilab Accelerator and DØ Detector 22

2.1 The Accelerator 22

2.2 DØ Detector 24

2.2.1 The DØ Coordinate System 25

2.2.2 Tracking System 27

2.2.3 Preshower Detectors 29

2.2.4 Calorimeters 30

2.2.5 Muon System 39

2.3 Trigger System 40

3 Event Selection 43

3.1 Data Set 43

3.2 Trigger Selection 44

3.3 Track and Vertex Reconstruction 47

3.4 Electron Identification 47

3.5 Neutrino Identification 50

3.6 Offline Selection Criteria 51

3.6.1 $Z \to ee$ Selection Criteria 51

3.6.2 $W \to e\nu$ Selection Criteria 53

4 Efficiencies, Fake Rate and Backgrounds 55

4.1 Efficiencies 55

4.1.1 Trigger Efficiency 56

4.1.2 Preselection Efficiency 56

4.1.3 HMatrix7 Efficiency 57

4.1.4 Track Matching Efficiency 58

4.2 Fake Rate 58

4.3 $Z \to ee$ Backgrounds 59

4.3.1 QCD Backgrounds 60

4.3.2 $Z \to \tau\tau$ Backgrounds 60

4.4 $W \to e\nu$ Backgrounds 60

4.4.1 QCD Backgrounds 61

4.4.2 $Z \to ee$ Backgrounds 61

4.4.3 $W \to \tau\nu$ Backgrounds 62

5 Overview of Monte Carlo Simulation 63

5.1 EM Objects Simulation 63

5.2 Recoil System Simulation 64

6 Electron Measurement and Simulation 66

6.1 Electron Energy Measurement 66

6.1.1 Pedestal subtration and zero-suppression 67

6.1.2 ADC - GeV Conversion 69

6.1.3 Sampling Weights 72

6.1.4 Clustering Algorithm 72

6.1.5 Geometrical Corrections 73

6.1.6 EM Scale Calibration 73

6.2 Determination of Electron Energy Scale 74

6.2.1 Binned Maximum Likelihood Method 74

6.2.2 $< M_{ee} >$ Method 75

6.2.3 Kolmogorov-Smirnov Test 77

6.2.4 Final Results for EM Energy Scale and Energy Offset 78

6.3 Determination of Electron Energy Resolution 78

6.3.1 Binned Maximum Likelihood Method 78

6.3.2 Z Width Method 79

6.3.3 Final Results for EM Energy Resolution 80

6.4 Consistency Check of Electron Energy Simulation using E/p 81

6.5 Determination of Calorimeter Position Resolution 83

6.6 Radiative Decay 83

6.7 Electron Simulation Results 84

7 Recoil Measurement and Simulation 86

7.1 Hadronic Momentum Response 86

7.2 Hadronic Energy Resolution 88

7.3 $u_{\parallel}$ Efficiency 88

7.4 Underlying Event Contribution 91

7.5 $u_{\parallel}$ Correction 93

7.6 Recoil System Simulation Results 94

8 Fitting 104

8.1 Maximum Likelihood 104

8.2 Reweighting 104

8.3 Fitting 105

8.4 Systematic Uncertainties 106

9 Consistency Checks 115

9.1 Ratio Fit 115

9.2 Electron p_T and $\not{E}_T$ Spectra 115

9.3 Dependence on Fitting Region 115

9.4 Dependence on p_T^W Cut 116

9.5 Dependence on Fitting Function 117

9.6 Dependence on Instantaneous Luminosity 117

9.7 Dependence on Calorimeter non-linearity 118

9.8 Dependence on Calorimeter non-uniformity 119

10 Conclusions and Future Prospects 131

A Discussion about the Constant Term 134

A.1 Electronics Noise 134

A.1.1 Design Goal 134

A.1.2 Electronics Calibration 134

A.1.3 Coherent Noise 135

A.2 Operation and Maintenance 136

A.2.1 Liquid Argon Monitoring 137

A.2.2 Hardware Problems 137

A.3 Clustering Algorithms and T42 138

A.4 Offline Calibration 140

A.4.1 Calorimeter non-uniformity and ϕ intercalibration 140

A.5 Preshower Detectors 140

B E/p Simulation 143

C DØ Author List 147

Bibliography 154

LIST OF TABLES

1.1 Fundamental forces and gauge bosons. 2

1.2 Three generations of elementary particles. 2

2.1 Central Calorimeter Module Parameters. 36

2.2 End Calorimeter Module Parameters. IFH, ICH, MFH, MCH, OH stand for inner fine hadronic, inner coarse hadronic, middle fine hadronic, middle coarse hadronic and outer hadronic section respectively. UNb and SS stand for Uranium-Niobium alloy and Stainless Steel. 37

3.1 Single EM triggers used in this analysis. 45

3.2 L1/L2/L3 requirements for each of the Single EM triggers used in this analysis. . . 46

6.1 Sampling weights for the four EM layers and the first fine hadronic layer. 72

7.1 $u_{\|}$ Efficiency. 91

8.1 Uncertainties on the W Width Measurement for the fitting region $100 < M_T < 200$ GeV. 113

8.2 Uncertainties on the W Width Measurement for the two fitting regions $90 < M_T < 200$ GeV and $110 < M_T < 200$ GeV. 114

A.1 Electronics Noise Performance. 135

B.1 Energy dependence of the size of the tail of E/p spectrum relative to its peak. . . 145

LIST OF FIGURES

1.1 Elementary particles. The lepton and quark families are shown as well as the force carrying bosons. Mass increases with generation number. 3

1.2 Lowest order Feynman diagrams for Z and W^+ boson production. 7

1.3 Initial state gluon radiation and Compton scattering in W^+ production. 9

1.4 Initial state gluon radiation and Compton scattering in Z production. 9

1.5 Illustration of spin states for W^+ production and decay. The left plot is for a W^+ produced with valence quarks, and the right plot is for W^+ produced with sea quarks. 11

1.6 Generated quantities for MC $W \to e\nu$ events. Top Left: W boson transverse mass M_T; Top Right: W boson p_T; Bottom Left: electron p_T (Line) and neutrino p_T (Dots); Bottom Right: electron pseudorapidity. 12

1.7 Generated quantities for MC $Z \to ee$ events. Top Left: Z boson invariant mass; Top Right: Z boson p_T; Bottom Left: electron p_T; Bottom Right: electron pseudorapidity. 13

1.8 Possible decay channels for Z and W bosons within the SM. 14

1.9 Feynman diagrams for 1-loop corrections to the W propagator. 15

1.10 M_H as a function of M_t and M_W. 16

1.11 M_T (Left) and $p_T(e)$ (Right) spectra for W bosons with $p_T^W = 0$ (solid line), with the correct p_T^W (points), and with detector resolutions (shaded area). 19

1.12 Transverse mass spectra from Monte Carlo simulation with different W widths, normalized to some arbitrary number. The triangles are for $\Gamma_W = 1.6$ GeV, the dots are for $\Gamma_W = 2.1$ GeV and the circles are for $\Gamma_W = 2.6$ GeV. 20

2.1 The general layout of the collider facility at Fermilab. 23

2.2 Tevatron bunch scheme for Run I (top) and Run II (bottom). 24

2.3 A view of the DØ Run II upgraded detector. 26

2.4 Cross-sectional view of the DØ tracking volume. 27

2.5 DØ Run II Silicon Microstrip Tracker detector. 28

2.6 (a) A quarter r - z view of the CFT detector showing the nested eight barrel design. (b) A magnified r - ϕ end view of the two doublet layer configuration for two different barrels. 29

2.7 Cross-sectional end view (left) and side view (right) of the Central Preshower Detector. 30

2.8 One quarter view of the Forward Preshower Detector. 31

2.9 Overall view of the calorimeter system. 32

2.10 Side-view of one quarter of the DØ calorimeter system, showing segmentation and tower definitions. The line extending from the center of the detector denote the pseudorapidity coverage of cells and projected towers. 33

2.11 Calorimeter channel configuration in terms of depth and η. 34

2.12 Schematic view of a representative calorimeter unit cell. The gap structure, grounded absorber plates, and signal boards are shown. 35

2.13 Schematic of the primary elements for the DØ calorimeter electronics. 37

2.14 Electronics signal shape from the calorimeter cell, after the preamplifier and after the shaper. 38

2.15 Channel hierarchy for the DØ calorimeter electronics. 39

2.16 Summary of the three-level DØ trigger system for Run II with the decision time and bandwidth allocated to each level. 41

2.17 L1 and L2 trigger data pathway. The arrow indicates the direction of data flow. . . 42

3.1 Integrated luminosity delivered by the Tevatron Collider and recorded by the DØ detector. 44

3.2 Invariant mass distribution of $Z \to ee$ candidates. 52

3.3 Transverse mass distribution of $W \to e\nu$ candidates. 54

4.1 Trigger efficiency vs electron p_T. 56

4.2 Preselection efficiency vs electron detector eta. 57

4.3 HMatrix7 efficiency vs electron detector eta. 57

4.4 Track Matching efficiency vs electron detector eta. 58

4.5 Fake track matching probability vs $\not{E}_T$ for both CC and EC region. 59

4.6 Fake track matching probability vs electron pseudorapidity. 60

4.7 Concept of the method used to subtract QCD backgrounds from $W \to e\nu$ events. . 62

6.1 Energy distribution of a typical calorimeter cell for a sample of minimum bias events. The mean pedestal has been subtracted and the events in the empty region are removed by the zero suppression (2.5 σ). 69

6.2 Schematic diagrams of a) the calibration system and b) the pulser system. 70

6.3 ADC response to the calibration signal (DAC). The noise multiplied by 100 is indicated by crosses. 71

6.4 Residual of data with respect to a straight line fit for a cell in the EM calorimeter, circles are $\times 1$ gain, crosses the $\times 8$ gain channel. 71

6.5 Electron Energy Scale vs likelihood. 75

6.6 Electron Energy Offset vs likelihood. 75

6.7 Electron Energy Scale vs $< M_{ee} >$. 76

6.8 Electron Energy Offset vs $< M_{ee} >$. 76

6.9 Integrated distribution of M_{ee} for data and MC, dashed line for data, solid line for MC. 77

6.10 Electron Energy Scale vs KS value. 78

6.11 Electron Energy Offset vs KS value. 79

6.12 Constant Term vs likelihood. 79

6.13 The observed invariant mass distribution for CC-CC Z candidates fitted with a Breit-Wigner convoluted with a Gaussian function. 80

6.14 Constant Term vs Z Boson Width. 81

6.15 E/p distribution for W events (Dots for data, line for the Monte Carlo simulation (Top: linear scale; Bottom: log scale). 82

6.16 Invariant Mass distribution for $Z \to ee$ events (Dots for data, line for MC). 84

6.17 Electron p_T distribution for $Z \to ee$ events (Dots for data, line for MC). 84

6.18 p_T^Z for $Z \to ee$ events (Dots for data, line for MC). 85

7.1 Definition of η and ξ axis for $Z \to ee$ events. 87

7.2 Average $\vec{p}_T^{\,rec} \bullet \hat{\eta}$ versus $\vec{p}_T^{\,ee} \bullet \hat{\eta}$ for $Z \to ee$ events, the line is a linear fit (Left); Average $\hat{\eta}$ imbalance versus $\vec{p}_T^{\,ee} \bullet \hat{\eta}$ for $Z \to ee$ events, the line is a linear fit. (Right) 88

7.3 Distribution of the average $|\vec{p}_T^{\,e1} + \vec{p}_T^{\,e2} + \not{E}_T|^2$ versus $|\vec{p}_T^{\,ee}|^2$ for $Z \to ee$ events, the line is a linear fit. 89

7.4 Definition of $u_\parallel$ and $u_\perp$ for $W \to e\nu$ events. 90

7.5 Average isolation f_{iso} versus $u_\parallel$ for signal electrons from W decays. 90

7.6 Distribution of the isolation quantity f_{iso} for signal electrons for different $u_\parallel$ ranges: $u_\parallel \leq -10$ GeV (Top Left), $-10 < u_\parallel \leq -5$ GeV (Top Right), $-5 < u_\parallel \leq 0$ GeV (Middle Left), $0 < u_\parallel \leq 5$ GeV (Middle Right), $5 < u_\parallel \leq 10$ GeV (Bottom Left) and $u_\parallel > 10$ GeV (Bottom Right). 92

7.7 $u_\parallel$ efficiency. 93

7.8 Instantaneous luminosity profiles for minimum bias events (line) and the W events (points). 94

7.9 x and y Component of MET distribution from minimum bias events. 95

7.10 $\not{E}_T$ distribution from minimum bias events. 95

7.11 $\not{E}_T$ vs instantaneous luminosity for minimum bias events, the line is a fit from 0.2 to 1.0, the slope is 0.61 GeV/10^{30}cm^{-2}s^{-1} and the offset is 3.5 GeV. 96

7.12 η imbalance (defined as $(\vec{p}_T^{\,ee} + \vec{p}_T^{\,rec}) \bullet \hat{\eta}$) for $Z \to ee$ events. Dots for data, line for the fast Monte Carlo simulation. 96

7.13 ξ imbalance (defined as $(\vec{p}_T^{\,ee} + \vec{p}_T^{\,rec}) \bullet \hat{\xi}$) for $Z \to ee$ events. Dots for data, line for the fast Monte Carlo simulation. 97

7.14 Determination of $u_\parallel$ correction $\Delta u_\parallel$. The curved line connecting the Monte Carlo points shows the correlation between $u_\parallel$ correction vs $N(u_\parallel > 0)/N(u_\parallel < 0)$ from Monte Carlo. The horizontal solid line shows the ratio $N(u_\parallel > 0)/N(u_\parallel < 0)$ measured from data and the horizontal dashed lines the uncertainty on $N(u_\parallel > 0)/N(u_\parallel < 0)$. From the intersection of the data line with the curved line we determin the $u_\parallel$ correction to be -1.78 ± 0.01 GeV. 97

7.15 $u_\parallel$ (Top) and $u_\perp$ (Bottom) distributions for $W \to e\nu$ events (Dots for data, line for MC). 98

7.16 $\cos(\theta_e)$ for electrons from $W \to e\nu$ events (Dots for data, line for MC). 99

7.17 Azimuthal angle difference between electron and $\not{E}_T$ from $W \to e\nu$ decays from $W \to e\nu$ decays compared to the Monte Carlo simulation (Dots for data, line for MC, shadowed area for QCD background). 99

7.18 Distribution of the mean $u_\parallel$ versus p_T^e from $W \to e\nu$ decays compared to the Monte Carlo simulation (Dots for data, circles for MC, no p_T^W cut). 100

7.19 Distribution of the mean $u_\parallel$ versus p_T^ν from $W \to e\nu$ decays compared to the Monte Carlo simulation (Dots for data, circles for MC, no p_T^W cut). 100

7.20 Distribution of the mean $u_\parallel$ versus M_T from $W \to e\nu$ decays compared to the Monte Carlo simulation (Dots for data, circles for MC, no p_T^W cut). 101

7.21 Distribution of the mean $u_\parallel$ versus p_T^W from $W \to e\nu$ decays compared to the Monte Carlo simulation (Dots for data, circles for MC, no p_T^W cut). 101

7.22 Spectrum of p_T^e from W data with $u_\parallel < 0$ (dots) and $u_\parallel > 0$ (circles) compared to the Monte Carlo simulations (Solid line for $u_\parallel < 0$ and dashed line for $u_\parallel > 0$). . . 102

7.23 Spectrum of p_T^ν from W data with $u_\parallel < 0$ (dots) and $u_\parallel > 0$ (circles) compared to the Monte Carlo simulations (Solid line for $u_\parallel < 0$ and dashed line for $u_\parallel > 0$). . . 102

7.24 Spectrum of M_T from W data with $u_\parallel < 0$ (dots) and $u_\parallel > 0$ (circles) compared to the Monte Carlo simulations (Solid line for $u_\parallel < 0$ and dashed line for $u_\parallel > 0$). . . 103

8.1 Results of the maximum likelihood fit of the data to Monte Carlo templates. Monte Carlo templates are generated with Γ_W between 1.6 and 3.6 GeV at 50 MeV intervals. Each point represents a log-likelihood fit performed over the range $100 < M_T < 200$ GeV. The curve is the best fit of the likelihood points to a fourth order polynomial. The best value is 2.011 ± 0.093 GeV. 107

8.2 Top: Comparison of data to Monte Carlo templates for the transverse mass shape. The dots with error bars are data, the shadowed area is QCD background and the line corresponds to QCD + MC $W \to e\nu$ + MC $W \to \tau\nu$ with the best W width. Bottom: χ distribution for the fit to the M_T spectrum. 108

8.3 Top: Comparison of data to Monte Carlo templates for electron p_T spectrum. The dots with error bars are data, the shadowed area is QCD background and the line corresponds to QCD + MC $W \to e\nu$ + MC $W \to \tau\nu$ with the best W width. Bottom: χ distribution for the fit to the electron p_T spectrum. 109

8.4 Top: Comparison of data to Monte Carlo templates for $\not{E}_T$ spectrum. The dots with error bars are data, the shadowed area is QCD background and the line corresponds to QCD + MC $W \to e\nu$ + MC $W \to \tau\nu$ with the best W width. Bottom: χ distribution for the fit to the $\not{E}_T$ spectrum. 110

8.5 Top: Comparison of data to Monte Carlo templates for p_T^W spectrum. The dots with error bars are data, the shadowed area is QCD background and the line corresponds to QCD + MC $W \to e\nu$ + MC $W \to \tau\nu$ with the best W width. Bottom: χ distribution for the fit to the W p_T spectrum. 111

8.6 Data-MC comparison plots for M_T in [100, 200] GeV, electron p_T and $\not{E}_T$ in [50, 100] GeV. 112

9.1 The ratio checking. The dots are the ratio from MC for different W widths, the center horizontal line represents the ratio from data. The two horizontal lines are for uncertainties. The intercept of two curves give the value 2.004 ± 0.091 GeV. . . 116

9.2 Electron p_T distribution for events with $100 < M_T < 200$ GeV (Dots for data, line for the Monte Carlo simulation. For data, the electron is required to have a matched track, and no background subtraction is applied). 117

9.3 $\not{E}_T$ distribution for events with $100 < M_T < 200$ GeV (Dots for data, blue line for the Monte Carlo simulation. For data, the electron is required to have a matched track, and no background subtraction is applied). 118

9.4 Comparison of the M_T spectra between the data (point) and the Monte Carlo simulation (solid line) for data selected with $p_T^W < 5$ GeV (Top) and $5 < p_T^W < 10$ GeV (Bottom). 120

9.5 Comparison of the M_T spectra between the data (point) and the Monte Carlo simulation (solid line) for data selected with $10 < p_T^W < 15$ GeV (Top) and $15 < p_T^W < 20$ GeV (Bottom). 121

9.6 Instantaneous Luminosity distribution of the W (solid line) and the Z (blue points) samples for events where electrons with (Top) and without (Bottom) track matching requirement. 122

9.7 M_T data-MC comparisons for events with instantaneous luminosity $L \leq 0.4 \times 10^{30}$ $\mathrm{cm}^{-2}\mathrm{s}^{-1}$ (Top) and $0.4 < L \leq 0.6 \times 10^{30}$ $\mathrm{cm}^{-2}\mathrm{s}^{-1}$ (Bottom). 123

9.8 M_T data-MC comparisons for events with instantaneous luminosity $0.6 < L \leq 0.8 \times 10^{30}$ $\mathrm{cm}^{-2}\mathrm{s}^{-1}$ (Top) and $L \geq 0.8 \times 10^{30}$ $\mathrm{cm}^{-2}\mathrm{s}^{-1}$ (Bottom). 124

9.9 Variation in the fitted W width as a function of the instantaneous luminosity. . . . 125

9.10 The peak position of the $Z \to ee$ invariant mass distribution vs instantaneous luminosity. 125

9.11 The width of the fitted Gaussian for the $Z \to ee$ invariant mass distribution vs instantaneous luminosity. 126

9.12 Top: The E_T distributions of electrons from W and Z decays (Blue dots for Z electrons and red circles for W electrons). Bottom: The E/P distributions of electrons from W and Z decays (Blue dots for Z electrons and red line for W electrons). . . 127

9.13 Top: Variation of the mean of E/P with electron transverse energy in the data and the Monte Carlo simulation (Dots for data, circles for MC). Bottom: Data minus the simulation. 128

9.14 Variation in the fitted W width as a function of ϕ module (x axis is ϕ module, defined as (int)$(32 \times \phi_{det}^{elec}/2\pi)$). 129

9.15 Electron energy scale as a function of ϕ module (y axis is ϕ module, defined as (int)$(32 \times \phi_{det}^{e}/2\pi)$). 129

9.16 M_T data and the Monte Carlo comparison for one typical module (Module 18). . . 130

10.1 Comparison of this measurement with previously published direct measurements of the W boson width, the shaded region indicates the predicted W width value. . . . 133

A.1 Comparison of physical signal (the histogram with only one peak) and calibration signal (the histogram with two peaks). 136

A.2 Normalized pair-wise correlation coefficients based on pedestal ADC counts for all 4608 channels in one ADC crate. 137

A.3 η_{det} vs ϕ_{det} calorimeter plots for runs 179762 to 180956. Hollow boxes are regions cut out, blue solid boxes are inefficient cells (lightest $< 60\%$ normal, darkest $< 20\%$), orange have at least twice normal acceptance. 138

A.4 Invariant Mass distribution for $Z \to ee$ events without (Left) and with (Right) T42 algorithm. 139

A.5 E/p distribution for electrons from $W \to e\nu$ candidates for crate 2 (Top Left), crate 3 (Top Right), Crate 8 (Bottom Left) and Crate 9 (Bottom Right). Each point represents the average E/p for electrons located inside one of twelve ADC cards within one ADC crate. 141

A.6 Simulation of the improvement obtained on the electron energy resolution with the DØ calorimeter including the Central Preshower detector for electrons at $E_T = 2$ GeV. 142

B.1 M_T distributions for W events (Dots for events in peak region, line for events in low E/p region (Using calorimeter E_T) and triangles for events in low E/p region (Using tracke p_T) The histograms are normalized to the number of events with $E/p < 0.9$. 146

Chapter 1

Introduction and Theory

1.1 The Standard Model

One of the main goals of particle physics is to understand what matter is made of, and what are the forces in nature through which matter interacts. Our current understanding of the fundamental forces is contained in the description of the gravitational, the strong, the weak and the electromagnetic interactions among elementary particles. These forces are transmitted by specific fields or particles which are equivalent concepts in relativistic quantum field theory.

In the 1960s, Glashow, Salam and Weinberg unified the electromagnetic and weak interaction into the electroweak theory [1], which, together with Quantum Chromodynamics (the theory of the strong interaction), forms the Standard Model (SM) of particle physics. The SM is a quantum field theory that is based on the gauge symmetry $SU(3)_C \times SU(2)_L \times U(1)_Y$. This gauge group includes the symmetry group of the strong interactions ($SU(3)_C$), and the symmetry group of the electroweak interactions ($SU(2)_L \times U(1)_Y$). The symmetry group of the electromagnetic interactions ($U(1)_{em}$) appears in the SM as a subgroup of $SU(2)_L \times U(1)_Y$, and it is in this sense that the weak and electromagnetic interactions are unified. The SM provides a very elegant theoretical framework, and it has successfully passed very precise tests [2].

Both electroweak and QCD theories are gauge field theories, meaning that they model the forces between fermions by coupling them to bosons which mediate the forces. The Lagrangian of each set of mediating bosons is invariant under gauge transformation, so these mediating bosons are referred to as gauge bosons. The massless photon, γ, is the exchange particle in electromagnetic interactions. The eight massless gluons, g_α, mediate strong interactions among quarks, and the three massive weak bosons, $W^\pm$ and Z, are the corresponding intermediate bosons that mediate the weak interaction. Table 1.1 summarizes the fundamental forces and the properties of their

gauge bosons [3].

Force	Boson Name	Symbol	Charge ($\|e\|$)	Spin	Mass (GeV/c^2)
Strong	Gluon	g	0	1	0
Electromagnetic	Photon	γ	0	1	0
Weak	W-boson	$W^{\pm}$	± 1	1	80.423 ± 0.039
	Z-boson	Z^0	0	1	91.1876 ± 0.0021
Gravitational	Graviton	G	0	2	0

Table 1.1: Fundamental forces and gauge bosons.

Apart from the gauge bosons, there are six leptons and six quarks. The six leptons are electron, muon, tau and the corresponding neutrinos; the six quarks are up, down, charm, strange, bottom, and top quarks. These six leptons and six quarks are fermions of spin $s = \frac{1}{2}$ and can be grouped into three generations (also called families) as shown in Table 1.2. Figure 1.1 shows a picture of all matter particles and the intermediate interaction particles [4]. Why Nature chooses to repeat itself like this, and whether any more generations remain to be discovered, are still open questions.

Generation	Leptons (spin=$\frac{1}{2}$)			Quarks (spin=$\frac{1}{2}$)		
	Flavors	Charge ($\|e\|$)	Mass (MeV/c^2)	Flavors	Charge ($\|e\|$)	Mass (MeV/c^2)
1	e	-1	0.511	u	$+2/3$	$1.5 - 5$
	ν_e	0	$< 3 \times 10^{-6}$	d	$-1/3$	$3 - 9$
2	μ	-1	105.66	c	$+2/3$	$(1.0 - 1.4) \times 10^3$
	ν_μ	0	< 0.19	s	$-1/3$	$60 - 170$
3	τ	-1	1776.99 ± 0.29	t	$+2/3$	$(178.0 \pm 4.3) \times 10^3$
	ν_τ	0	< 18.2	b	$-1/3$	$(4.0 - 4.5) \times 10^3$

Table 1.2: Three generations of elementary particles.

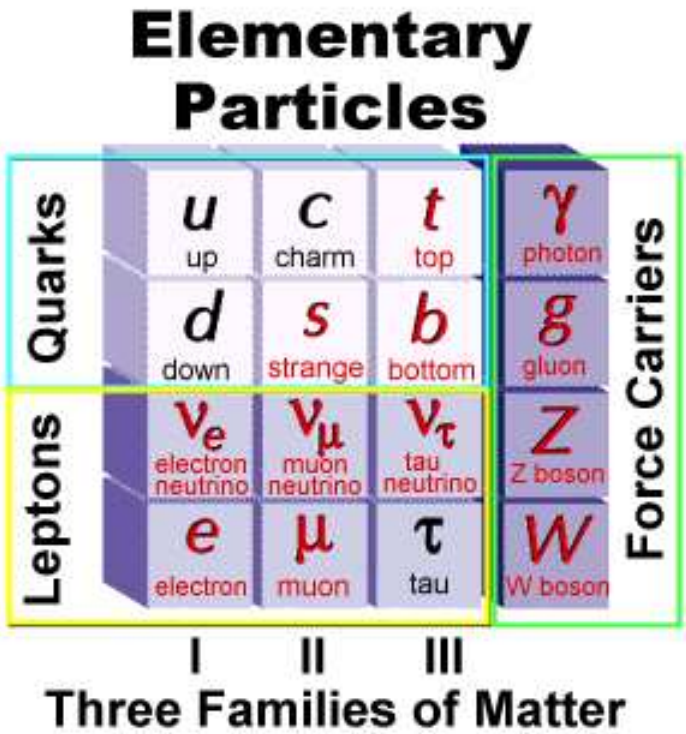

Figure 1.1: Elementary particles. The lepton and quark families are shown as well as the force carrying bosons. Mass increases with generation number.

1.2 W and Z Bosons

The W and Z bosons in the Standard Model are the quanta of local gauge fields; their properties depend only on a very few fundamental parameters. A comparison between the directly measured W and Z properties and the theoretical calculations provides therefore an excellent test of the Standard Model prediction.

1.2.1 W/Z in the Standard Model

As mentioned in Sec. 1.1, the electroweak interaction is based on an $SU(2)$ group of "weak isospin", I, and a $U(1)$ group of "weak hypercharge", Y. The Lagrangian energy density of fermions with the fields $\mathbf{W}_\mu$ and B_μ is the product of the fermion currents with the fields, that

is, of the form [5] [6]

$$L = g\mathbf{J}_\mu \bullet \mathbf{W}_\mu + g' J^Y_\mu B_\mu \tag{1.1}$$

where $\mathbf{J}_\mu$ and J^Y_μ represent respectively the isospin and hypercharge currents of the fermions, and g, g' are the couplings of fermions to $\mathbf{W}_\mu$ and B_μ. If we define the weak hypercharge as $Y = Q - I_3$, where Q is the electric charge and I_3 the third component of weak isospin, then the corresponding relation among the currents is

$$J^Y_\mu = J^{em}_\mu - J^{(3)}_\mu \tag{1.2}$$

where J^{em}_μ is the electromagnetic current, coupling to the charge Q, and $J^{(3)}_\mu$ is the third component of the isospin current $\mathbf{J}_\mu$.

The Lagrangian is thus

$$\begin{aligned} L &= g\mathbf{J}_\mu \bullet \mathbf{W}_\mu + g' J^Y_\mu B_\mu & (1.3)\\ &= g(J^{(1)}_\mu W^{(1)}_\mu + J^{(2)}_\mu W^{(2)}_\mu) + g(J^{(3)}_\mu W^{(3)}_\mu) + g'(J^{em}_\mu - J^{(3)}_\mu)B_\mu & (1.4) \end{aligned}$$

where $W^{(i)}_\mu$, $i = 1, 2, 3$, are the weak bosons of the $SU(2)_L$ group, and B_μ is the hypercharge boson of the $U(1)_Y$ group. The physical bosons consist of the charged particles $W^\pm_\mu$ and the neutrals Z_μ and A_μ, the latter are taken as linear combinations of $W^{(3)}_\mu$ and B_μ. Thus, if we set

$$W^\pm_\mu = \frac{1}{\sqrt{2}}(W^{(1)}_\mu + iW^{(2)}_\mu) \tag{1.5}$$

and

$$W^{(3)}_\mu = \frac{gZ_\mu + g'A_\mu}{\sqrt{g^2 + g'^{\,2}}} \tag{1.6}$$

$$B_\mu = \frac{-g'Z_\mu + gA_\mu}{\sqrt{g^2 + g'^{\,2}}} \tag{1.7}$$

then

$$\begin{aligned} L &= (g/\sqrt{2})(J^-_\mu W^+_\mu + J^+_\mu W^-_\mu) + J^{(3)}_\mu(gW^{(3)}_\mu - g'B_\mu) + J^{em}_\mu g' B_\mu & (1.8)\\ &= \frac{g}{\sqrt{2}}(J^-_\mu W^+_\mu + J^+_\mu W^-_\mu) + \frac{g}{\cos\theta_W}(J^{(3)}_\mu - \sin^2\theta_W J^{em}_\mu)Z_\mu + g\sin\theta_W J^{em}_\mu A_\mu & (1.9)\\ &= L_{CC} + L_{NC} + L_{em} & (1.10) \end{aligned}$$

where $J_\mu^\pm = J_\mu^{(1)} \pm iJ_\mu^{(2)}$ and $g'/g = \tan\theta_W$.

This equation shows that the interaction contains the weak charge-changing current ($L_{CC} = \frac{g}{\sqrt{2}}(J_\mu^- W_\mu^+ + J_\mu^+ W_\mu^-)$), a weak neutral current ($L_{NC} = \frac{g}{\cos\theta_W}(J_\mu^{(3)} - \sin^2\theta_W J_\mu^{em})Z_\mu$), and the electromagnetic current ($L_{em} = g\sin\theta_W J_\mu^{em} A_\mu$), for which we know the coupling to be e. Hence

$$e = g\sin\theta_W \tag{1.11}$$

The angle θ_W is called the weak mixing angle (or Weinberg angle).

As we know, the weak charged current interaction is parity-violating, and connects, for example, the left-handed (LH) states of neutrino and electron. On the other hand the electromagnetic interaction is parity-conserving and involves both LH and RH states of the electron. Hence we have to assign the lepton states to a LH doublet and a RH singlet, as follows (here we just consider the case of the first generation leptons: electron and electron neutrino)

$$R_e = (e)_R \tag{1.12}$$

$$L_e = \begin{pmatrix} \nu_e \\ e^- \end{pmatrix}_L$$

where the LH and RH components of a field ψ are defined by

$$\psi_R = \frac{1-\gamma_5}{2}\psi \tag{1.13}$$

$$\psi_L = \frac{1+\gamma_5}{2}\psi \tag{1.14}$$

here γ_5 is the chirality operator. The charged currents are thus defined as

$$J_\mu^+ = \bar{\nu}\gamma_\mu \frac{1+\gamma_5}{2} e = \bar{\nu}_L \gamma_\mu e_L = \bar{\psi}_L \gamma_\mu \tau^+ \psi_L \tag{1.15}$$

and

$$J_\mu^- = \bar{e}\gamma_\mu \frac{1+\gamma_5}{2} \nu = \bar{e}_L \gamma_\mu \nu_L = \bar{\psi}_L \gamma_\mu \tau^- \psi_L \tag{1.16}$$

where $\tau^\pm = \tau_1 \pm \tau_2$ are the Pauli operators suitable for describing $I = 1/2$ systems, γ_μ are Dirac matrices. The neutral current will be

$$J_\mu^{(3)} = \bar{\psi}_L \gamma_\mu \tau_3 \psi_L = \bar{\psi}\gamma_\mu \frac{1+\gamma_5}{2} I_3 \psi = \frac{1}{2}(\bar{\nu}_L \gamma_\mu \nu_L - \bar{e}_L \gamma_\mu e_L) \tag{1.17}$$

In $V-A$ theory, the charged current matrix element is [7]

$$|M| = \frac{G}{\sqrt{2}}[\bar{e}\gamma_\mu(1+\gamma_5)\nu][\bar{\nu}\gamma_\mu(1+\gamma_5)e] \tag{1.18}$$

where G is the Fermi coupling constant. Compared with the expressions 1.10, 1.15 and 1.16, in the limit of $q^2 \ll M_W^2$, we have

$$|M| = \left(\frac{g}{\sqrt{2}}\right)^2 \frac{1}{M_W^2}\left[\bar{e}\gamma_\mu\frac{1+\gamma_5}{2}\nu\right]\left[\bar{\nu}\gamma_\mu\frac{1+\gamma_5}{2}e\right] \tag{1.19}$$

so that

$$\frac{G}{\sqrt{2}} = \frac{g^2}{8M_W^2} \tag{1.20}$$

it follows that

$$M_W = \left(\frac{\sqrt{2}\ g^2}{8\ G}\right)^{1/2} = \left(\frac{\sqrt{2}\ e^2}{8\ G\sin^2\theta_W}\right)^{1/2} \tag{1.21}$$

Inverting the relation 1.6 and 1.7, we find

$$Z_\mu = W_\mu^{(3)}\cos\theta_W - B_\mu\sin\theta_W \tag{1.22}$$

$$A_\mu = W_\mu^{(3)}\sin\theta_W + B_\mu\cos\theta_W \tag{1.23}$$

so that, using the empirical fact that the photon is massless and orthogonal to the Z, we get

$$M_Z = \left(\frac{\sqrt{2}\ e^2}{8\ G}\right)^{1/2}\frac{1}{\sin\theta_W\cos\theta_W} = \frac{M_W}{\cos\theta_W} \tag{1.24}$$

In the electroweak model, the mass of W boson is determined thus by the fine structure constant α_{EM} $(g^2\sin^2\theta_W/4\pi)$, the Fermi coupling constant G, and Z boson mass M_Z. The standard set of measurable input parameters is the following

$$\alpha_{EM} = 1/(137.0359895 \pm 0.0000061) \tag{1.25}$$

$$G = 1.16639(\pm 0.00002)\times 10^{-5}\ \mathrm{GeV}^{-2} \tag{1.26}$$

$$M_Z = 91.1884 \pm 0.0022\ \mathrm{GeV}/c^2 \tag{1.27}$$

The fine structure constant is measured from the quantum Hall effect [8]; the Fermi coupling constant is measured from the muon lifetime ($\Gamma(\mu^- \to e^-\bar{\nu}_e\nu_\mu) = G^2 m_\mu^5/(192\pi^3)$) [8], and M_Z is measured directly by the combined experiments at the CERN e^+e^- collider LEP [9].

1.2.2 W/Z Boson Production

In $p\bar{p}$ collisions at $\sqrt{s} = 1.96$ TeV, W and Z bosons are produced predominantly through quark-antiquark annihilation. The lowest order diagrams for Z and W^+ boson production are shown in Fig. 1.2. The processes $d\bar{d} \to Z$ and $\bar{u}d \to W^-$ are similar to the ones shown. The initial state consists of two quarks with momenta q_1 and q_2. The momentum fractions, x_1, x_2, are defined as $q_1 = x_1 P_1$ and $q_2 = x_2 P_2$, where P_1 and P_2 are the momenta of the colliding proton and antiproton, respectively. The center of mass energy of the two quark system is

$$\sqrt{\hat{s}} = |q_1 + q_2| = \sqrt{x_1 x_2 s} \tag{1.28}$$

and $\sqrt{s} = 1.96$ TeV is the center of mass energy of the proton antiproton collisions at the Run II Tevatron collider.

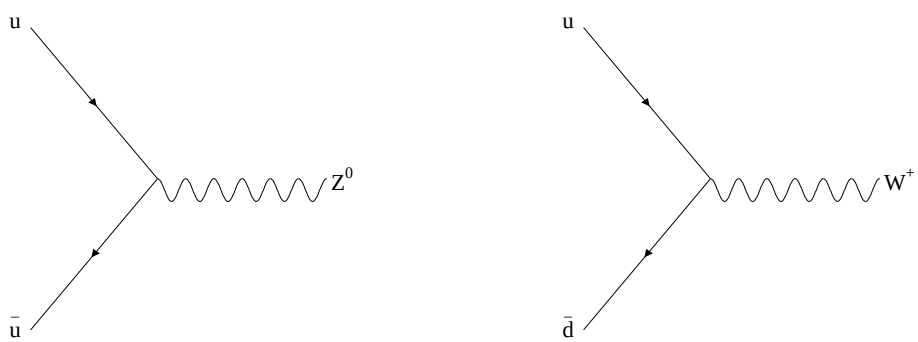

Figure 1.2: Lowest order Feynman diagrams for Z and W^+ boson production.

To predict the cross section of a process ($p\bar{p} \to V$) (V stands for either the W or the Z intermediate vector boson) at the hadron collider, one calculates the parton-level cross section $\hat{\sigma}$ as a function of the quark momenta, and then convolves with the distribution of quark momenta inside the proton and the antiproton

$$\sigma = \sum_{i,j} \int \int dx_1 dx_2 f_{i/p}(x_1, \hat{s}) f_{j/\bar{p}}(x_2, \hat{s}) \hat{\sigma}_{ij}(\hat{s}) \tag{1.29}$$

where the indices i and j run over the contributing quark flavors. The probability density functions f are called parton distribution functions (PDFs). The distributions are functions of x (the fraction of the hadron momentum carried by the parton), and of $\hat{s}$ (the energy scale of the collision).

The parton-level cross section for $q\bar{q}' \to V$ is given by

$$\hat{\sigma_{ij}}(\hat{s}) = \frac{1}{3}\frac{|V_{ij}|^2}{3\pi}\left(\frac{GM_V^2}{\sqrt{2}}\right)^2 \frac{\hat{s}\ \Gamma_V^2/M_V^2}{(\hat{s}-M_V^2)^2+(\hat{s}\Gamma_V/M_V)^2} \tag{1.30}$$

where V is the CKM matrix named after Cabibbo, Kobayashi and Maskawa that describes the quark mixing, G is the Fermi constant, and M_V and Γ_V are the mass and the total decay width of the boson respectively. The factor 1/3 in front accounts for the fact that the colliding partons must have the same color. The resonance shape is the relativistic Breit-Wigner distribution, the $\hat{s}$-dependent factor in $\hat{\sigma}$ above.

The boson is determined by its mass $\sqrt{Q^2}$, transverse momentum Q_T, rapidity y and azimuthal angle ϕ [1]. Since the proton and antiproton collide head-on, at lowest order the produced boson has no transverse momentum, and the kinematics are completely determined by x_1 and x_2:

$$Q^2 = x_1 x_2 s = \hat{s}, \qquad Q_T = 0, \qquad y = \frac{1}{2}\ln\frac{x_1}{x_2} \tag{1.31}$$

The non-zero transverse momentum of the W and Z bosons is due to the production of one or more gluons or quarks along with the bosons. Higher order processes such as Compton scattering can also produce the W and Z bosons with significant transverse momentum. The Feynman diagrams for the initial state radiation and Compton scattering are shown in Fig. 1.3 for W^+ and Fig. 1.4 for Z production. At the Tevatron, about ninety percent of the production cross section of W or Z boson is in the small transverse momentum region, where $p_T^V < 20$ GeV. In this region, multiple soft gluon emission is expected to dominate the cross section, and these soft gluons induce a large logarithmic contribution to the p_T^V distribution. Thus the order-by-order perturbative calculation in the theory of QCD does not accurately describe the p_T^V spectrum and

[1] In general, for any particle with 4-momentum (E, p_x, p_y, p_z), $Q^2 = E^2 - p_x^2 - p_y^2 - p_z^2$, $Q_T = \sqrt{p_x^2 + p_y^2}$, $y = \frac{1}{2}\ln\frac{E+p_z}{E-p_z}$ and $\phi = \arctan\frac{p_y}{p_x}$.

the contributions from multiple soft-gluon emission. A soft-gluon resummation technique [10] has been developed to predict a p_T^V distribution that agrees with experimental data. At high transverse momentum ($p_T^V > 50$ GeV), the cross section is dominated by the radiation of a single parton with large transverse momentum. The perturbative QCD calculations are therefore expected to be reliable in this regime. A prescription [11] [12] [13] has been proposed for matching the low and high p_T^V regions to provide a continuous prediction for all p_T^V.

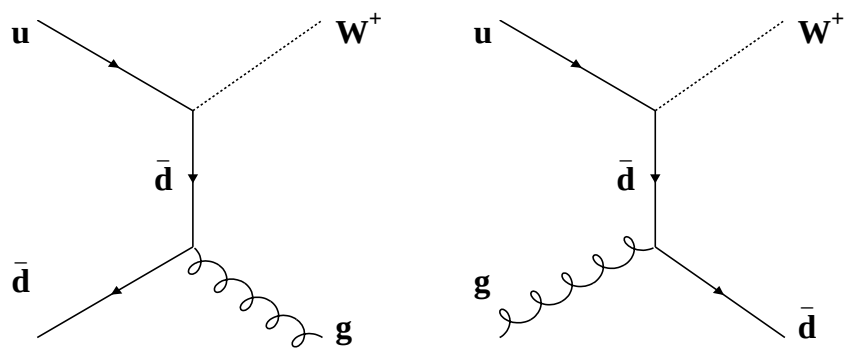

Figure 1.3: Initial state gluon radiation and Compton scattering in W^+ production.

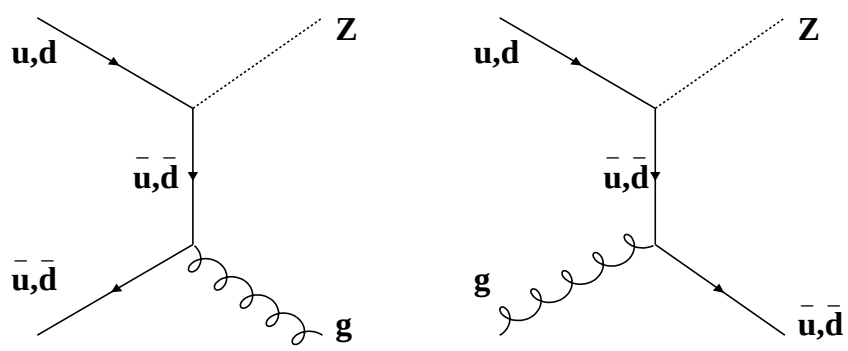

Figure 1.4: Initial state gluon radiation and Compton scattering in Z production.

1.2.3 W/Z Boson Decay

The W and Z bosons are unstable particles, and will soon decay to other stable particles once they are produced. In this dissertation we will only study the decays of the W and Z bosons to the first generation leptons. Let us first consider the two-body decay of $W \to e\nu$. In the boson rest frame, the electron and neutrino are back-to-back, and the energy of each is half the generated W mass. Given the boson 4-vector, the decay is then completely specified by fixing the polar and azimuthal angles, θ and ϕ, of either decay product in the boson rest frame.

The distribution of these angles depends on the boson polarization. The θ distribution of the electron in the W rest frame is given by the famous V-A coupling formula [14]

$$P(\theta) \propto (1 - \lambda Q \cos\theta)^2 \tag{1.32}$$

where λ is the W helicity, assumed to be ± 1 and aligned along the $p\bar{p}$ axis, Q is the W charge, and θ is the angle between the electron and the proton beam axis.

Figure 1.5 shows the spin states in W^+ production and decay [15]. A u-quark from the proton and a $\bar{d}$-quark from the antiproton interact. The spin of the quark is anti-collinear with the direction of the quark momentum (left-handed), whereas the antiquark's spin is collinear with its momentum (right-handed). Both spins are preferentially aligned in $-z$ direction. The outgoing positron is right-handed and will have its momentum preferentially pointing in the $-z$ direction which is reflected in the cross section, giving $d\sigma/d\cos\,\theta \approx (1 - \cos\,\theta)^2$, where θ is the angle with respect to the $+z$-axis.

The interaction shown in the right plot can only occur if both quarks are sea quarks from the proton and antiproton, respectively. The spins of both quarks now point in $+z$ direction which determines the direction of the spin of the positron ($+z$). The V-A coupling causes the positron to be emitted preferentially in $+z$ direction which is given in a cross section as $d\sigma/d\cos\,\theta \approx (1 + \cos\,\theta)^2$.

To correctly describe the vector boson decay, we have to consider the electroweak radiative corrections, which consist of the emission of real and virtual photons off the quarks and charged

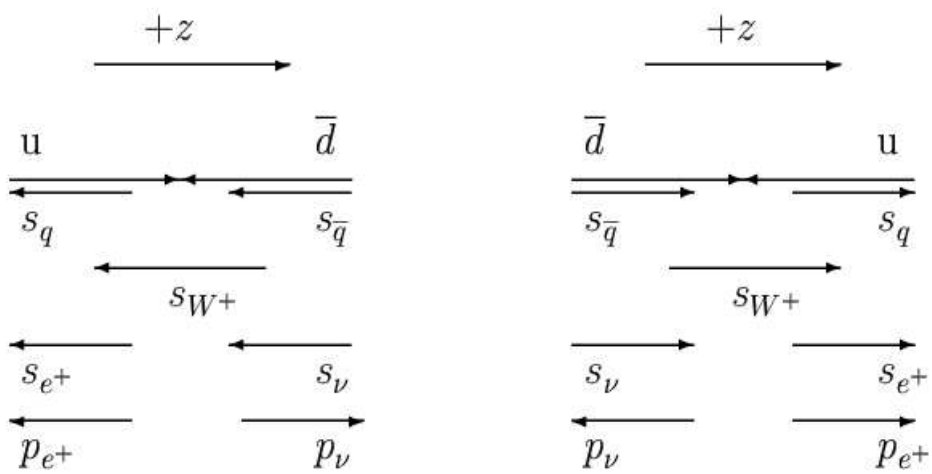

Figure 1.5: Illustration of spin states for W^+ production and decay. The left plot is for a W^+ produced with valence quarks, and the right plot is for W^+ produced with sea quarks.

leptons and the W as well. The electroweak corrections can be further divided into initial and final-state radiation. The final-state QED correction is very important, since photon emission from the charged lepton can significantly modify the lepton momentum and thus affect the transverse mass distribution. The full next-to-leading order (NLO) $O(\alpha)$ electroweak radiative corrections have been calculated in detail [17].

1.2.4 Generated Quantities for $W \to e\nu$ and $Z \to ee$ Events

In this dissertation, we use the PYTHIA event generator to generate Monte Carlo $W \to e\nu$ and $Z \to ee$ events. PYTHIA [18] is a program for the generation of high-energy physics events. It provides models for a number of the physics aspects of the interactions that are of interest to us, including hard and soft interactions, parton distributions, initial and final state parton showers, multiple interactions, fragmentation and decay.

The top plots of Fig. 1.6 show the generated transverse mass, M_T, (discussed in Sec. 1.4) and p_T distributions for the W boson. The bottom left plot shows the p_T distributions for the electron and neutrino; the electron p_T spectrum is softer than the neutrino as a result of the radiative

decay. The bottom right plot shows the pseudorapidity distribution of the electron. For all plots, no selection cuts were applied.

The top plots of Fig. 1.7 show the generated invariant mass (the mass window used here is 60 - 130 GeV) and p_T distributions for the Z boson. The bottom left plot shows the p_T distribution for the two electrons, the bottom right plot shows the pseudorapidity distribution of the two electrons. Also, no selection cuts were applied to any plot.

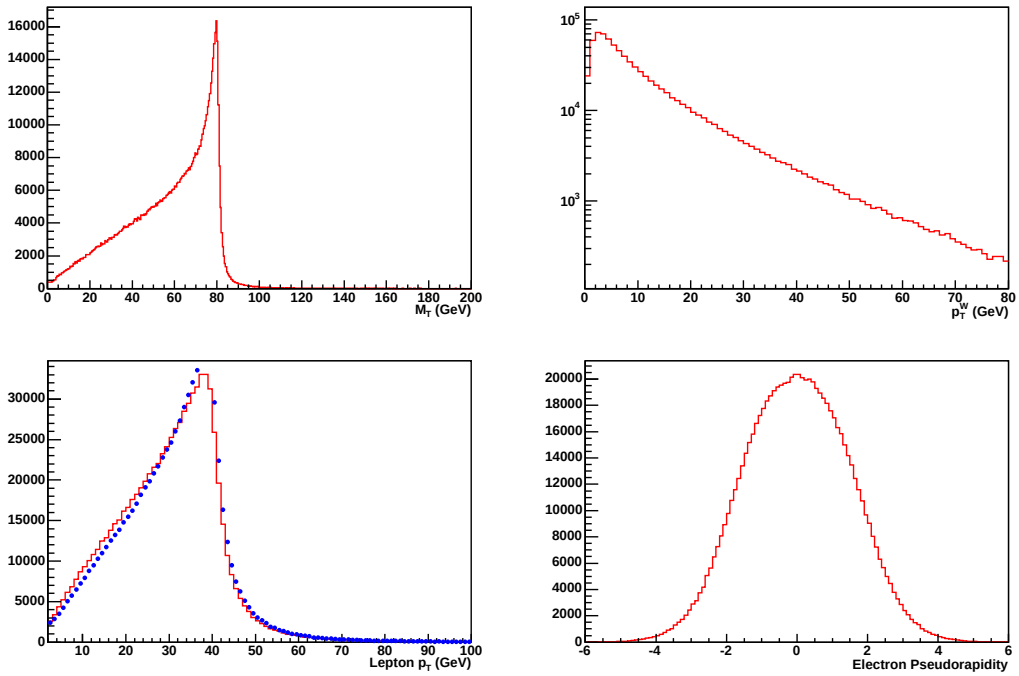

Figure 1.6: Generated quantities for MC $W \rightarrow e\nu$ events. Top Left: W boson transverse mass M_T; Top Right: W boson p_T; Bottom Left: electron p_T (Line) and neutrino p_T (Dots); Bottom Right: electron pseudorapidity.

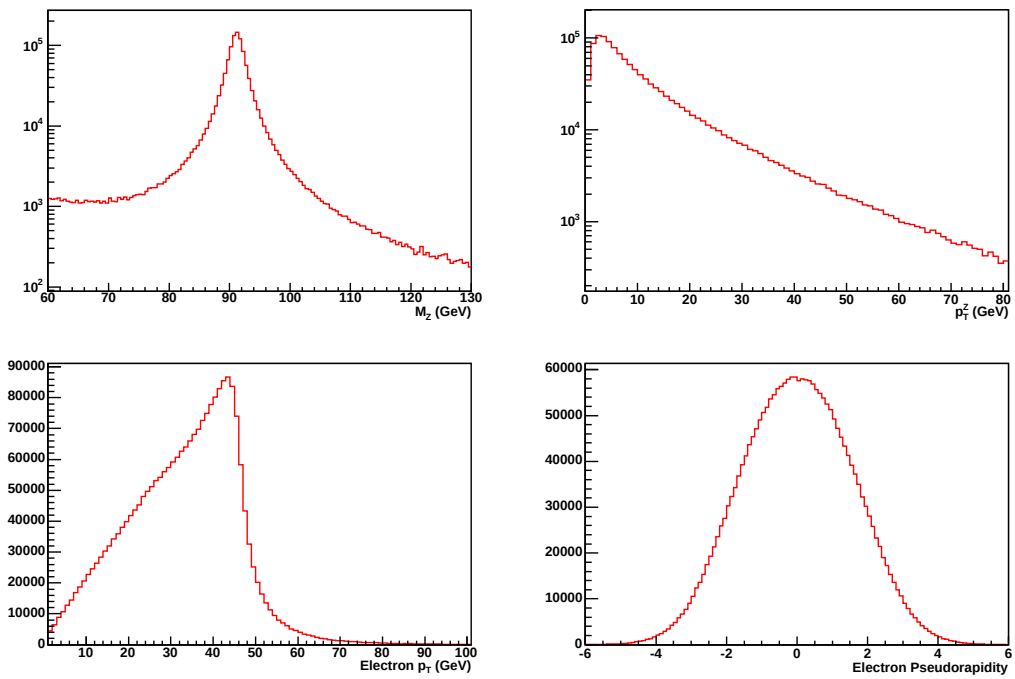

Figure 1.7: Generated quantities for MC $Z \to ee$ events. Top Left: Z boson invariant mass; Top Right: Z boson p_T; Bottom Left: electron p_T; Bottom Right: electron pseudorapidity.

1.3 Theoretical Predictions of W/Z Production Cross Sections, Masses and Decay Widths

1.3.1 W/Z Boson Production Cross Sections time Branching Ratio

The W and Z bosons can decay either into quarks or into leptons within the SM. The possible decay channels for the Z and W are shown in Fig. 1.8. The charged W boson makes a charged current transition to all leptons and all quark pairs which are allowed. $W^+ \to t\bar{b}$ and $W^- \to \bar{t}b$ are not allowed, since the top quark mass has been measured to have a mass of 178 GeV, and is heavier than the W boson. The dominant decays are clearly into quarks because they have an extra color factor which is not present in the leptonic decays. As regards branching ratios, under the universality assumption, we just have to count the final states weighted by the color factor.

This ansatz leads to the branching ratios:

$$Br(Z \to ll) \sim \frac{1}{21} = 4.8\% \qquad Br(Z \to \text{hadrons}) \sim \frac{15}{21} = 71.4\% \tag{1.33}$$

$$Br(W \to l\nu) \sim \frac{1}{9} = 11.1\% \qquad Br(W \to \text{hadrons}) \sim \frac{6}{9} = 66.7\% \tag{1.34}$$

Comparing with the latest PDG values [3]:

$$Br(Z \to ll) \sim (3.363 \pm 0.004)\% \qquad Br(Z \to \text{hadrons}) \sim (69.91 \pm 0.06)\% \tag{1.35}$$

$$Br(W \to l\nu) \sim (10.68 \pm 0.16)\% \qquad Br(W \to \text{hadrons}) \sim (67.96 \pm 0.35)\% \tag{1.36}$$

this simple calculation gives very reasonable predictions.

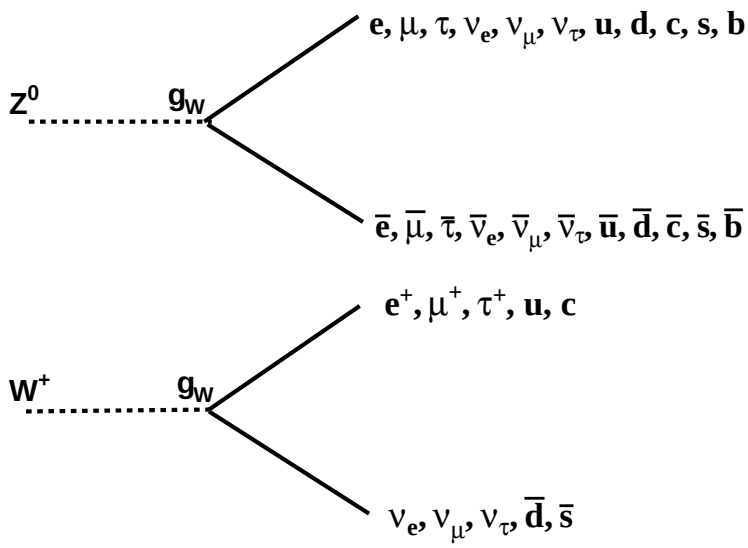

Figure 1.8: Possible decay channels for Z and W bosons within the SM.

1.3.2 W/Z Boson Masses

From section 1.2.1 we know that at lowest order, M_W and M_Z depends only on the Fermi coupling constant G, the fine structure constant α_{EM}, and the weak mixing angle θ_W. By inserting the measured values of α_{EM}, G and θ_W into equations 1.53 and 1.24, one gets the tree level values for the gauge boson masses, $M_W = 78$ GeV and $M_Z = 89$ GeV, which is very close to

the present experimental values from the LEP and Tevatron experiments:

$M_W = (80.423 \pm 0.039)$ GeV and $M_Z = (91.1876 \pm 0.0021)$ GeV [3].

Within a given scheme, loop corrections are most easily included through the use of a single measurable parameter Δr, and lead to a quadratic dependence of M_W on the top mass ($\Delta M_W \propto M_t^2 - M_b^2$), and a logarithmic dependence on the Higgs mass ($\Delta M_W \propto log M_H$). In the leading log approximation, Δr can be written in terms of M_W as [19]

$$\Delta r = 1 - \frac{\pi \alpha_{EM}/\sqrt{2}}{G M_Z^2 (M_W/M_Z)^2 [1 - (M_W/M_Z)^2]} \tag{1.37}$$

As an example, Fig. 1.9 shows the 1-loop contributions to the W propagator including the top quark and Higgs boson. Δr depends on all the masses and couplings in the theory, and also on the masses of the top quark and the Higgs particle. Figure 1.10 shows the predicted M_H as a function of M_t and M_W [20]. Precision measurement of the W mass, in conjunction with precision measurement of the top quark mass, allows tests of the Standard Model at the level of its radiative corrections.

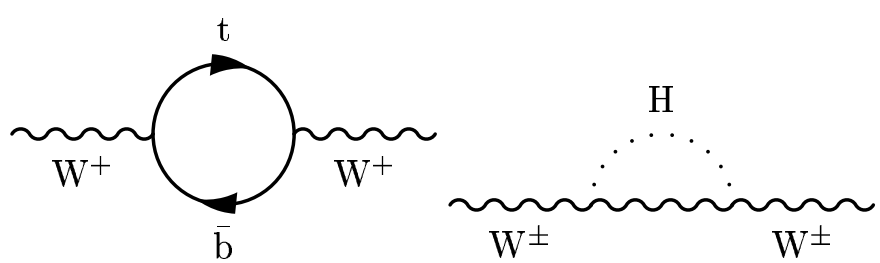

Figure 1.9: Feynman diagrams for 1-loop corrections to the W propagator.

1.3.3 W/Z Boson Decay Widths

Dimensional arguments lead us to expect that the W and Z boson decay widths are proportional to the coupling constant g_W^2 and the mass of the parent (phase space). An estimate of the width of a vector boson V is given by [21]

$$\Gamma_V \sim g_W^2 M_V \sim 1 \text{ GeV} \tag{1.38}$$

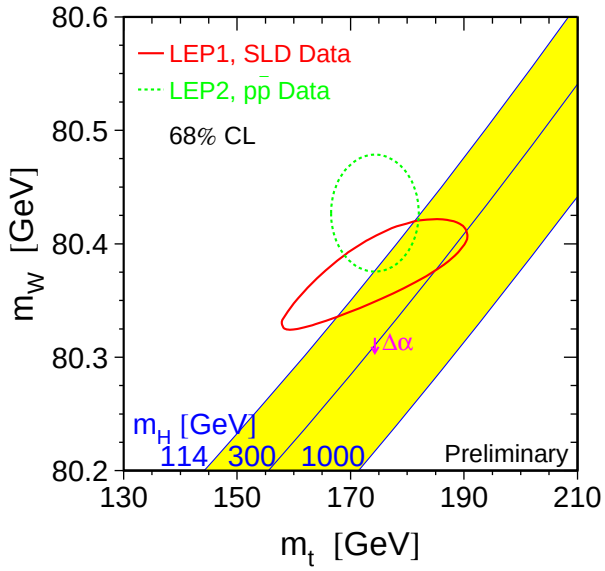

Figure 1.10: M_H as a function of M_t and M_W.

At tree level, the amplitude for $Z \to ee$ decay is

$$M = -ig_W \epsilon_\alpha e \gamma^\alpha (g_V^e + g_A^e \gamma_5) \bar{e} \tag{1.39}$$

Here g_V^e and g_A^e are the vector and axial-vector coupling strengths of the electron to the Z boson. The values are different for different type of leptons and quarks, we have [5]:

$$g_V^f = I_3^f - 2Q_f \sin^2 \theta_W \tag{1.40}$$

$$g_A^f = I_3^f \tag{1.41}$$

here I_3^f the weak isospin component of fermion f and Q_f its charge.

The exact result for the $Z \to ee$ partial width is thus calculated to be [6]

$$\Gamma(Z \to ee) = \frac{1}{48\pi}(2\sqrt{2}g_W)^2 \left(\frac{{g_V^e}^2 + {g_A^e}^2}{2} \right) M_Z = 8({g_V^e}^2 + {g_A^e}^2) \frac{GM_Z^3}{12\sqrt{2}\pi} \tag{1.42}$$

In the massless fermion approximation similar expressions hold for all $l\bar{l}$ and $q\bar{q}$ partial widths

$$\Gamma(Z \to l\bar{l}) = 8\left[(g_V^l)^2 + (g_A^l)^2\right] \frac{GM_Z^3}{12\sqrt{2}\pi} \tag{1.43}$$

$$\Gamma(Z \to q\bar{q}) = 8\left[(g_V^q)^2 + (g_A^q)^2\right] \frac{GM_Z^3}{12\sqrt{2}\pi} \tag{1.44}$$

the total Z width is

$$\Gamma_Z \approx 2.8 \text{ GeV}. \tag{1.45}$$

At tree level, the amplitude for $W^- \to e\bar{\nu}_e$ decay is

$$M = -i\frac{g_W}{\sqrt{2}}\epsilon_\alpha \bar{e}\gamma^\alpha \frac{1}{2}(1-\gamma_5)\nu \tag{1.46}$$

where ϵ_α is the polarization wave function of the W. The exact result for $W \to e\nu$ partial width is thus calculated to be [6]

$$\Gamma(W \to e\nu) = \frac{g_W^2 M_W}{48\pi} = \frac{G}{\sqrt{2}}\frac{M_W^3}{6\pi} \tag{1.47}$$

Assuming lepton universality, we have

$$\Gamma(W \to e\nu) = \Gamma(\mathrm{W} \to \mu\nu) = \Gamma(W \to \tau\nu) \tag{1.48}$$

$$\Gamma(W \to q\bar{q}') = 3\,|V_{qq'}|^2\,\Gamma(W \to e\nu) \tag{1.49}$$

where $V_{qq'}$ is the CKM matrix element. The factor of 3 in the decay rate to quarks comes from summing three colors. When experimental values for G and M_W are used, the partial width is predicted to be

$$\Gamma(W \to e\nu) = 226 \pm 1 \text{ MeV} \tag{1.50}$$

where the uncertainty is dominated by the experimental precision on M_W. The Standard Model prediction for the total decay width is thus [22]

$$\Gamma_W = 2.090 \pm 0.008 \text{ GeV} \tag{1.51}$$

The predictions of the total decay widths of the W and Z bosons agree with the current world average values $\Gamma_Z = (2.4952 \pm 0.0023)$ GeV and $\Gamma_W = 2.114 \pm 0.043$ GeV very well [3].

1.4 W Boson Transverse Mass

Since $p_z(\nu)$ cannot be measured experimentally (as discussed in Sec. 2.2.1), we cannot reconstruct the $e\nu$ invariant mass for $W \to e\nu$ candidates, and therefore must resort to other kinematic variables for the mass and the width measurement.

For recent measurements the transverse mass was used:

$$M_T(e,\nu) = \sqrt{(|\vec{p}_T^{\,e}| + |\vec{p}_T^{\,\nu}|)^2 - (\vec{p}_T^{\,e} + \vec{p}_T^{\,\nu})^2} = \sqrt{2E_T^e E_T^\nu (1 - cos(\phi_e - \phi_\nu))} \tag{1.52}$$

where E_T^e, E_T^ν are the transverse energies, $\vec{p}_T^{\,e}$, $\vec{p}_T^{\,\nu}$ are transverse momenta and ϕ_e, ϕ_ν are azimuthal angles of electron and neutrino respectively. It is analogous, in the transverse momentum subspace, to the $e\nu$ invariant mass $M(e,\nu)$

$$M_W = M(e,\nu) = \sqrt{(|\vec{p}^{\,e}| + |\vec{p}^{\,\nu}|)^2 - (\vec{p}^{\,e} + \vec{p}^{\,\nu})^2} \tag{1.53}$$

Forming the difference, we find $0 \leq M_T(e,\nu) \leq M_W$. Events with $M_T(e,\nu) > M_W$ arise due to the combination of the non-zero W width and the detector resolution.

The transverse mass has the advantage that its spectrum is relatively insensitive to the production models of the W and is unaffected by longitudinal boosts of the $e\nu$ system, since it depends only on transverse momenta. It is also insensitive to selection biases that prefer certain topologies. However, it makes use of the inferred neutrino p_T, and is therefore sensitive to the response of the detector to the recoil particles.

The electron p_T is measured with better resolution than the neutrino p_T and is insensitive to the recoil momentum measurement. However, its shape is sensitive to the motion of the W and thus requires a better understanding of the W boson production models than the M_T spectrum.

The M_T and $p_T(e)$ spectra are illustrated in Fig. 1.11, which shows the effect of the production model of the W bosons and the detector resolutions on the shape of each of the two spectra. The solid line shows the shape of the distribution before the detector simulation and with $p_T^W = 0$. The points show the shape after p_T^W is added to the system, and the shaded histogram also includes the detector simulation. We observe that the shape of the M_T spectrum is dominated by detector resolutions and the shape of the $p_T(e)$ spectrum by the motion of the W.

1.5 Measurements of the W Boson Width

Since the W total decay width Γ_W is an important parameter in the Standard Model, it has been measured repeatedly with improving precision since the discovery of W and Z bosons in 1983 [23].

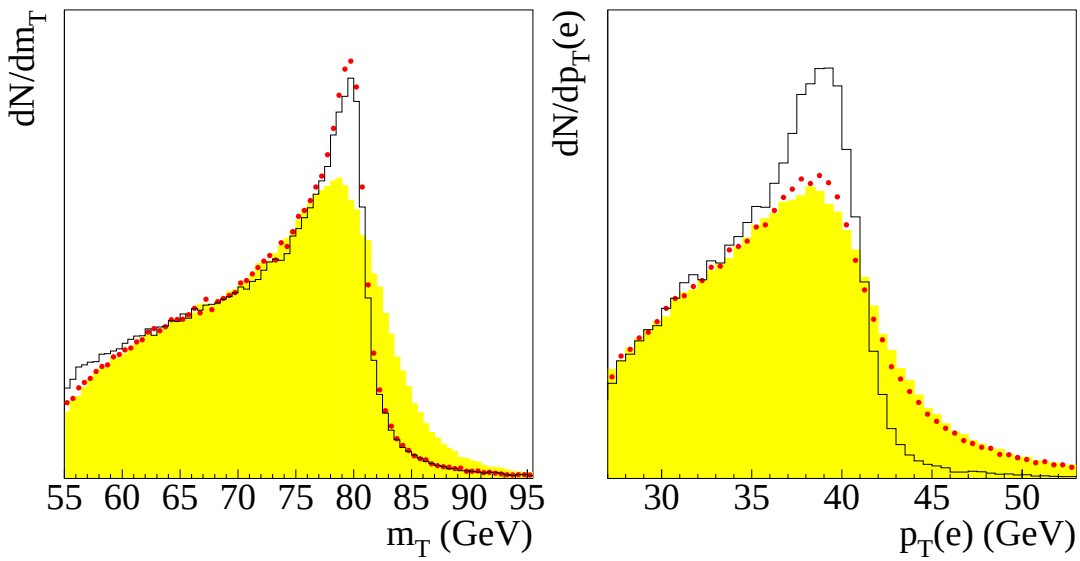

Figure 1.11: M_T (Left) and $p_T(e)$ (Right) spectra for W bosons with $p_T^W = 0$ (solid line), with the correct p_T^W (points), and with detector resolutions (shaded area).

1.5.1 Indirect Measurement of Γ_W

The W boson width has been measured indirectly using the ratio of the $W \to l\nu$ and $Z \to ll$ production cross sections:

$$R = \frac{\sigma(p\bar{p} \to W + X \to l\nu)}{\sigma(p\bar{p} \to Z + X \to ll)} = \frac{\sigma(p\bar{p} \to W + X) \times Br(W \to l\nu)}{\sigma(p\bar{p} \to Z + X) \times Br(Z \to ll)} = \frac{\sigma_W}{\sigma_Z} \times \frac{\Gamma_Z}{\Gamma_{Z\to ll}} \times \frac{\Gamma_{W\to l\nu}}{\Gamma_W} \quad (1.54)$$

Both σ_W/σ_Z and $\Gamma_{W\to l\nu}$ can be calculated theoretically to high precision, and the ratio $\Gamma_Z/\Gamma_{Z\to ll}$ has been measured precisely by experiments at the LEP collider. A precise measurement of R therefore yields a precise measurement of Γ_W.

The published CDF [24] and DØ [25] measurements of R in the electron channel are $R = 10.90 \pm 0.32(\text{stat}) \pm 0.30(\text{syst})$ (CDF) and $R = 10.82 \pm 0.41(\text{stat}) \pm 0.36(\text{syst})$ (DØ), the combined result of the decay width of W boson is $\Gamma_W = 2.141 \pm 0.057$ GeV [28].

1.5.2 Direct Measurement of Γ_W

We can make a direct measurement of the W boson width using the tail region of the transverse mass spectrum of $W \to e\nu$ events. The transverse mass distribution exhibits a Jacobian edge at

the value of M_W. Figure 1.12 shows the Monte Carlo simulated M_T spectra for different widths. At low values of M_T, all distributions look very similar and it is hard to distinguish between them, the differences show up only in the tail region, particularly in the region from 100 GeV to 200 GeV where the Breit-Wigner lineshape (width component) dominates over the Gaussian lineshape (detector resolution component). Direct measurements of the W width using the transverse mass shape have been performed by the CDF and DØ experiments, the results are: $\Gamma_W = 2.05 \pm 0.13$ GeV (CDF) [26] (electron+muon channels) and $\Gamma_W = 2.231^{+0.175}_{-0.170}$ GeV (DØ) [27] (electron channel only). The combined result is $\Gamma_W = 2.115 \pm 0.105$ GeV [28].

Direct measurements of Γ_W have also been made by measuring the W resonance lineshape in $e^+e^- \to W^+W^-$ events collected at the LEP collider, resulting in an average value $\Gamma_W = 2.150 \pm 0.091$ GeV [29].

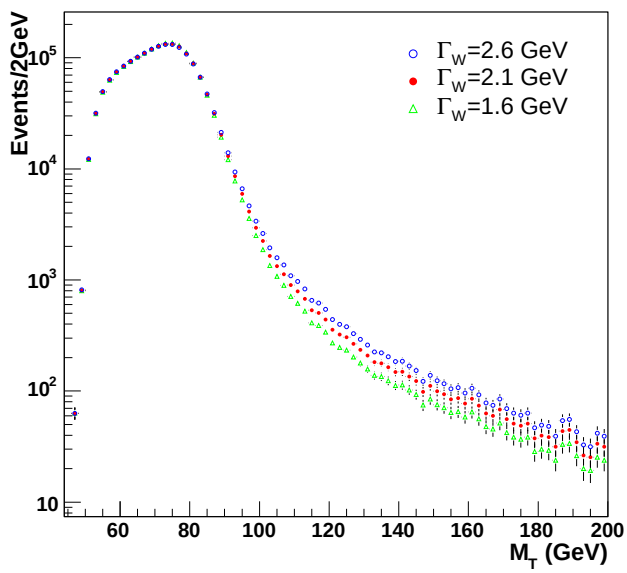

Figure 1.12: Transverse mass spectra from Monte Carlo simulation with different W widths, normalized to some arbitrary number. The triangles are for $\Gamma_W = 1.6$ GeV, the dots are for $\Gamma_W = 2.1$ GeV and the circles are for $\Gamma_W = 2.6$ GeV.

Since there is no analytic description of the transverse mass distribution observed in data, the determination of M_T relies on modeling the transverse mass spectrum through a Monte Carlo

simulation. The width, Γ_W, is extracted by comparing the measured M_T distribution in data with Monte Carlo M_T templates generated at different Γ_W, then using a binned maximum likelihood method. Obviously, the Monte Carlo simulation depends on experimental data for its parameters. $Z \to ee$ data are extensively used for the calibration of such aspects of the simulation as the determination of electron energy scale, the electron energy resolution, the hadronic momentum response, the selection efficiencies, etc. Minimum Bias events are also used in this analysis to study the contribution from underlying events.

Both the W mass and W width measurements use the transverse mass spectrum; they are thus interwined both theoretically and experimentally. However, in the W mass measurement, the mass of the W boson affects the M_T spectrum from 60 to 90 GeV, where most of the events are located. In the W width measurement, only the high M_T region is sensitive to Γ_W, due to the rapid decrease of M_T in the tail region; only a small fraction of the events (about 1%) can be used for fitting, so this analysis is dominated by statistical uncertainty.

The direct measurement of Γ_W complements the indirect measurement in several ways [30]:

- Theoretical inputs for σ_W/σ_Z and $\Gamma(W \to l\nu)$, which may be sensitive to non-SM coupling of the W boson, are not needed;
- The sources of systematic errors are different: understanding the acceptance for $ee/e\nu$ final states versus understanding the spectral shape for $e\nu$ final state;
- The direct measurement explores the region above the W boson mass pole, where possible new phenomena, such as an additional heavy vector boson (W'), can contribute;
- The sources of systematic errors in the two methods are different. The direct method is expected to ultimately be more accurate when the indirect measurement becomes limited by systematic uncertainty.

Chapter 2

Fermilab Accelerator and DØ Detector

2.1 The Accelerator

The Fermi National Accelerator Laboratory is currently the site of the world's highest center-of-mass energy proton-antiproton colliding beam accelerator, the Tevatron. It consists of several stages that increases the energy of the protons and antiprotons. Figure 2.1 shows the layout of the accelerator system. A detailed description of the Tevatron can be found at [31]. The acceleration process begins with the Pre-accelerator, or "PreAcc"; it is the source of the negatively charged hydrogen ions accelerated by the linear accelerator. It first converts hydrogen gas to ionized hydrogen gas (H^-). Next, an extractor plate accelerates the ions to a kinetic energy of 18 keV, and a Cockcroft-Walton accelerator propels the ions to an energy of 750 keV. The ions are then injected into a linear accelerator (the Linac), where they are accelerated to an energy of 400 MeV. When the ions enter the Booster, a circular synchrotron nearly half a kilometer in circumference, they are passed through a thin carbon foil which strips off the electrons, leaving a beam of H^+ ions, which are bare protons. The steady beam of protons travels around the Booster, collecting more protons with each turn. After six revolutions, the Booster contains about 3×10^{12} protons, and the Linac ceases suppling them. The Booster then restores the bunch structure to the beam and accelerates the protons to 8 GeV.

After the Booster, the protons are injected into a larger synchrotron, the Main Injector. The Main Injector is about two miles in circumference, and replaces the Main Ring that was used in Run I of the Tevatron. With the Main Injector there is a factor of three increase in the number of protons that can be delivered to the Tevatron over what was possible in Run I. The Main Injector provides a 120 GeV proton beam for the production of antiprotons, and it also accelerates protons and antiprotons from an energy of 8 GeV to an energy of 150 GeV and then

injects them into the Tevatron. The extracted 120 GeV protons are directed onto a nickel target to produce antiprotons. For every about 10^5 incident protons, one antiproton is produced. The antiprotons are produced with a wide range of momenta. They are focused and stored in the Debuncher and Accumulator rings, where the beams are cooled, creating a beam of 8 GeV antiprotons to be injected into the Main Injector, and accelerated to 150 GeV. The 150 GeV antiprotons are then injected into the Tevatron in the direction opposite to the proton beam. The Tevatron is a 4-mile circumference synchrotron ring where the beams are accelerated to 980 GeV. It contains near 1,000 superconducting magnets which operate at a temperature of 4.6 Kelvin and provide a field of 4.2 Tesla. Once protons and antiprotons are accelerated to 980 GeV, low-beta quadrupole magnets squeeze the beams to small transverse dimensions. The beams are then brought into collision at two interaction points: BØ, where the CDF detector was built and DØ, the location of the other multipurpose detector, also called DØ since it was named after its interaction point.

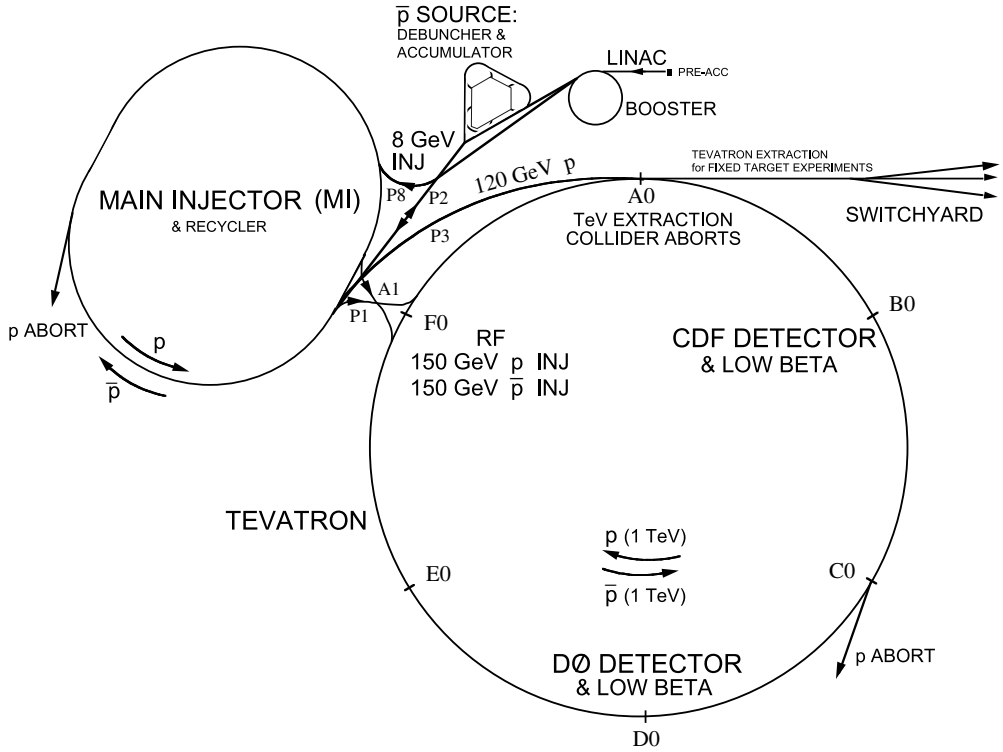

Figure 2.1: The general layout of the collider facility at Fermilab.

The bunch structure for Run I and Run II is shown in Fig. 2.2. In Run I, the accelerator delivered 6 bunches of protons and antiprotons ("6×6" bunches), separated by a 3.5 μs gap. This gap was used to form the trigger and sample the detector baselines prior to the next crossing. In Run II, the proton antiproton bunches circulate in superbunches of 4.36 μs duration, with a 2.64 μs gap spacing between them. The spacing between each bunch is 396 ns ("36×36" bunches).

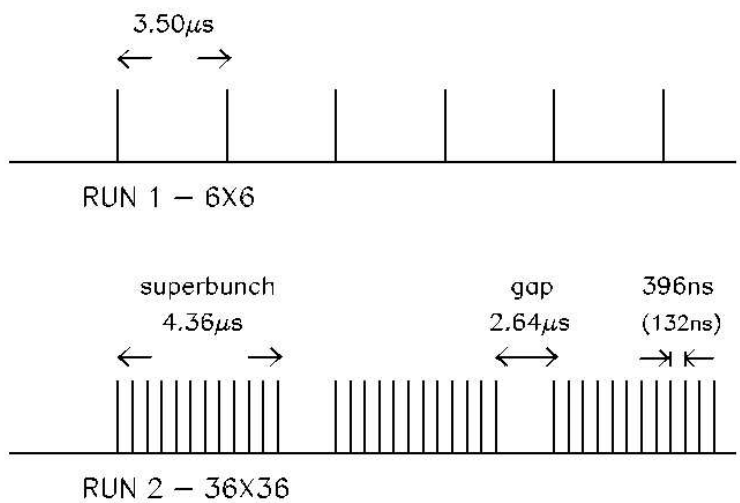

Figure 2.2: Tevatron bunch scheme for Run I (top) and Run II (bottom).

2.2 DØ Detector

The DØ detector is a multipurpose particle detector designed for the study of high mass and large transverse energy phenomena. Initial operation started in 1992 with Run I of the Tevatron accelerator; it has played a key role in experimental high energy physics [32]. One example of this was the discovery of the top quark in 1995 with the CDF detector [33].

Since the Tevatron accelerator complex has been upgraded, the instantaneous lumonosity was increased from 10^{31} cm^{-2}s^{-1} in Run I to 10^{32} cm^{-2}s^{-1} in Run II. Also the Tevatron beam energy was increased from 900 GeV to 980 GeV, increasing the $p\bar{p}$ center-of-mass collisions from 1.8 TeV to 1.96 TeV.

To take advantage of these improvements, the DØ detector went through a major upgrade. The

upgraded DØ detector consists of three major subsystems: a tracking system with superconducting solenoid magnet, a nearly 4π solid angle uranium liquid argon calorimeter with two additional preshower detectors, and a muon toroidal spectrometer. Figure 2.3 shows an overview of the entire DØ detector [34].

2.2.1 The DØ Coordinate System

The following convention for coordinates is used: the direction of the protons is the positive z direction, the positive x direction points away from the center of the Tevatron ring and thus the positive y direction points up.

In $p\bar{p}$ collisions, one can use the image that two "bags" of elementary particles (quarks, antiquarks and gluons) collide. One is usually interested in events where two of these elementary particles undergo a so-called "hard-scattering" interaction; their annihilation produces new particles at high transverse momentum. The center-of-mass system (CMS) of this hard interaction usually has a boost along the z-axis. Many of the particles produced in the collision, for example the remnants of the proton not participating in the hard-scattering interaction, escape down the beam pipe. Hence the longitudinal boost of the CMS of the hard scattering partons cannot be measured. The transverse momentum of the particles that escape down the beam pipe is negligible compared to the detector resolution, making it possible to apply conservation of energy and momentum in the transverse plane. This makes the transverse energy/momentum and the missing transverse energy ($\not{E}_T$), defined as the transverse energy imbalance, extensively used in hadron collider physics. The rapidity y of a particle (defined as $y = \frac{1}{2}\ln\left(\frac{E+p_z}{E-p_z}\right)$) is also generally used. The advantage of using rapidity is that it is invariant under the Lorentz transformation. If the energy of a particle is much larger than its mass ($m/E \to 0$), the pseudorapidity $\eta = -\log\tan(\theta/2)$ becomes a very good approximation to y (where θ is the polar angle with respect to the proton beam).

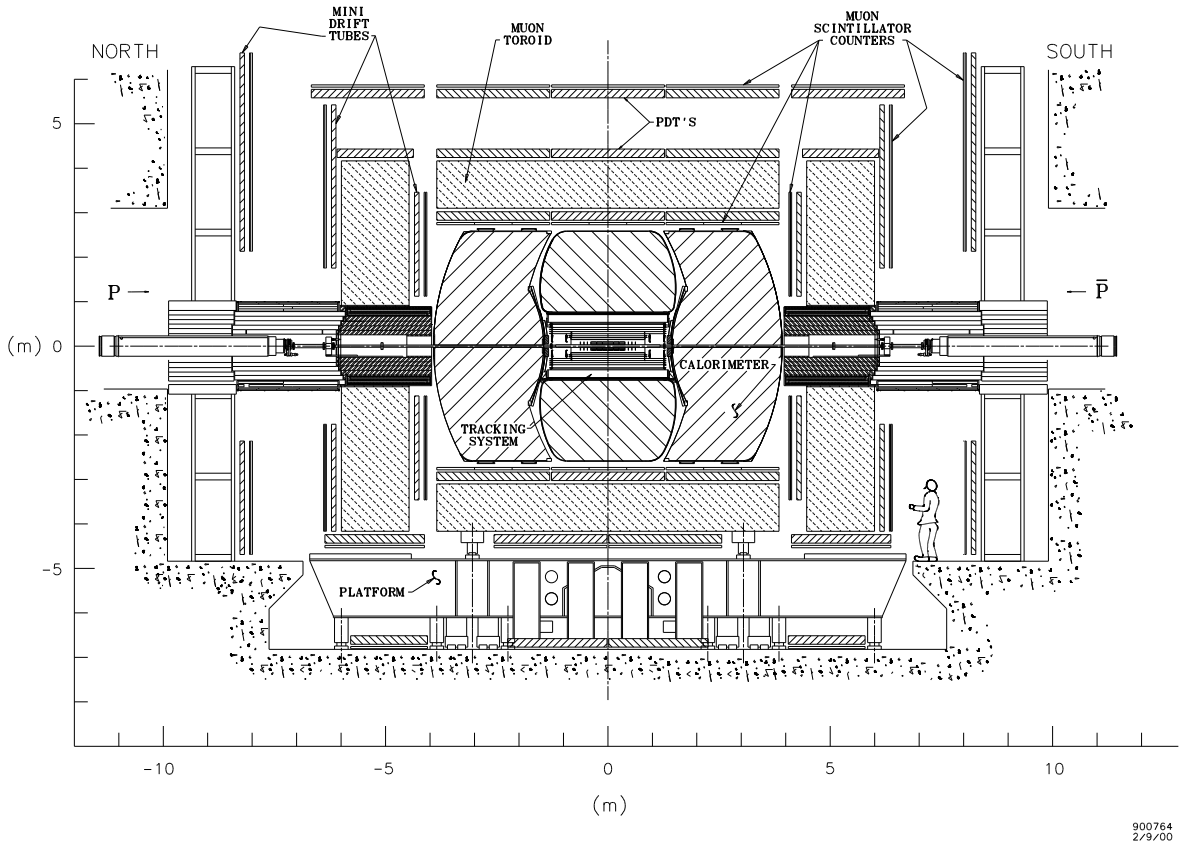

Figure 2.3: A view of the DØ Run II upgraded detector.

2.2.2 Tracking System

One of the biggest changes to the DØ detector between Run I and Run II was the addition of a new tracking system inside the calorimeter's bore. Figure 2.4 shows the various components of the inner tracking detectors in DØ. The inner detectors are surrounded by a 2 Tesla superconducting solenoid magnet, which bends the paths of charged particles with a curvature inversely proportional to their transverse momenta. Observing the curvature of a particle's path allows for a precise measurement of its momentum, as well as the sign of the particle's charge.

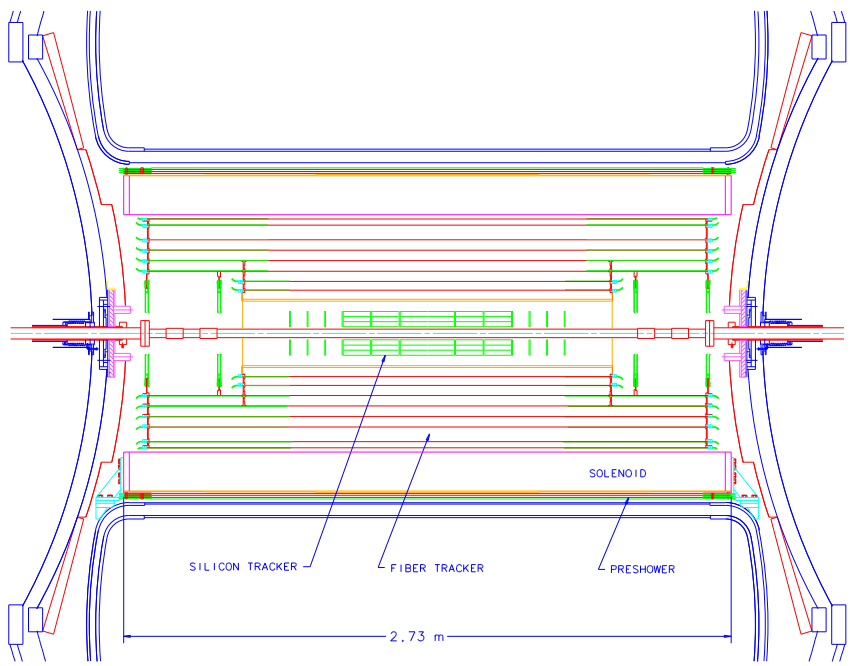

Figure 2.4: Cross-sectional view of the DØ tracking volume.

The Silicon Microstrip Tracker

The detector nearest to the interaction region is the Silicon Microstrip Tracker (SMT), which provides the high resolution position measurements of the charged particle paths that are used to reconstruct tracks and determine the vertex information [35]. Figure 2.5 shows an overview of the SMT detector. It consists of six 12 cm long barrels, with interspersed disks (12 F-disks and 4 H-disks), and has approximately 793,000 readout channels with a $r\phi$ hit resolution of

approximately 10 μm. The tracks for high η particles are reconstructed in three dimensions primarily by the disks, while particles at small η are detected primarily by the barrels.

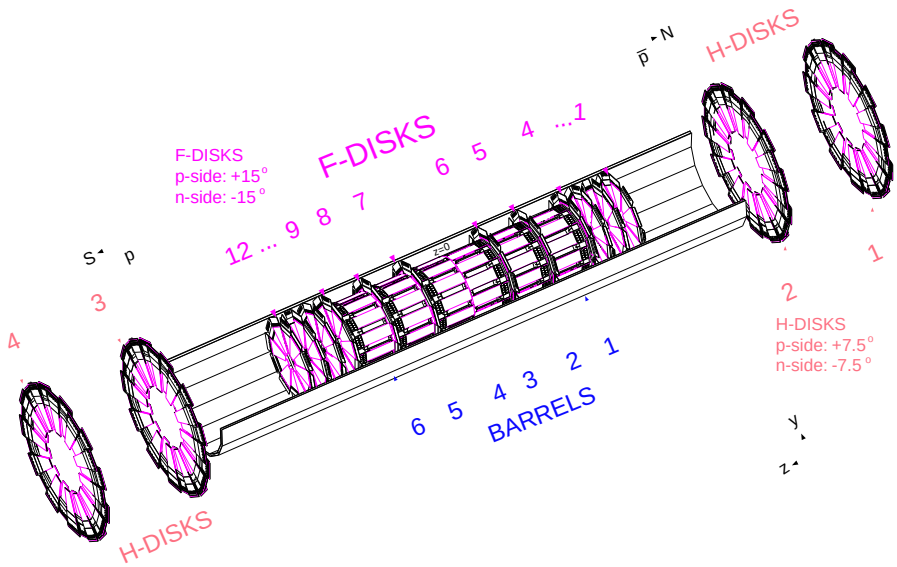

Figure 2.5: DØ Run II Silicon Microstrip Tracker detector.

The Central Fiber Tracker

Surrounding the silicon detector and extending out to the solenoid magnet, is the Central Fiber Tracker (CFT), a detector which aids the SMT in reconstruction of charged particle tracks [36]. It makes use of 76,800 scintillating fibers and can detect charged particles up to $|\eta|$ of about 2. Each ionizing particle produces an average of about 10 photons in each fiber, which are then detected using a Visible Light Photon Counter (VLPC) that converts the photons into an electrical pulse. There are 8 super-layers; each super-layer is completely covered by two doublet layers of scintillating fibers. The innermost doublet layer is mounted along the axial direction to provide the ϕ information (called the x layer), and a stereo doublet-layer is on the top to provide the η (called the u/v layer, the u layer tilts 3 degree from the z axis clockwise and the v layer tilts 3 degree counter-clockwise). Since each fiber is 835 microns in diameter, the position resolution is on the order of 100 μm, corresponding to a ϕ resolution of 2×10^{-4} radians. Figure 2.6 shows a view of the CFT as well as an illustration of the doublet layer configuration.

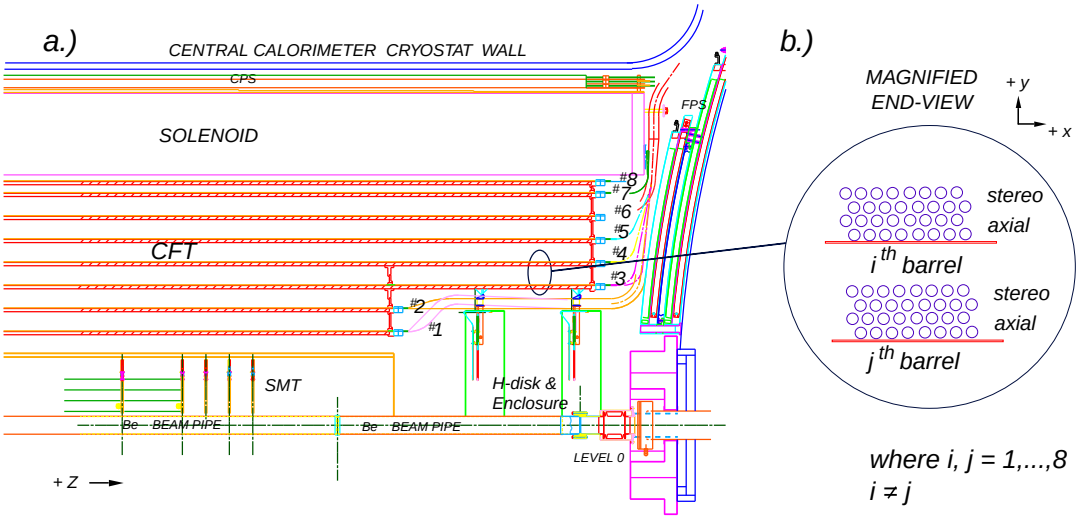

Figure 2.6: (a) A quarter r - z view of the CFT detector showing the nested eight barrel design. (b) A magnified r - ϕ end view of the two doublet layer configuration for two different barrels.

2.2.3 Preshower Detectors

There are two preshower detectors located just before the calorimeters: a central preshower covering $|\eta| < 1.3$ (CPS), and a forward preshower covering $1.5 < |\eta| < 2.5$ (FPS) (shown in Fig. 2.7 and Fig. 2.8). The primary purpose of the preshower detectors is to provide discrimination between electrons/photons and hadronic jets by exploiting the differences between their energy loss mechanisms in showers.

The detectors function as a calorimeter by providing an early energy sampling and as a tracker by providing precise position measurements. The central system [37] consists of a lead radiator of two radiation lengths thickness at $\eta = 0$, followed by three layers of scitillating material arranged in an axial, $u - v$ geometry with a 22.5^0 stereo angle. The forward system [38] also consists of a lead radiator with a thickness of two radiation lengths, sandwiched between two layers of scitillating material. Each layer is made from two thinner layers of scintillating fibers, arranged in a $u - v$ geometry with a 22.5^0 stereo angle. Electrons are recognized based on the fact that muons and charged pions traversing the radiator will only deposit energy due to ionization, while electromagnetic particles will shower in the radiator.

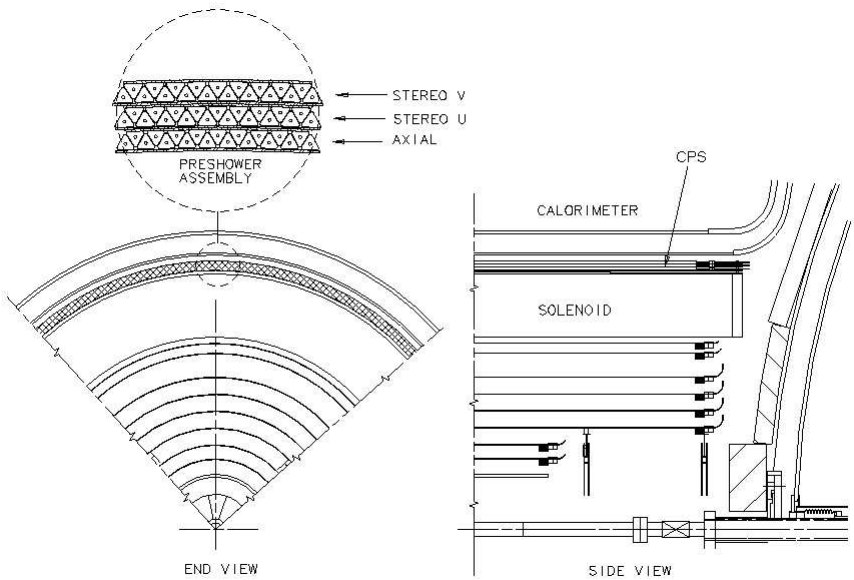

Figure 2.7: Cross-sectional end view (left) and side view (right) of the Central Preshower Detector.

2.2.4 Calorimeters

The DØ calorimeters have been designed to provide excellent measurement of the energy of photons, electrons and hadronic jets, by inducing them to create showers of energy using a large amounts of dense material. The energy in the showers is then sampled at many points, to determine its shape and energy. In this section, I first describe the energy measurement in the calorimeter, then describe the calorimeter and its performance.

Energy Measurement

EM objects interact primarily with materials via the following two processes: pair production ($\gamma \to e^+e^-$) and bremsstrahlung ($e \to e\gamma$). For each successive interaction the number of secondary particles increases while the average energy per particle decreases. It is the collection and measurement of these secondary particles that gives us information on the original EM object's energy. Because of these interactions, the energy of the original particle is expected to drop exponentially:

$$E(x) = E_0 e^{-x/X_0} \tag{2.1}$$

where E_0 is the particle's original energy, x is the distance traveled, and X_0 is the radiation

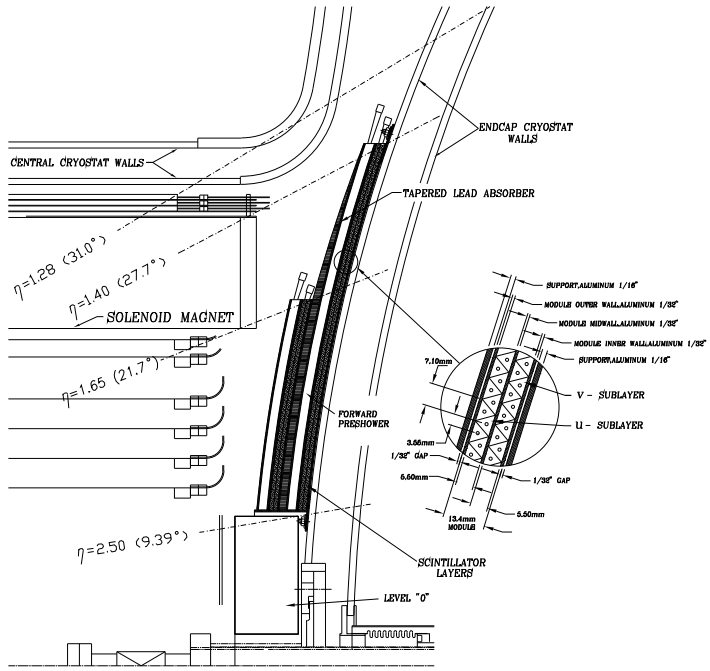

Figure 2.8: One quarter view of the Forward Preshower Detector.

length of the material being passed through. For uranium, X_0 is approximately 3.2 mm. For hadrons the interaction with material occurs with the nuclei via the strong nuclear force. These interactions also produce secondary particles, most of them are neutral pions (π^0) and charged pions ($\pi^{\pm}$). While the π^0s produce electrons and photons which interact electromagnetically, the charged pions interact strongly. This type of particle shower tends to develop over longer distances and is also larger. The analog of the radiation length for hadronic interactions is the nuclear interaction length (λ_0), which is about 10.5 cm for uranium.

DØ Calorimeters

Figure 2.9 shows an overview of the DØ calorimeter system [39]. The DØ calorimeters are compensating sampling calorimeters, using liquid argon as an active medium and depleted uranium as well as copper and steel as absorber material. The choice of this configuration was driven by its ease of segmentation, compensation properties, stability of calibration, and homogeneity of response. The high density of uranium allows a compact detector that contains almost all shower energy while reducing cost. There are three liquid argon calorimeters housed in

three separate cryostats - one central (CC) (with $|\eta| < 1.1$) and two endcaps (EC) (with $1.5 < |\eta| < 4.2$). In the inter-cryostat region ($1.1 < |\eta| < 1.4$), both "massless gaps" and an inter-cryostat detector (ICD) have been added to sample the shower energy that is lost by particles that transverse the module endplates and cryostat walls.

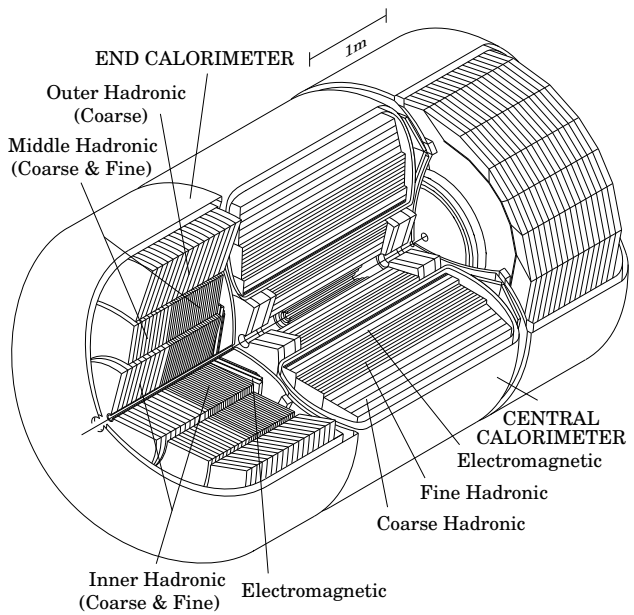

Figure 2.9: Overall view of the calorimeter system.

A typical calorimeter unit cell is shown in Fig. 2.12; it is made up of an alternating sandwich of signal boards and absorber material separated by a 2.3 mm liquid argon gap. The electric field is established by grounding the metal absorber plate and connecting the resistive surfaces of the signal boards to a positive high voltage (2.0 kV). Particles interact with the uranium and the liquid argon, thus producing charged particles in the liquid argon. These charged particles will then move in the electric field and be collected. The electron drift time across the argon gap is ~ 450 ns, which sets the time scale for the signal charge collection. The gap thickness was chosen to be large enough to observe minimum ionizing particle (MIP) signals and to avoid fabrication difficulties.

The pattern and sizes of the readout cells were determined from several considerations. The transverse sizes of the cells were chosen to be comparable to the transverse sizes of showers:

$\Delta R \sim 0.2$ for EM showers and $\Delta R \sim 0.5$ for hadronic showers (where $\Delta R = \sqrt{\Delta\eta^2 + \Delta\phi^2}$). Segmentation finer than this is useful in measuring the shape of electrons and jets. Longitudinal subdivision within the EM, fine hadronic and coarse hadronic sections is also useful since the longitudinal shower profiles help distinguish EM objects and hadron jets.

The final arrangement of the readout cells was chosen to give semi-projective readout towers of equal size in pseudorapidity that are subdivided in depth. The cells are first ganged into layers, and then arranged into semi-projective towers of size 0.1×0.1 in $\Delta\eta \times \Delta\phi$ and are segmented logitudinally into electromagnetic (EM), fine hadronic (FH), and coarse hadronic (CH) sections. A cross sectional view of one quarter of the detector, showing the η and depth segmentation is shown in Fig. 2.10. Each projective tower consists of 8 to 12 layers. To capture the profile of electromagnetic showers, the third layer of the EM section, which corresponds to the shower maximum, is segmented more finely transversely into 0.05×0.05 in $\Delta\eta \times \Delta\phi$ (See Fig. 2.11).

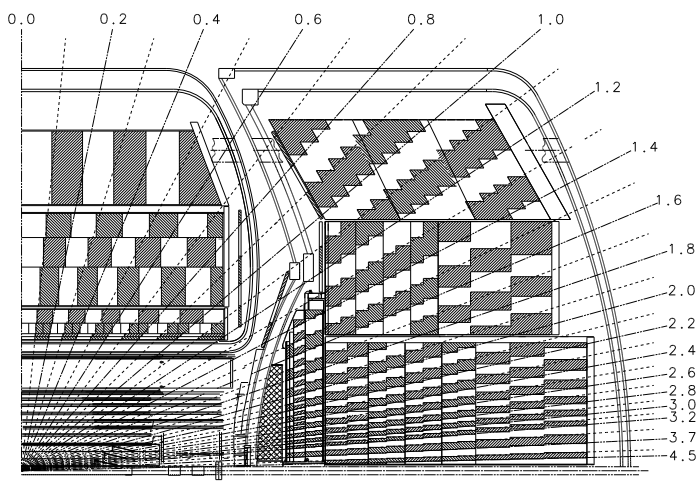

Figure 2.10: Side-view of one quarter of the DØ calorimeter system, showing segmentation and tower definitions. The line extending from the center of the detector denote the pseudorapidity coverage of cells and projected towers.

Different absorber plate materials were used in difference locations. The EM modules for both CC and EC used nearly pure depleted uranium; the thicknesses were 3 mm and 4 mm respectively. The fine hadronic module sections have 6 mm thick uranium-niobium (2%) alloy.

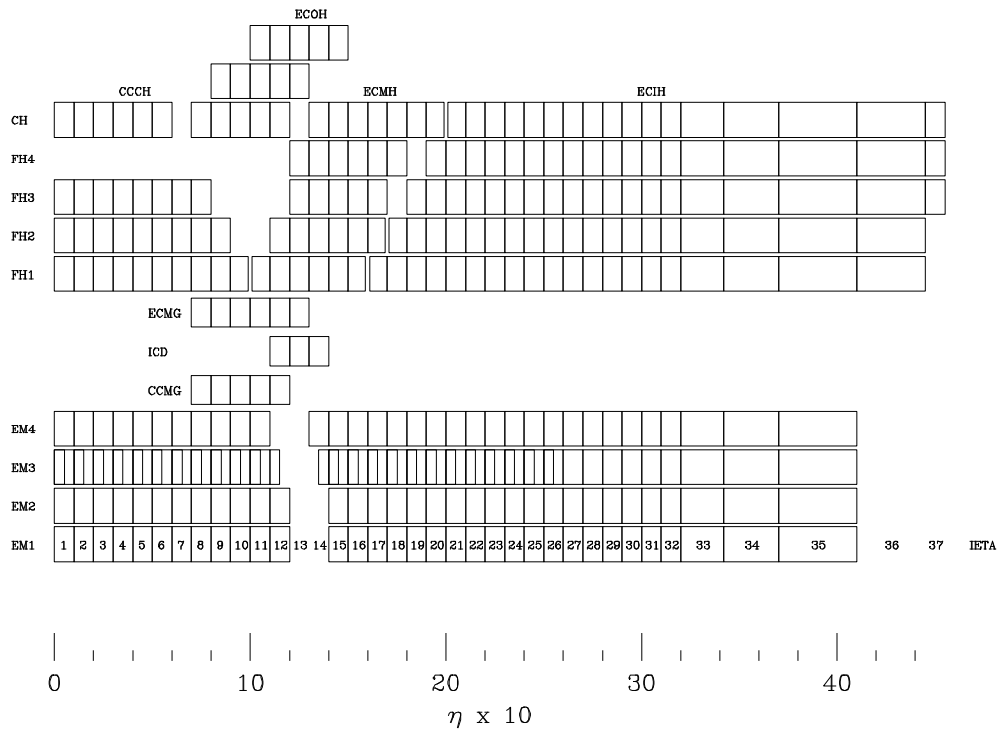

Figure 2.11: Calorimeter channel configuration in terms of depth and η.

The coarse hadronic module sections contain relatively thick (46.5 mm) plates of either copper (CC) or stainless steel (EC). For the CC, the EM section consists of 32 modules, each subtending $2\pi/32 \approx 0.2$ radians in azimuth.

Table 2.1 and 2.2 list the major parameters for the central and endcap calorimeters. At $\eta = 0$, the CC has a total of 7.2 nuclear absorption lengths; at the smallest angle of the EC, the total is 10.3 nuclear absorption lengths.

Calorimeter Electronics

In Run II, the higher instantaneous luminosity of the Tevatron collider with the shorter bunch crossing interval of 132 ns (compared to the Run I bunch crossing interval of 3.5 μs) forces a faster readout time. At the same time, a low-noise performance and minimal channel-to-channel variations must be maintained, to prevent any degradation to the calorimeter's performance [41] [42]. A schematic of the electronics system is shown in Fig. 2.13.

The signal from each calorimeter readout cell is triangular with a very fast rise time and a decay

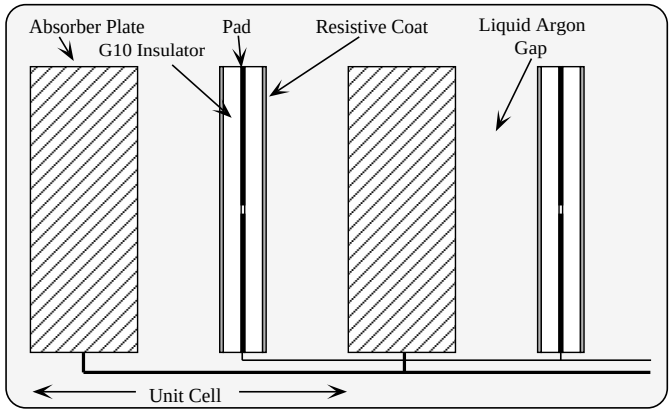

Figure 2.12: Schematic view of a representative calorimeter unit cell. The gap structure, grounded absorber plates, and signal boards are shown.

time of 400 ns. Each signal is taken to a feedthrough port via 30 Ω resistive coaxial cables. The impedance-matched cabling maintains a low-noise transfer of the signal to the preamplifiers. The integrated circuits in the preamplifiers convert the charge to a voltage that is proportional to the input charge. In order to minimize electronic noise stemming from the shorter shaping times, the preamps incorporate a dual field effect transistor (FET) input design. The output signal from the preamplifier is approximately a step function with an about 400 ns rise time and a long fall time ($\sim$ 15 μs). As the values of the calorimeter cell capacitances range over a broad interval, 14 species of preamplifiers were built to match them. The preamplifier output signal is then shaped into a shorter one with a 320 ns rise time and a 500 ns decay time. The shaped signals are sampled every 132 ns; the timing is tuned such that the shaped output can be sampled at its peak at about 320 ns. Because of this earlier sampling time compared to the liquid argon drift time of 430 ns, only $2/3^{rds}$ of the charge in the cell is used to form the preamplifier signal. Figure 2.14 shows the shape of signals from the calorimeter cell, the preamplifier and the shaper.
The signal is then split and sent to two paths. In one path it is amplified by a factor of $8g$ ($g \approx 1$) with respect to the other. The gain factor is defined by precision resistors. We will call the 2 paths $G = 8$ and $G = 1$ respectively. On each path the signal is sampled every 132 ns, and the measured voltage is stored in an analog memory called the Switched Capacitor Array (L1 SCA).

	EM	FH	CH
Number of Modules	32	16	16
Absorber	Uranium	Uranium	Copper
Absorber Thickness (mm)	3	6	46.5
Argon Gap (mm)	2.3	2.3	2.3
Number of Readout Layers	4	3	1
Cells per Readout Layer	$2, 2, 7, 10$	$20, 16, 14$	9
Total Radiation Length (X_0)	20.5	96.0	32.9
Total Interaction Length (λ)	0.76	3.2	3.2

Table 2.1: Central Calorimeter Module Parameters.

On a trigger, a gain selector decides which of the 2 signals ($G = 1$ or $G = 8$) is most appropriate: the $G = 8$ one if the signal is below a certain saturation voltage, the $G = 1$ otherwise. The reason two paths are used is that the Analog-to-Digital Converters (ADCs) only have a 12-bit dynamic range, while a 15-bit range is needed. The SCA is a 48-element-deep storage device that provides a buffer zone for saving analog information from a calorimeter channel until it can be processed through the ADC's after an event has occurred and a trigger has been received. The sample at the nominal peak time and the one earlier by 3×132 ns are then retrieved from the SCA memory and the earlier sample is subtracted from the nominal one in the baseline subtractor (BLS). The difference voltage is stored into another analog memory (L2 SCA). On a positive trigger decision, the voltage is retrieved from the memory and digitized in an ADC. The integer number is finally multiplied by 8 if the signal previously proceeded through the $G = 1$ path. The ADC counts are ultimately transferred to a host computer for storage and analysis.

The readout electronics of the DØ calorimeter is composed of 12 crates containing 12 ADC cards. Each card contains 384 channels which are distributed on 8 BLS cards, each treating the signals of 4 towers with 12 longitudinal depths each. All three calorimeter cryostats together contain a

	EM	IFH	ICH	MFH	MCH	OH
Number of Modules	1	1	1	16	16	16
Absorber	Uranium	UNb	SS	UNb	SS	SS
Absorber Thichness (mm)	4	6	46.5	6	46.5	46.5
Argon Gap (mm)	0.23	0.21	0.21	0.22	0.22	0.22
Number of Readout Layers	4	4	1	4	1	3
Cells per Readout Layer	$2, 2, 6, 8$	16	14	15	12	8
Total Radiation Length (X_0)	20.5	121.8	32.8	115.5	37.9	65.1
Total Interaction Length (λ)	0.95	4.9	3.6	4.0	4.1	7.0

Table 2.2: End Calorimeter Module Parameters. IFH, ICH, MFH, MCH, OH stand for inner fine hadronic, inner coarse hadronic, middle fine hadronic, middle coarse hadronic and outer hadronic section respectively. UNb and SS stand for Uranium-Niobium alloy and Stainless Steel.

total of $12 \times 12 \times (8 \times 4 \times 12) = 12 \times 12 \times 384 = 55296$ channels. Figure 2.15 shows the channel hierarchy.

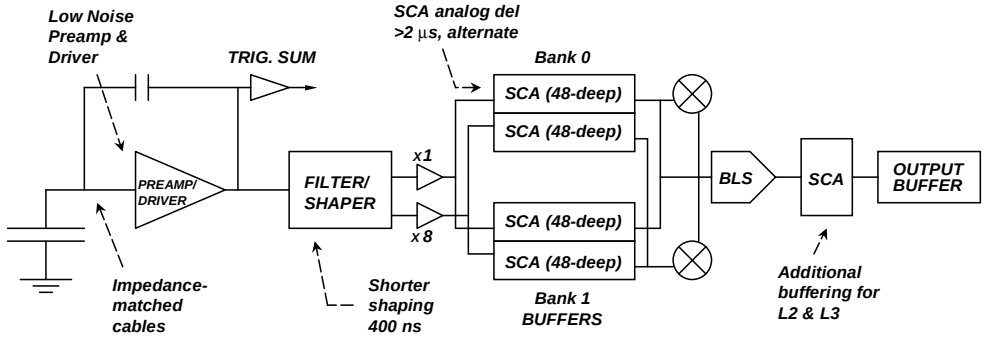

Figure 2.13: Schematic of the primary elements for the DØ calorimeter electronics.

Calorimeter Performance

The performance of the calorimeter is very crucial for the W width measurement. The energy resolution can be described as arising from three major sources. The first is the noise term that

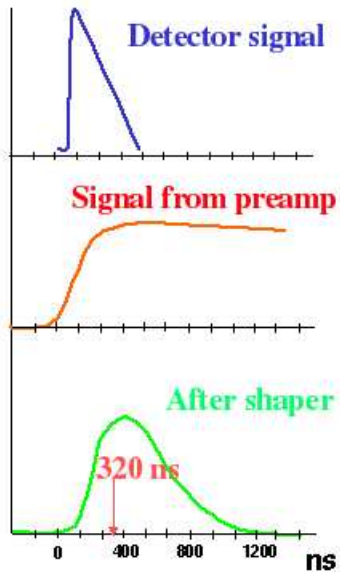

Figure 2.14: Electronics signal shape from the calorimeter cell, after the preamplifier and after the shaper.

has a fixed value, independent of the observed signal. The second is the sampling term which reflects statistical fluctuations in the energy deposited in the argon and therefore scales like the square root of the signal size. The third is the constant term, which reflects how well the response of different parts of the detector are equalized, in other words, how well we understand and calibrate the entire calorimeter. It therefore scales linearly with signal size, assuming the energy is distributed over approximately the same number of readout cells, independent of energy. The energy resolution is thus described using the following functional form:

$$\frac{\sigma_E}{E} = \sqrt{\left(\frac{N}{E}\right)^2 + \left(\frac{S}{\sqrt{E}}\right)^2 + C^2} \tag{2.2}$$

where N, S and C are the noise, sampling, and constant terms, respectively. In Run I, the three terms were determined to be: $N = 0.003$ GeV, $S_{EM} = 0.15$ GeV$^{1/2}$ [43] [44] and $C = 1.15^{+0.27}_{-0.36}\%$ [16]. The values for Run II will be discussed in Sec. 6.3.

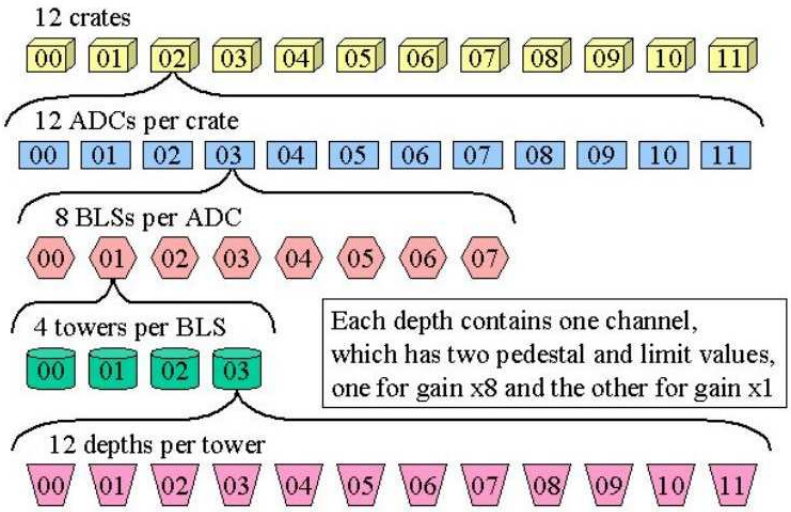

Figure 2.15: Channel hierarchy for the DØ calorimeter electronics.

2.2.5 Muon System

Surrounding the calorimeter is the muon system [45]. Muons are about 200 times heavier than electrons, and therefore they lose very little energy via bremsstrahlung, unlike electrons. Muon energy loss occurs due to ionization in the detector media, which is a low energy loss absorption process. Therefore, muons above a certain energy threshold (about 3 GeV) pass through the whole DØ detector. Also, since muons are measured after the electromagnetic and hadronic particle showers are absorbed in the calorimeters, muons can be identified in the middle of hadron jets with much greater purity than electrons.

To detect muons, a second tracking system is located outside the calorimeter. This has three layers of detectors giving position measurements, and a toroid magnet with a 1.8 T field located between the first and second layer, allowing a measurement of momentum. Position measurements are provided by drift chambers. These chambers collect charge ionized in a gas by the passage of a charged particle. The gas is held in a sealed volume. The chambers are arranged in planes, four planes make up the central muon system, surrounding the calorimeter and providing coverage up to $|\eta| < 1$. Two further planes of detectors are located at either end of the calorimeter, making up the forward muon system. These extend the detector coverage out to

$|\eta| < 2.2$. The drift chambers provide an accurate (to within 0.5 mm) measurement of the coordinate perpendicular to the sense wires (corresponding to η). The muon detectors also have layers of scintillating material arranged in pixels; these provide the best measurement of the other coordinate (corresponding to ϕ). Signals from the drift chambers and scintillators in each region are combined into segments. Segments are then joined in a fit, with a measurement of the bending in the toroidal magnetic field giving a measurement of muon momentum.

2.3 Trigger System

Overview of the Trigger System

The proton-antiproton beams make about 1.7 million collisions per second at the center of the DØ detector. The information collected for each collision is called an event. Not every event needs to be saved to the tape. Actually, roughly only a few collisions in a million are of physics interest. The task of the trigger system is to reduce this rate by evaluating events and deciding whether they are interesting or if they can be discarded.

The DØ trigger system is implemented as a hierarchy of three distinct selection stages: the level 1 trigger (L1) is designed to have an ouput rate of 10 kHz, the level 2 trigger (L2) has an output rate of 1 kHz, and the level 3 trigger (L3) has an output rate of 50 Hz (shown in Fig. 2.16).

The level 1 decision is made based on the fast readout of the sub-detectors and simple algorithms in Field Programmable Gate Arrays (FPGA) [46]. The L2 trigger [47] receives the information from L1 output and creates physics object candidates such as tracks. electrons, jets and muons. The information pathway for the L1 and L2 triggers is shown by the block diagram in Fig. 2.17.

The Level 3 trigger [48] is based on a computer farm including over 100 dual 1 GHz Pentium III PCs. It receives information from all sub-detectors and L1, L2 crates, and then partially reconstructs the event to determine whether it passes the software filtering. The software filtering is accomplished by a series of filter tools. Each tool has a specific function related to the identification of a type of particle or characteristic. The filter tools are associated in particular combinations and ordered into 128 L3 scripts. If any of the L3 scripts is passed, the event will be

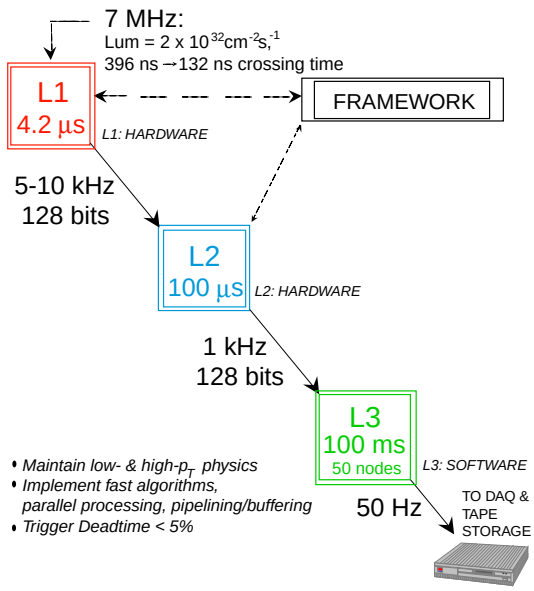

Figure 2.16: Summary of the three-level DØ trigger system for Run II with the decision time and bandwidth allocated to each level.

recorded on permanent storage media.

Calorimeter Triggers

Since in this analysis, all W and Z candidates are required to pass the calorimeter triggers, I will discuss the calorimeter L1/L2/L3 EM triggers in more detail.

At L1, four calorimeter towers are combined into a trigger tower of size 0.2×0.2 in $\Delta\eta \times \Delta\phi$. The energy is readout for two depth sections: the electromagnetic layers are combined, as are the fine hadronic layers. The calorimeter L1 trigger terms are of the form CEM(x, y) and CJT(x, y) where x is the number of towers above a transverse energy threshold of y GeV. CEM is the readout of the energy deposited in the electromagnetic section, CJT is the total transverse energy of the electromagnetic and fine hadronic layers combined in the tower.

The L2 calorimeter trigger consists of three processors which are designed for electron/photon, jet finding and $\not\!\!E_T$ calculation, respectively. Each processor uses information from the L1 trigger and combines appropriate sub-detector proto-objects into physics objects. For a more detailed description of the L2 calorimeter trigger, the reader is referred to [49].

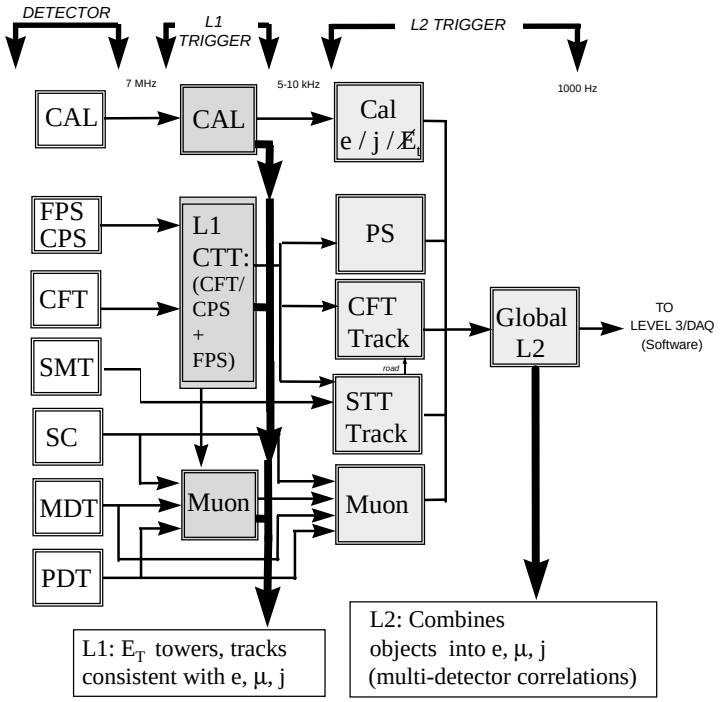

Figure 2.17: L1 and L2 trigger data pathway. The arrow indicates the direction of data flow.

At L3 a fast version of the offline code for electron identification is used. The trigger decision is based on a combination of an energy threshold, a cut on the energy fraction in the electromagnetic calorimeter, and requirements on shape of the cluster. The trigger strategy is to lower the requirements on the electron candidate as their energy increases.

Chapter 3

Event Selection

3.1 Data Set

Since the start of Run II in 2001, the DØ detector has collected about 400 pb^{-1} data; Fig. 3.1 shows the integrated luminosity delivered by the Tevatron collider and recorded by the DØ detector since 2001 [50].

The sample used for this particular analysis was collected from August 2002 to September 2003. Runs declared bad due to hardware failures or when electronics noise is unusually large [51] are removed from this sample, leaving a total of 177.3 pb^{-1} of integrated luminosity. The quality assessment of the bad runs is based on distributions of the reconstructed $\not\!\!E_T$. The three criteria used in the run selection are [52]:

- the average scalar E_T [1] of the run is > 80 GeV (in the range 100-120 GeV is normal);
- the mean shift of the $\not\!\!E_T$ ($\sqrt{\not\!\!E_{Tx}^2 + \not\!\!E_{Ty}^2}$) is lower than 4 GeV (a clean run has a mean shift below 0.5 GeV);
- the RMS of the $\not\!\!E_T$ distribution ($\sqrt{\sigma^2(\not\!\!E_{Tx}) + \sigma^2(\not\!\!E_{Ty})}$) (discussed in Sec. 3.5) has to be below 16 GeV (10 GeV is typical).

The information recorded online by the detector is in the form of digital signals, which need to be interpreted as physics objects. This complicated task is performed by the standard reconstruction software package, D0RECO [53]. D0RECO starts by processing the raw data into high-level objects, such as energy clusters in the calorimeters or tracks in the tracking and muon systems. These objects are in turn combined to form the physical particles: electrons, photons,

[1] Scalar E_T is defined as the total transverse energy deposited in the calorimeter $SE_T = \sum E_T^i$, where i runs over all cells except the cells in the coarse hadronic calorimeter.

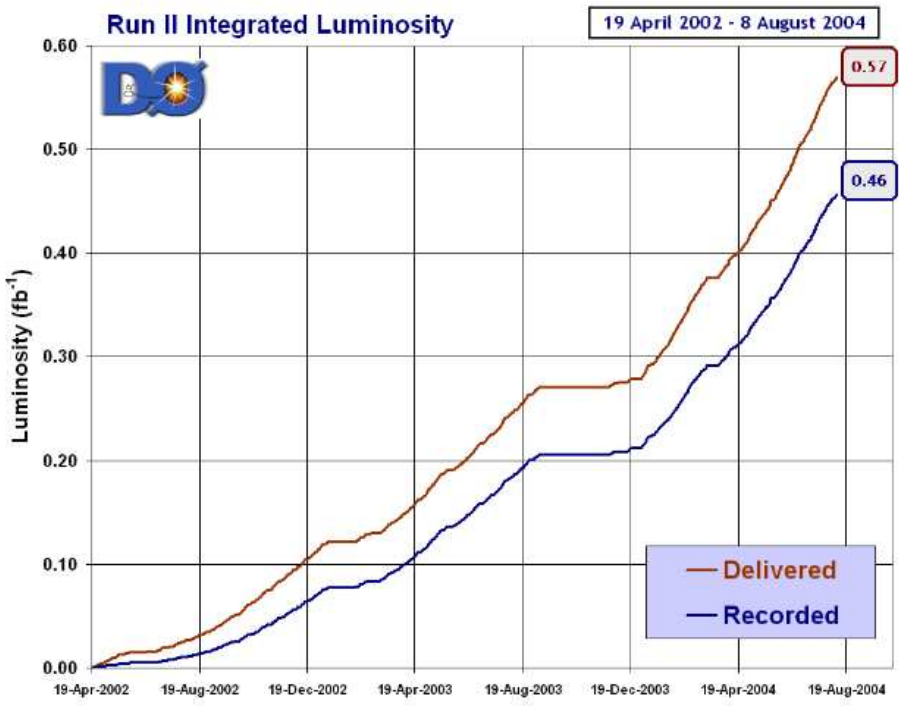

Figure 3.1: Integrated luminosity delivered by the Tevatron Collider and recorded by the DØ detector.

jets, muons and neutrinos. Since for this analysis, we are interested in vertices, electrons and neutrinos, I will only discuss vertex, electron and neutrino identification in detail.

3.2 Trigger Selection

Events which enter into the final Z and W candidate samples are selected from a combination of single EM triggers. For an event to be used, a candidate electron must fire one of these triggers. Listed below, is the preferred order of trigger combinations to use based on which are

Trigger	L1	L2	L3
EM_HI_SH	CEM(1, 10)	EM(1, 12)	ELE_LOOSE_SH_T(1, 20)
EM_HI_2EM5_SH	CEM(2, 5)	EM(1, 12)	ELE_LOOSE_SH_T(1, 20)
EM_HI	CEM(1, 10)	EM(1, 12)	ELE_LOOSE(1, 30)
EM_MX_SH	CEM(1, 15)	-	ELE_LOOSE_SH_T(1, 20)
EM_MX	CEM(1, 15)	-	ELE_LOOSE(1, 30)
E1_SHT20	CEM(1, 11)	-	ELE_NLV_SHT(1, 20)
E2_SHT20	CEM(2, 6)	-	ELE_NLV_SHT(1, 20)
E3_SHT20	CEM(1, 9)CEM(2, 3)	-	ELE_NLV_SHT(1, 20)
E1_SH30	CEM(1, 11)	-	ELE_NLV_SH(1, 30)

Table 3.1: Single EM triggers used in this analysis.

unprescaled [2] [55]. For global CMT 8 to 11 trigger combinations (runs $\leq$ 178721) [3]: EM_HI_SH or EM_HI_2EM5_SH, EM_HI_SH, EM_HI, EM_MX_SH, EM_MX. For global CMT 12 trigger combinations (runs $\geq$ 178722): E1_SHT20, E2_SHT20, E3_SHT20 or E1_SH30, E1_SHT20, E2_SHT20 or E1_SH30, E1_SHT20 or E1_SH30, E1_SHT20. See Table 3.1 for a summary of EM triggers used in this analysis, the exact meaning of each trigger term is explained in Table 3.2.

[2] if a set of trigger conditions does not reject a high enough fraction of events and would lead to an unacceptable rate of events being written to tape, it gets "prescaled". This means only a fraction of passing events are accepted, and this fraction is determined by the prescale factor. In general, the prescale factors are adjusted according to the instantaneous luminosity to keep as many interesting events as possible while keeping the total rate to tape approximately constant.

[3] In order to cope with the increasing Tevatron instantaneous luminosity, we have used several versions of global combined trigger list during the data taking period, the L1/L2/L3 requirements are the same for the CMT 8 to 11 trigger combinations, while for CMT 12, the L1/L2/L3 conditions have changed.

L1 Triggers

CEM(1, 10)	one EM trigger tower with $E_T > 10$ GeV
CEM(2, 5)	two EM trigger towers with $E_T > 5$ GeV
CEM(1, 15)	one EM trigger tower with $E_T > 15$ GeV
CEM(1, 11)	one EM trigger tower with $E_T > 11$ GeV
CEM(2, 6)	two EM trigger towers with $E_T > 6$ GeV
CEM(1, 9)CEM(2, 3)	one EM trigger tower with $E_T > 9$ GeV, another EM trigger tower with $E_T > 3$ GeV

L2 triggers

EM(1, 12)	one EM candidate with $E_T > 12$ GeV (not present for runs below 169524)

L3 triggers

ELE_LOOSE_SH_T(1, 20)	one electron with $\|\eta\| < 3.0$ and $E_T > 20$ GeV passing loose requirements including shower shape cuts
ELE_LOOSE(1, 30)	one electron with $\|\eta\| < 3.0$ and $E_T > 30$ GeV passing loose requirements
ELE_NLV_SHT(1, 20)	one electron with $\|\eta\| < 3.6$ and $E_T > 20$ GeV passing tight shower shape cuts
ELE_NLV_SH(1, 30)	one electron with $\|\eta\| < 3.6$ and $E_T > 30$ GeV passing loose shower shape cuts

Table 3.2: L1/L2/L3 requirements for each of the Single EM triggers used in this analysis.

3.3 Track and Vertex Reconstruction

Hits from the SMT and CFT are used to reconstruct the trajectories of charged particles and the event vertex. The track finding algorithm is road-following with a Kalman filter update implemented using the TRF++ software package [56]. Tracking is first done for each individual layer to produce track segments; the track segments are matched between layers to form global track candidates; a fit of a track and nearby hits is then performed and the track is accepted (rejected) if the fit is good (poor) as determined by the $\chi 2$ value [57].

The interaction point of an event is called the event vertex. There are two types of vertices: primary and secondary vertices. A primary vertex is the original interaction point with the largest number of associated tracks, while a secondary vertex is a displaced vertex due to long-lived meson decay (e.g. B, K_s or D). The x and y coordinates of the primary vertex are close to zero since the cross sectional extent of the beam is ≈ 40 μm [58]. However, the z coordinate has a range with a rms width of 28 cm and with a central value close to zero [55]. The reconstruction and selection of primary and secondary vertices is described in detail in [59].

The primary vertex candidates are found by first selecting global tracks with at least one hit in the SMT and then fitting a vertex position from these tracks (bad tracks with a large contribution to the $\chi 2$ are removed), repeating this procedure until convergence. A primary vertex must contain at least 3 tracks.

The secondary vertex candidates are found by forming a good seed from two tracks that do not point to the primary vertex and fitting a secondary vertex, then adding another track and refitting the secondary vertex (if the $\chi 2$ becomes larger, the track is removed), repeating the procedure until there is no more good tracks. There can be more than one secondary vertex.

3.4 Electron Identification

A cluster-finding algorithm is used to find showers in the EM calorimeter. The algorithm begins with a list of EM towers with significant energy (an EM tower is defined by adding the energy measured by the calorimeter in all four EM layers plus the first FH layer for cells within 0.1×0.1

in $\Delta\eta \times \Delta\phi$). The seed is the tower with the highest p_T. The algorithm starts with the seed tower, then looks at all neighbors of that tower and includes the highest energy neighbor in the cluster. The process continues until there are no more towers with a neighbor above the threshold ($\sim$ 50 MeV). The cluster has to pass crude initial selection criteria imposed by the DØ reconstruction program. Unless the p_T of the cluster is above 1.5 GeV, the cluster is rejected. Electromagnetic candidates are required to have EM fraction f_{EM} above 0.9 and the isolation variable (f_{iso}) less than 0.2. The EM fraction is defined as the ratio of the EM energy to the total energy in the cluster. The isolation is defined as

$$f_{iso} = \frac{E_{cone} - E_{core}}{E_{core}} \tag{3.1}$$

where E_{cone} is the energy in a cone of radius $R = \sqrt{\Delta\eta^2 + \Delta\phi^2} = 0.4$ around the direction of the cluster, summed over the entire depth of the calorimeter except the CH layers and E_{core} is the energy in a cone of $R = 0.2$, summed over the EM layers only.

Since charged hadrons deposit less than 10% of their energy in the EM calorimeter, and electrons from W and Z boson decays tend to be isolated from other particles, f_{EM} and f_{iso} provide powerful discrimination between the EM objects and hadron jets.

A cluster that passes the default thresholds enters the final stage of the reconstruction. At this stage, various quantities that describe cluster properties are computed and stored. A few examples are cluster energy, cluster p_T, η and ϕ. In addition, a multi-variate tool is used to determine how well the shape of the EM cluster agrees with that expected for an electromagnetic shower. It is the inverse of the covariance matrix built on the following seven variables: the fractional energies in the four EM layers, shower width in the η direction, the logarithm of the cluster energy and the position of the primary vertex. The 7-dimensional covariance matrix is determined from the GEANT based Monte Carlo simulation [54].

The electron energy is computed from the signals in all EM towers within a window of 0.5×0.5 in $\Delta\eta \times \Delta\phi$ (5×5 towers) (for CC) or within a cone of 10 cm radius in EM3 (for EC) centered on the tower which registered the highest fraction of the electron energy. The calorimeter shower centroid position is determined using a log-energy-weighted algorithm (discussed in Sec. 6.5). If

an electron has a matched track, the direction of this electron is then given by the direction of the matched track. If the electron does not have a matched track, then the calorimeter shower centroid position and the primary vertex position are used to define the electron direction. The momentum of the electron is thus given by:

$$\vec{p}(e) = E(e) \begin{pmatrix} \sin\theta(e)\cos\phi(e) \\ \sin\theta(e)\sin\phi(e) \\ \cos\theta(e) \end{pmatrix} \tag{3.2}$$

and the transverse momentum of the electron is $E_T(e) = E(e)\sin\theta(e)$.

Electron candidates satisfy the following requirements:

- $|\eta^{det}| < 1.05$; [4]
- In calorimeter fiducial region;
- EM fraction > 0.9;
- Isolation < 0.15;
- HMatrix7 < 12;
- $E_T > 25$ GeV;
- Calorimeter Quality cuts;
- Not inside CC-EM module 17. [5]

The fiducial requirement requires the EM object be in a well-understood region of the calorimeter; electrons near to the intermodule boundaries were excluded. There are 32 equal

[4] There are two η's used in this analysis: detector η (or η^{det}) and physical η (η^{phys} or simply η). η^{det} is derived from the angle between the center of the detector and the cluster position in the EM calorimeter; η^{phys} is derived from the physical polar angle between the interaction vertex and the cluster position. η^{phys} is thus related to the true angle made by the particle with respect to the detector whereas η^{det} is related to the true position of the particle in the detector.

[5] The electron energy response for this module ((int)$(32 \times \phi^{e}_{det}/2\pi) = 16$) is about 8% lower than the rest 31 modules, and this module was damaged during assembly at the beginning of Run I.

modules in the CC region, and the modules are located at $\phi = 2\pi N/32$, where $N = 0, 1, \cdots, 31$. The excluded regions were mod(ϕ, $2\pi/32$)<0.1 and mod(ϕ, $2\pi/32$)>0.9. Electrons near the ends of the central calorimeter were also excluded. The electron energy is reconstructed using a 0.5×0.5 window in $\eta \times \phi$ space, while the central calorimeter extends $|\eta^{det}| = 1.2$. To ensure that the electron window is not clipped, the calorimeter cluster is required to satisfy $|\eta^{det}| < 1.05$. Calorimeter quality cuts refer to the calorimeter areas that have an identified hardware problem as discussed in [55].

An important source of background for electrons is photons from π^0 or η meson decays. This background was reduced by requiring that a track from a charged particle in the tracking detector be consistent with the position of the cluster in the calorimeter. In the final sample, electrons are required to be matched to a track reconstructed in the central tracker using the following χ^2 variable:

$$\chi^2 = \left(\frac{\Delta\phi}{\sigma_\phi}\right)^2 + \left(\frac{\Delta z}{\sigma_z}\right)^2 + \left(\frac{E/p - 1}{\sigma_{E/p}}\right)^2 \tag{3.3}$$

where $\Delta\phi$, Δz are the angle difference and the spatial difference between the electron position and the extrapolated track position, E is the energy of the EM cluster measured by the calorimeter and p is the momentum measured by the tracker system. σ_ϕ, σ_z and $\sigma_{E/p}$ are the associated experimental resolutions. Tracks with a track match significance $\chi 2$ probability > 0.01 are considered good matches [6].

3.5 Neutrino Identification

Neutrinos (and other weakly interacting neutral particles) are not directly detected by the DØ detector. As explained in Sec. 2.2.1, the conservation of energy in proton antiproton collisions cannot be used as a constraint in the beam direction, as particles escape detection along the beam. The presence of these undetected particles is inferred from an overall momentum imbalance in the event. Since the total momentum is conserved in the transverse plane, a large

[6] To give an idea of the level of track matching required, for the CC this is roughly $\Delta Z < 2.4$ cm, $\Delta\phi < 0.02$ rad or $|E/p - 1| < 0.6$ when the other terms are zero.

missing E_T, denoted as $\not{E}_T$, indicates the production of high-p_T neutrino(s).

The missing transverse momentum is calculated by taking the vector sum

$$\vec{\not{E}}_T^{\,raw} = -\sum_i E_i \sin\theta_i \begin{pmatrix} \cos\phi_i \\ \sin\phi_i \end{pmatrix} = -\sum_i \vec{E}_T^i \tag{3.4}$$

where the sum runs over all calorimeter cells that were read out except cells in the coarse hadronic calorimeter. E_i are the cell energies, and ϕ_i and θ_i are the azimuth and coaltitude of center of cell i with respect to the primary vertex.

After we have the raw missing transverse energy, we then apply electron energy corrections on EM clusters with $E_T > 5$ GeV, EM fraction>0.9, Isolation<0.15 to get the corrected missing transverse energy $\not{E}_T$. In this analysis, we use this corrected missing transverse energy; no jet corrections are applied. In principle, one could improve the missing energy resolution by applying jet corrections. However, in the present analysis this is not done because the recoil distributions of W and Z events are soft, typically a few GeV. Since the jet corrections are not well measured for low p_T jets, it is not clear that they would improve the recoil measurement. In addition, at DØ, jets are not reconstructed below 8 GeV, so the analysis would suffer from threshold effects.

3.6 Offline Selection Criteria

The offline criteria for the Z and W sample were chosen to select well-measured events with low background contamination.

3.6.1 $Z \to ee$ Selection Criteria

The kinematic and fiducial requirements that define the Z boson candidate sample are

- At least 2 electron candidates;
- Each electron candidate has a matched track;
- One of the electron candidates must have fired one of the single EM triggers.

The two electron candidates with the highest p_T are selected to form a Z if there are more than 2 electron candidates. This resulted in a sample of 3169 candidate events with two electrons in CC region, and an invariant mass between 0 and 150 GeV. Figure 3.2 shows the invariant mass distribution of the CCCC Z boson candidate events [7].

In the case of $Z \to ee$ events, we often use the following variables:

- Dielectron transverse momentum (or the transverse momentum of the Z Boson)

$$\vec{p}_T^{\,ee} = \vec{p}_T^{\,Z} = \vec{p}_T^{\,e1} + \vec{p}_T^{\,e2} \tag{3.5}$$

- Transverse momentum of the recoil system (all particles recoiling against the Z boson)

$$\vec{u}_T = -\vec{p}_T^{\,e1} - \vec{p}_T^{\,e2} - \vec{\not{E}}_T = -\vec{p}_T^{\,ee} - \vec{\not{E}}_T \tag{3.6}$$

- Invariant mass

$$M_{ee} = \sqrt{2E(e1)E(e2)(1-\cos\omega)} \tag{3.7}$$

where ω is the opening angle between the two electrons [8].

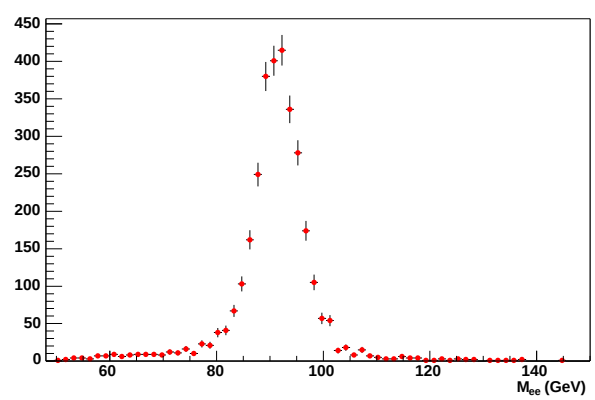

Figure 3.2: Invariant mass distribution of $Z \to ee$ candidates.

[7] If two electrons from Z decays are both located in CC or EC region, we call it a CCCC or ECEC Z candidate; if one electron is located in CC region and the other one located in EC region, we call it a CCEC Z candidate.

[8] The open angle ω between two electrons is $\cos\omega = \sin\theta_1 \sin\theta_2 \cos(\phi_1 - \phi_2) + \cos\theta_1 \cos\theta_2$, where θ_1, θ_2, ϕ_1 and ϕ_2 are the polar angles and azimuthal angles of the two electrons.

3.6.2 $W \to e\nu$ Selection Criteria

The kinematic and fiducial requirements that define the W boson candidate sample are

- At least 1 electron candidate with a matched track;
- This electron candidate must have fired one of the single EM triggers;
- $\not\!\!E_T$>25 GeV;
- $p_T^W < 20$ GeV;
- no second track with $p_T > 15$ GeV that is back-to-back with the electron (to remove $Z \to ee$ background).

The p_T^W cut was chosen to minimize systematic errors in the detector modeling. Since the Z sample has only a few events at high p_T^Z, the detector model is best constrained at low p_T^W. The second purpose is to reduce QCD background.

This resulted in a sample of 75910 candidate events with the electron in the CC region and transverse mass between 0 to 200 GeV, and 625 candidate events with transverse mass between 100 to 200 GeV. Figure 3.3 shows the transverse mass distribution of the central W boson candidate events used in this measurement.

In the case of $W \to e\nu$ events, we often use the following variables:

- Transverse momentum of the W boson

$$\vec{p}_T^{\,W} = \vec{p}_T^{\,e} + \vec{\not\!\!E}_T \tag{3.8}$$

- Transverse momentum of the recoil system (all particles recoiling against the W boson)

$$\vec{u}_T = -\vec{p}_T^{\,W} = -\vec{p}_T^{\,e} - \vec{\not\!\!E}_T \tag{3.9}$$

- Transverse mass

$$M_T = \sqrt{2E_T(e)\not\!\!E_T(1 - \cos[\phi(e) - \phi(\not\!\!E_T)])}. \tag{3.10}$$

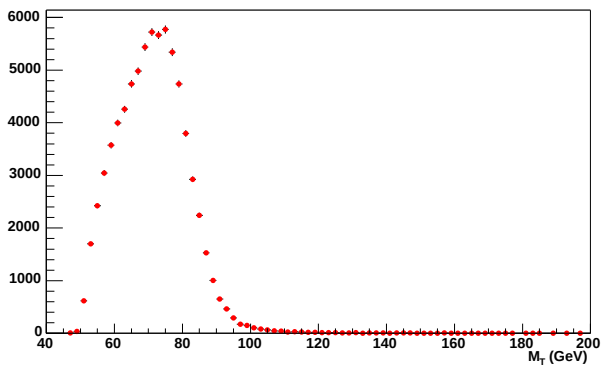

Figure 3.3: Transverse mass distribution of $W \to e\nu$ candidates.

Chapter 4

Efficiencies, Fake Rate and Backgrounds

There are two main inefficiencies which affected this measurement: those related to the hardware trigger, and those related to electron identification criteria. Both effects can potentially bias the measurement as these particular inefficiencies depend on the kinematics. These efficiencies are determined from data as discussed below.

4.1 Efficiencies

The efficiencies described here are mainly trigger efficiency, preselection efficiency, HMatrix7 efficiency and track matching efficiency. The detailed analysis can be found elsewhere [55] [60], here only the main points are listed.

We often apply a "tag - probe" method on $Z \to ee$ data to determine the selection efficiencies. The idea of the "tag - probe" method is to require one leg of $Z \to ee$ pass very tight cuts (tag electron), while the other leg only needs pass very loose cuts (probe electron). The loose electrons will then be an unbiased sample for us to study the efficiencies for various cuts. The definition of "tag electron" is a good EM candidate that passes trigger requirements and has a matched track. Subtraction of QCD background from the $Z \to ee$ event sample is needed for various efficiency measurements and to extract the number of Z events. The invariant mass distribution of the QCD background is determined directly from data, and QCD background candidates are required to have at least two EM candidates that pass all criteria described in Sec. 3.4 except the HMatrix7 cut (instead we invert HMatrix7 cut: HMatrix7 > 20). The normalization is obtained from a fit to the data of the background and $Z/\gamma^* \to ee$ signal Monte Carlo shapes.

4.1.1 Trigger Efficiency

As mentioned before, the trigger efficiency is measured using the "tag - probe" method. To pass a trigger's requirements, an electron must have a matching trigger object at each level which passes all cuts for the corresponding trigger. The electron candidate to trigger object matching requirements are: $\Delta R = \sqrt{\Delta\eta^2 + \Delta\phi^2} < 0.4$ for L1, L2 and L3. The average trigger efficiency is found to be 98.2% for runs $\leq$ 178721 and 97.4% for runs $\geq$ 178722 respectively. Trigger efficiency is highly dependent on electron p_T; Fig. 4.1 shows the trigger efficiency for both run ranges as a function of electron p_T in the CC region.

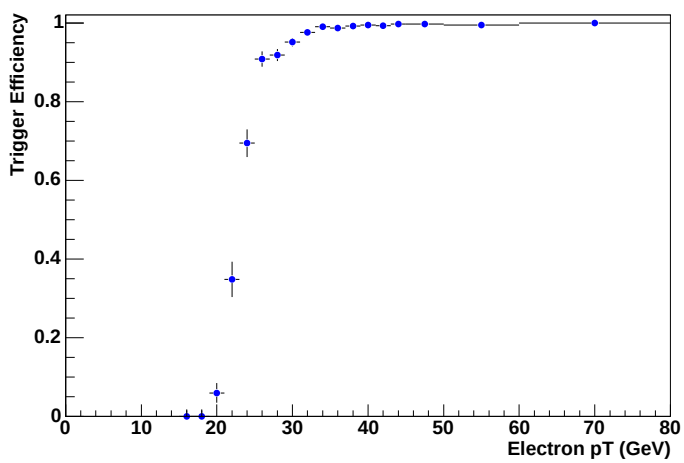

Figure 4.1: Trigger efficiency vs electron p_T.

4.1.2 Preselection Efficiency

The preselection efficiency is defined as the efficiency for an electron to form an EM cluster passing the EM fraction (> 0.9) and the isolation requirements (< 0.15). An unbiased sample not using calorimeter information needs to be employed to study this efficiency. The sample we use is EM + track data: the tag leg consists of a good electron candidate and the probe leg of a track. The average preselection efficiency is determined to be $(98.8 \pm 0.3)\%$. The efficiency versus electron pseudorapidity is shown in Fig. 4.2.

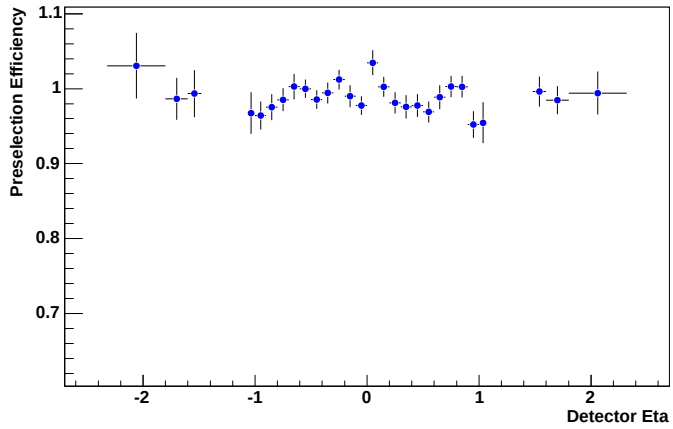

Figure 4.2: Preselection efficiency vs electron detector eta.

4.1.3 HMatrix7 Efficiency

HMatrix7 is the cut to require that the shape of the EM cluster be consistent with that of an electron. The efficiency is also determined using the "tag - probe" method, where the probe EM cluster passes all EMID selection criteria except the HMatrix7 requirement. The average efficiency is determined to be $(92.80 \pm 0.28)\%$ for CC and $(95.60 \pm 0.44)\%$ for EC. The HMatrix7 efficiency versus electron pseudorapidity is shown in Fig. 4.3.

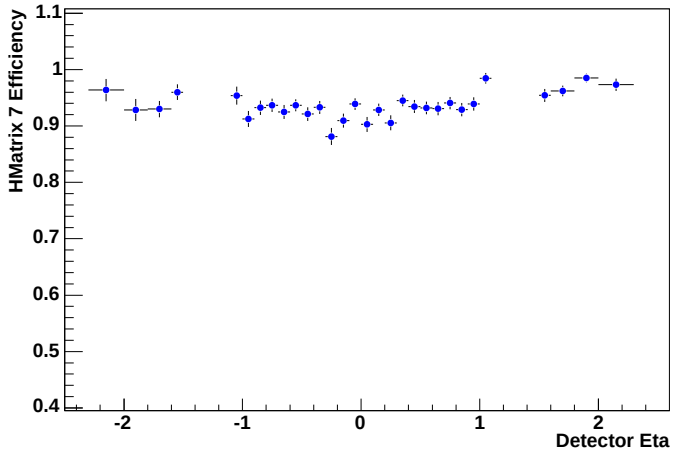

Figure 4.3: HMatrix7 efficiency vs electron detector eta.

4.1.4 Track Matching Efficiency

As mentioned in Sec. 3.4, we apply the track matching criteria on the electron candidate in order to remove a large contamination of QCD events. However, a QCD jet can sometimes have a matching track. Both the efficiency for an electron to have a matched track and the probability of a QCD produced EM object to have a matched track must be measured. The "tag - probe" method is applied to get the track matching efficiency versus pseudorapidity. The tag cluster is required to have a good track match and the second EM cluster is checked for a good track match. The average efficiency is $(79.0 \pm 0.5)\%$ for CC and $(74.3 \pm 0.9)\%$ for EC. The track matching efficiency versus electron pseudorapidity is shown in Fig. 4.4 [1].

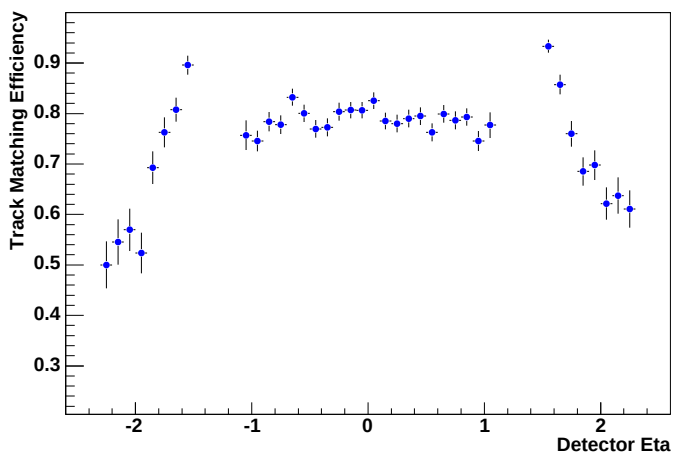

Figure 4.4: Track Matching efficiency vs electron detector eta.

4.2 Fake Rate

The fake rate (also called fake track matching probability) is determined from Jet-Jet (called di-jet) events where one jet has been misidentified as an electron. The EM cluster has to pass the EMID requirement and be back-to-back with a jet in ϕ with a deviation of $\Delta\phi < 0.5$. Jet

[1] In the EC region, we do not have the E/p requirement on the matched track. The track matching efficiency drops quickly in the EC region because the geometric acceptance of the CTF decreases as fewer layers are transversed by the charged particles.

candidates are identified using the 0.7 cone algorithm and are required to pass good jet requirements ($E_T > 25$ GeV, n90 > 1, f90 < 0.65, $0.05 <$ EM fraction < 0.7, CHF< 0.25, $N_{trk} \geq 5$ and Hotfraction< 0.5 [2]). The fake rate is then the fraction of those EM objects that are found to have a matching track. Figure 4.5 shows the fake rate as a function of $\not\!\!E_T$; the fake rate is almost constant for events with $\not\!\!E_T < 15$ GeV, and then it increases. The explanation is the sample is contaminated by W+jet events in the high $\not\!\!E_T$ region. The fake rate is determined using events with missing $E_T < 15$ GeV, the fake rate versus electron pseudorapidity is shown in Fig. 4.6.

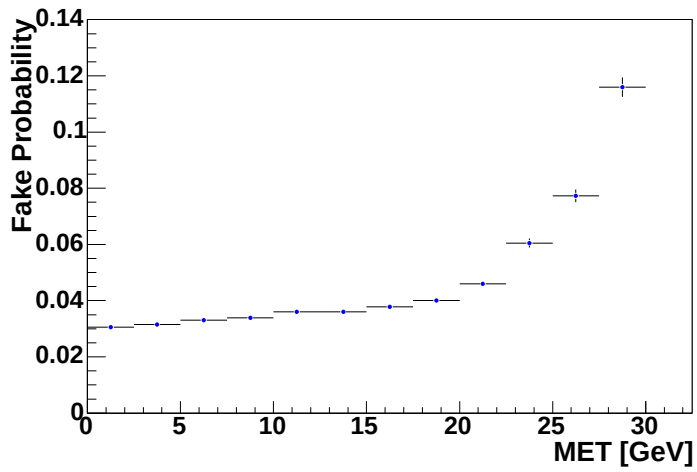

Figure 4.5: Fake track matching probability vs $\not\!\!E_T$ for both CC and EC region.

4.3 $Z \to ee$ Backgrounds

There are two major backgrounds for $Z \to ee$ events, the background from QCD multi-jets, where the jets fluctuate electromagnetically and fake electrons, and also the physics background from $Z \to \tau\tau$ events.

[2] E_T is the jet transverse energy; n90 is number of towers that contains 90% of jet transverse energy; f90 is the fraction of jet towers carrying 90% of jet transverse energy; EM fraction is the fraction of jet energy deposited in the EM part of the calorimeter; CHF is the fraction of jet transverse energy that was deposited in the coarse hadronic part of the calorimeter; N_{trk} is number of tracks matched with the jet; Hotfraction is the ratio of the transverse energy of the leading cell in the jet to the transverse energy of the second leading cell.

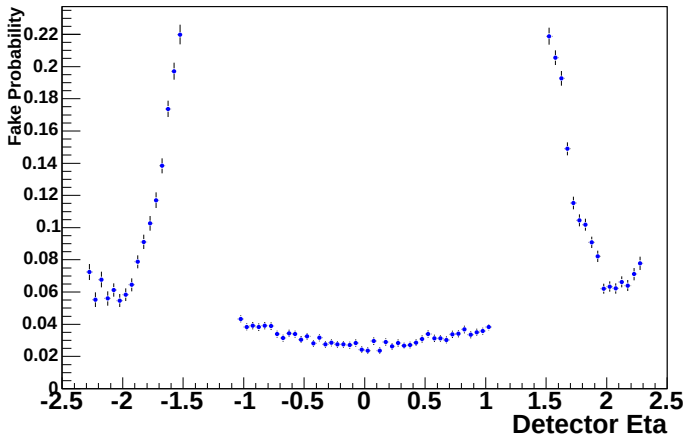

Figure 4.6: Fake track matching probability vs electron pseudorapidity.

4.3.1 QCD Backgrounds

The method of background subtraction has already been described in Sec. 4.1. For the $Z \to ee$ candidates, we require both electrons have matched track, and the QCD background is found to be negligible.

4.3.2 $Z \to \tau\tau$ Backgrounds

There is a potential background from $Z \to \tau\tau$ processes, where both taus decay to electrons. However, electrons from τ decays have a softer E_T spectrum and a small branching ratio $Br(\tau \to e\nu\nu)^2$, making this background negligible.

4.4 $W \to e\nu$ Backgrounds

Several processes can mimic the $W \to e\nu$ signal: QCD events in which one jet fakes the electron and the other jet is lost in an uninstrumented region of the detector; $Z \to ee$ decays in which one electron remains undetected, and $W \to \tau\nu \to e\nu\nu\nu$ decays.

4.4.1 QCD Backgrounds

QCD processes can fake the signature of a $W \to e\nu$ decay if a hadronic jet fakes the electron signature and the transverse momentum balance is mismeasured. In order to subtract the QCD background from the W candidates, we solve two linear equations using the number of W candidates with and without track match as well as the track matching efficiency and fake probability. The number of W bosons produced is extracted from the following equations:

$$N = N_W + N_{QCD} \tag{4.1}$$

$$N_{trk} = \epsilon_{trk} N_W + f_{QCD} N_{QCD} \tag{4.2}$$

Yielding

$$N_W = \frac{N_{trk} - f_{QCD} N}{\epsilon_{trk} - f_{QCD}} \tag{4.3}$$

where N_W is the true number of real W bosons, and N_{trk} and N are the numbers of W candidate events with and without the track matching requirement. f_{QCD} is the fake track matching probability and ϵ_{trk} is the track matching efficiency.

Since for this analysis we require the electron to have a matched track, the real W events and the QCD background in the sample we use should be:

$$\epsilon_{trk} N_W = \frac{\epsilon_{trk}(N_{trk} - f_{QCD} N)}{\epsilon_{trk} - f_{QCD}} \tag{4.4}$$

$$f_{QCD} N_{QCD} = \frac{f_{QCD}(\epsilon_{trk} N - N_{trk})}{\epsilon_{trk} - f_{QCD}} \tag{4.5}$$

To account for the variation in the track matching efficiency and fake rate with respect to pseudorapidity, the above equations are applied in bins of measured η^{det}. The tracking efficiency and fake track matching probability as a function of η^{det} are determined in Sec. 4.1 and Sec. 4.2.

4.4.2 $Z \to ee$ Backgrounds

To estimate the fraction of $Z \to ee$ events which satisfy the $W \to e\nu$ selection, we use a Monte Carlo sample of 0.8 million $Z \to ee$ events generated with PYTHIA and simulated with the full GEANT simulation. $Z \to ee$ events typically enter the W sample when one electron satisfies the W cuts while the second electron is lost or mismeasured, causing the event to have large $\not{E}_T$.

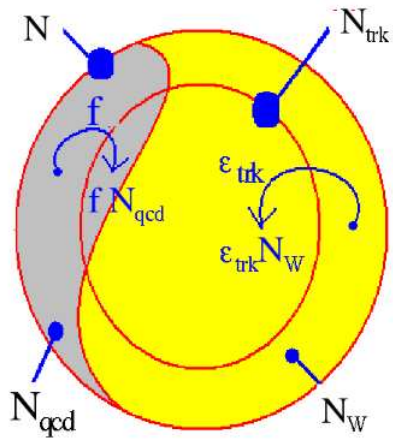

Figure 4.7: Concept of the method used to subtract QCD backgrounds from $W \to e\nu$ events.

An electron is most frequently mismeasured when it goes into the ICD regions, which are covered only by the hadronic section of the calorimeter. These electrons therefore cannot be identified, and their energy is measured in the hadronic calorimeter. A large $\vec{\not{p}}_T$ is more likely for these events than when both electrons hit the EM calorimeter. The GEANT Monte Carlo Z sample was modified to match the $Z \to ee$ data, the electron energies were smeared with a constant term of 4.2%, and also overlaid with underlying event. To select W candidates, we require that there is no second back-to-back track with $p_T > 15$ GeV; this removes a lot of $Z \to ee$ backgrounds where one electron hits the ICD region or the massless gap. The $Z \to ee$ background is found to be negligible.

4.4.3 $W \to \tau\nu$ Backgrounds

The decay $W \to \tau\nu \to e\nu\nu\nu$ is topologically indistinguishable from $W \to e\nu$ and is suppressed by the branching fraction of $\tau \to e\nu\nu$ and by the electron p_T cuts. We generate 0.8 million $W \to e\nu$ and 0.8 million $W \to \tau\nu$ events and then apply W selection criteria on both samples. Because of lepton universality, we assume that the cross section times branching ratio for $W \to e\nu$ and $W \to \tau\nu$ are the same, the $W \to \tau\nu \to e\nu\nu\nu$ fraction is thus found to be $(1.250 \pm 0.027)\%$.

Chapter 5

Overview of Monte Carlo Simulation

As can see from Sec. 1.4, the W boson width is extracted by comparing the measured W transverse mass distribution with ones generated by a Monte Carlo simulation. The PYTHIA (Version 6.202) event generator is used in this analysis to simulate $p\bar{p}$ interactions, particle production and decay. The generated events are then processed by a detector simulation package to add detector effects; we use a parameterized model [61] to incorporate all the main features of the DØ detector. Since neutrinos escape detection, in essence only two quantities are measured in W events: the electron momentum vector and the transverse momentum of the system recoiling against the W. Thus in the Monte Carlo simulation, we need to simulate the detector response and thus obtain the prediction of the observed electron and recoil momenta [16]. The simulated missing transverse momentum is derived from the total energy measurement in the event

$$\vec{\not{E}}_T(smear) = -\vec{p}_T^{\,e}(smear) - \vec{u}_T(smear) \tag{5.1}$$

where $\vec{\not{E}}_T(smear)$ is the smeared $\not{E}_T$, $\vec{p}_T^{\,e}(smear)$ the smeared electron transverse momentum and $\vec{u}_T(smear)$ the smeared recoil system. The basic concept of electron and recoil system smearing is described in this chapter, while the detailed modeling of the different components is described in the next two chapters.

5.1 EM Objects Simulation

After the PYTHIA generator generates $Z \to ee$ and $W \to e\nu$ events, electrons (photons) are extrapolated from the primary vertex to the third layer of the EM calorimeter. The energies of the generated electrons and any radiative photons, if they were present and retained their identity, are scaled by the measured EM energy scale. The generated transverse momenta and electron angle are then smeared according to the measured resolution. All efficiencies measured

in Chapter 4 are included in the Monte Carlo simulation. To simulate the detector response to an electron of energy E_0, we compute the observed momentum as

$$E(e) = R_{EM}(E_0) \otimes \sigma_{EM}(E_0) \tag{5.2}$$

where $R_{EM}(E_0)$ is the response of the electromagnetic calorimeter and σ_{EM} is the energy resolution of the electromagnetic calorimeter.

The energy response of the EM calorimeter is modeled using two parameters

$$E(e) = \alpha \times E_{gen} + \beta \tag{5.3}$$

and the resolution of the EM calorimeter is also modeled using two parameters

$$\frac{\sigma_{EM}(E_e)}{E(e)} = \sqrt{C_{EM}^2 + \frac{S_{EM}^2}{E(e)}} \tag{5.4}$$

The smeared electron energy is thus

$$E(e)(smear) = E(e) + x * \sigma_{EM}(E_e) \tag{5.5}$$

where x is a random variable from a normal gaussian distribution with zero mean and unit width. The calorimeter position resolution is modeled using two parameters:

$$\eta_{smear}^{det} = \eta_{gen}^{det} + y * \sigma_{\eta^{det}} \tag{5.6}$$

$$\phi_{smear}^{det} = \phi_{gen} + z * \sigma_{\phi^{det}} \tag{5.7}$$

where α is the EM energy scale and β EM energy offset, C_{EM} is the constant term and S_{EM} the sampling term for the EM calorimeter, $\sigma_{\eta^{det}}$ and $\sigma_{\phi^{det}}$ are the detector η and ϕ resolution y and z are two random variables from a normal gaussian distribution with zero mean and unit width.

5.2 Recoil System Simulation

The model for the particles recoiling against the W/Z boson has two components, a "hard" component, that models the p_T of the W/Z boson (denoted by $\vec{p}_T^{\,rec} = -\vec{p}_T^{\,W}$), and a "soft" component, that models detector noise and underlying events (denoted by $\vec{u}$). The transverse

momentum of the recoil system is taken to be the negative of the generated transverse momentum of the W boson; its magnitude is scaled by the product of the measured EM energy scale and the relative response of the hadronic and EM calorimeters. Smearing was added according to the jet energy resolution. For the soft component, we use the transverse momentum balance $\vec{\not{p}}_T^{mb}$ from a minimum bias event recorded in the detector, which mimics the debris in the event due to spectator parton interactions and the pile-up associated with multiple interactions. The hadronic content of $Z \to ee$ events is modeled in the same fashion as for $W \to e\nu$ events. The observed recoil transverse momentum is then given by

$$\vec{u}_T = -[R_{rec}(q_T) \otimes \sigma_{rec}(q_T)]\hat{q}_T + \alpha_{mb}\vec{\not{p}}_T^{mb} - \Delta u_{\parallel}\hat{p}_T(e) \tag{5.8}$$

where q_T is the generated value of the boson transverse momentum, R_{rec} is the response and σ_{rec} the resolution of the hadronic calorimeter, $\Delta u_{\parallel}$ is the transverse energy flow into the electron window due to underlying events and $\hat{p_T}(e)$ is the electron direction. α_{mb} is a correction factor that allows us to adjust the resolution to the data, and is roughly the number of additional minimum bias events overlaid on a W boson event.

For $R_{rec}(q_T)$, we have

$$R_{rec}(q_T) = \kappa \times q_T \tag{5.9}$$

and for $\sigma_{rec}(q_T)$, we have

$$\frac{\sigma_{rec}(q_T)}{q_T} = \sqrt{C_{had}^2 + \left(\frac{S_{had}}{\sqrt{q_T}}\right)^2} \tag{5.10}$$

where κ is the hadronic momentum response, and C_{had} and S_{had} are the constant term and sampling term for the hadronic calorimeter respectively.

Chapter 6

Electron Measurement and Simulation

In this chapter, I will discuss how we reconstruct the electron energy and how we simulate it in the fast Monte Carlo.

6.1 Electron Energy Measurement

The signals emerging from the calorimeter are digitized charge measurements from each cell; they need to be converted to energy. This conversion is extremely complicated and very important for the energy measurement.

In general, the relation between the energy and the measured ADC counts for an EM object in an n-layer sampling of a calorimeter is given by (in our case, $n = 5$ since we use the energy deposited on the four EM layers and the first FH layer):

$$E = \alpha \sum_i \beta_i \left[\sum_j (\lambda_j \ a_j + \gamma_j) \right] + \delta \tag{6.1}$$

where E is the true energy of an EM particle and the a_j's are the ADC counts for each readout calorimeter cells. The first sum runs over the number of layers, while the second sum runs over the number of readout cells for layer i. α is the overall energy scale, δ is the overall energy offset, β_i is the sampling fraction, λ_j converts ADC counts to GeV and γ_j is the non-linearity term for calorimeter cell j. In principle, α, δ, β_i, λ_j and γ_j depend on η and ϕ. Moreover, all of these quantities vary with time.

The first two constants (α and δ) are global parameters which can be adjusted by various "offline" calibration methods ($Z \to ee$, $J/\psi \to ee$, E/p, etc.). The sampling fraction β_i is determined from GEANT Monte Carlo simulation. The last two factors λ_j and γ_j, known as the "calibration constants" or ADC to GeV conversion constants, are actually the product of two factors: the charge produced per deposited MeV, and the conversion from ADC counts to input

charge. These two terms vary however in a broad range from channel to channel.

The steps in the conversion process are listed below in order:

- Pedestal subtraction and zero-suppression;
- ADC - GeV conversion;
- Sampling weights;
- Clustering algorithm;
- Geometrical corrections;
- EM scale calibration.

I will describe each step in this chapter in detail.

6.1.1 Pedestal subtration and zero-suppression

The distribution of ADC counts from each cell in the absence of beam is called its "pedestal" distribution. The mean of the pedestal distribution is called the pedestal. The energy deposited in the cell when hit by a particle is proportional to the difference between the energy read out and the pedestal. Therefore, to reconstruct the energy deposited in a cell, it is necessary to first subtract the pedestal, then multiply the result by a conversion factor which relates the energy measurement in ADC counts to the energy measurement in GeV. The pedestal distributions are determined from frequent pedestal calibration runs taken between stores, and the pedestal subtraction was performed online.

Even in the absence of a particle flux, due to the decay of uranium nuclei, electronic noise and the hardware pedestal cut (cut on integer ADC number), there are still many calorimeter cells that have signal. In order to control the size of the data, not all cells are read out in a given event. Hardware zero-suppression eliminates most cells ($\approx 90\%$) in a given event. The zero-suppression criteria are based on the pedestal distributions. To decide whether or not a cell was hit, the pedestal subtracted energy for that cell was required to be greater in magnitude

than 2.5 σ (In Run II, we use 2.0 σ online and 2.5 σ offline), where σ was the rms of the pedestal distribution for that cell. σ is usually around 25 MeV for EM layers and 40 MeV for FH layers. The σ of each channel in raw ADC counts and in MeV can be found at [62]. In Run I, because of the lower instantaneous luminosity and lower electronic noise, we used the 2.0 σ online cut only. Figure 6.1 shows the energy distribution for a calorimeter cell after pedestal subtraction and zero-suppression. The spectrum has an asymmetric tail from ionization caused by the intrinsic radioactivity of the uranium absorber plates [63]. The purpose of pedestal subtraction is to make the mean energy zero for each cell, that is

$$N_1\langle E_1\rangle + N_2\langle E_2\rangle + N_3\langle E_3\rangle = 0 \tag{6.2}$$

where $\langle E_1\rangle$, $\langle E_2\rangle$ and $\langle E_3\rangle$ are the average energies of the calorimeter cells within the interval $E < -2.5\ \sigma$, $-2.5\ \sigma < E < 2.5\ \sigma$ and $E > 2.5\ \sigma$ respectively, and N_1, N_2 and N_3 are the average number of events within each interval for a sample of minimum bias events. The hardware and software zero-suppression sets all calorimeter cells within $\pm 2.5\ \sigma$ of the pedestal to zero, thus forcing $\langle E_2\rangle = 0$ at readout. After zero-suppression, the pedestal distribution contributes on average a net energy to each cell, as can be seen from the following equation

$$N_1\langle E_1\rangle + N_3\langle E_3\rangle = -N_2\langle E_2\rangle \tag{6.3}$$

If the cell energy distribution is symmetric in the $\pm 2.5\ \sigma$ region, then $N_2\langle E_2\rangle = 0$, but in reality, the energy distribution is asymmetric. On average, $\langle E_2\rangle < 0$, thus the spectrum does not average to zero after zero-suppresssion. In effect the zero-suppression unphysically raises the energy of each calorimeter cell.

The zero-suppression contribution to the cell energy has been studied by analyzing non-zero-suppressed minimum bias events and zero-suppressed minimum bias events. The contribution was found to be +7.55 MeV per cell in Run I (2.0 σ) [16], the contribution for Run II is currently still under study.

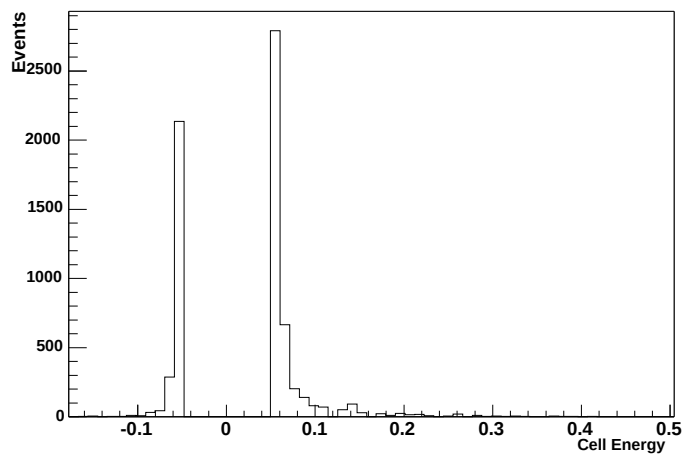

Figure 6.1: Energy distribution of a typical calorimeter cell for a sample of minimum bias events. The mean pedestal has been subtracted and the events in the empty region are removed by the zero suppression (2.5 σ).

6.1.2 ADC - GeV Conversion

The calibration constants λ_j and γ_j are calculated by means of an "electronic" calibration: a pulse of known amplitude is sent to the measuring chain and the ADC counts are measured giving the desired ratio. The offset term γ_j (also called the calorimeter non-linearity term) arises due to the analog samples being stored in SCA chips which are nonlinear over part of their range. The ability to calibrate the DØ calorimeter electronics is of prime importance for determining with optimal precision the energy of a particle, since a non-uniform response degrades both the scale and the resolution of the energy measurement. For the purpose of electronic calibration, a new pulser system was built [64]. It works as follows: an 18-bit DAC delivers a DC current to a 1 mH inductance. On a command signal whose arrival time is defined by a programmable delay (256 steps of $\sim$ 1.6 ns), a switch diverts the current from the generator to ground, the current stored in the inductance then decays into a resistor and flows to the preamplifier input as an exponential signal (1 DAC unit = 11.5 μV, 40 ns rising time, 450 ns decaying time). The signal can be sent to a set of preselected preamplifiers and allows us to measure the ratio of input

voltage to ADC counts. Figure 6.2 shows the schematic view of the calorimeter calibration system and the pulser system.

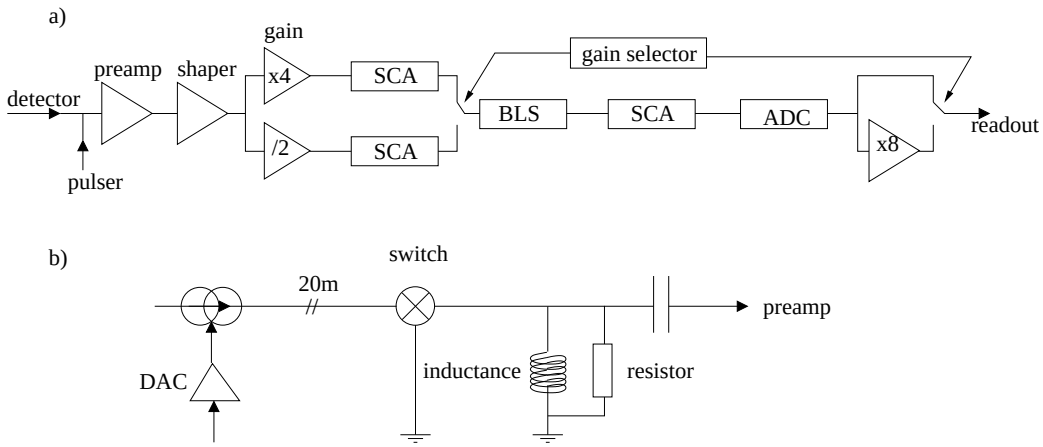

Figure 6.2: Schematic diagrams of a) the calibration system and b) the pulser system.

The two terms (λ_j and γ_j) are measured by a comparison of the electronics response (in ADC counts) vs the pulse height (in DAC units) for each gain path ($\times 1$ and $\times 8$). To first approximation, the ADC response to the DCA calibration is linear, as shown on Fig. 6.3. Figure 6.4 shows the residuals of the readout to the linear fit. In both plots you can see the saturation for large signal and a non-linear response for low signals. The measurements of the non-linearities in the response of the calorimeter are described in detail in [42]. To correct for the non-linearities, the following parameterization is used

$$u_8(v) = gav + \epsilon(gav) \tag{6.4}$$

$$u_1(v) = av + 8\epsilon(av/8) \tag{6.5}$$

where ϵ is a universal function fitted to all channels, and v is the input voltage injected into the readout channel, which is assumed to be linear with an offset. The real numbers $g \approx 1$ and a may be different for each readout channel. After applying this correction, the residuals are better than ± 5 ADC over the whole range for both gain paths. The effect of this correction on the energy reconstruction results in a shift of 200 MeV for energies above 500 MeV when read out with the gain 8 and a shift of 1 GeV when read out with gain 1.

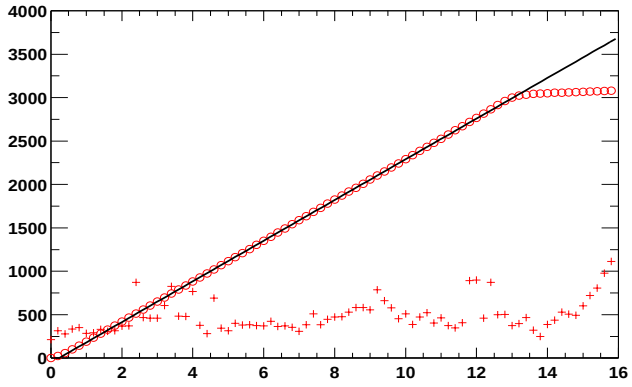

Figure 6.3: ADC response to the calibration signal (DAC). The noise multiplied by 100 is indicated by crosses.

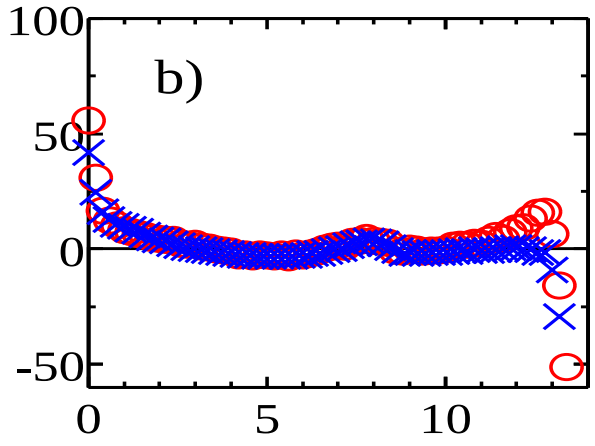

Figure 6.4: Residual of data with respect to a straight line fit for a cell in the EM calorimeter, circles are $\times 1$ gain, crosses the $\times 8$ gain channel.

6.1.3 Sampling Weights

The DØ calorimeter is a sampling calorimeter, since a very small fraction of the electron energy is deposited in the liquid argon and then read out; we need to apply sampling weights to get the correct electron energy. In Eqn. 6.1, the sampling weights β_i are the ratio of the energy deposited in liquid argon to incident energy. In Run I, we used test beam data to minimize [16]

$$\chi 2 = \sum \left(\frac{p_{beam} - \sum_{i=1}^{5} \beta_i L_i}{\sigma_{EM}} \right)^2 \tag{6.6}$$

where the sum runs over all events, p_{beam} is the beam energy, L_i is the live energy deposited in the liquid argon for layer i, and σ_{EM} is the energy resolution given in Eqn. 2.2. The parameters β_1 - β_4 weight the four EM layers and β_5 the first FH layer. In Run II the sampling weights are determined by studying single energy electrons and pions from the full GEANT Monte Carlo simulation and then minimizing the function [65]

$$\chi 2 = \sum_{\text{events}} (E_{true} - \sum_{i=1}^{5} \beta_i L_i)^2 \tag{6.7}$$

where E_{true} is the true energy of the electron or pion. The sampling weights for each layer are given in Table 6.1.

	EM1	EM2	EM3	EM4	FH1
CC	31.1991	9.3992	25.7156	28.0328	24.8846
EC	32.9612	17.0792	33.1245	39.5006	27.4569

Table 6.1: Sampling weights for the four EM layers and the first fine hadronic layer.

6.1.4 Clustering Algorithm

After the pedestal subtraction, zero-suppression, and ADC to GeV conversion, we have a list of calorimeter towers with significant energy deposition. These towers serve as the seeds for the subsequent jet and electron cluster finding algorithm. The highest E_T EM towers are selected as the starting points of the preclusters. Adjacent EM towers above 50 MeV are added to a

precluster if they are within a window of 5×5 in $i\eta \times i\phi$ (CC) or within a cone of 10 cm radius in EM3 (EC). The centroid of the cluster is recalculated and repeated until the final cluster does not change. The energy is then computed from the signals in all cells of this EM cluster.

6.1.5 Geometrical Corrections

There are two main reasons that the electron energy is not completely recovered in the calorimeter: the presence of material in front of the calorimeters and the presence of regions not covered by precision calorimetry. For example, the η edges of the CC and EC calorimeters, and the ϕ edges between 2 of the 32 CC modules. Corrections are applied to recover the energy loss in the cases mentioned above. These corrections are called "geometrical" corrections since they deal exclusively with the geometry of the detectors. They are directly deduced from Monte Carlo studies using single energy electron samples after GEANT Monte Carlo simulation [66]. The energy loss is found to vary in η from 0.2 GeV for 5 GeV electrons (4%) to 3 GeV for 250 GeV electrons (1.2%), and vary in ϕ from 1.5 GeV for 5 GeV electrons (30%) to 30 GeV for 250 GeV electrons (12%). The energy loss is parameterized as a function of η and ϕ and corrections are applied in both data and Monte Carlo.

6.1.6 EM Scale Calibration

Suppose α varies for each readout cell, in the following way:

$$\alpha = \alpha(0)(1+\epsilon) \tag{6.8}$$

where ϵ is the EM scale correction factor. The aim is to determine $\epsilon(\eta, \phi)$ simultaneously in different η and ϕ sectors of the calorimeter. We use $Z \to ee$ events produced in Drell-Yan processes and minimize the likelihood based on the invariant mass distribution of the e^+e^- pairs. Since we are limited by the available $Z \to ee$ data, the calibration was done in 12 zones (according to 12 ADC crates):

$$\bar{m}_i^2 = m_i^2(1+\epsilon_{1k})(1+\epsilon_{2l}) \tag{6.9}$$

where ϵ_{1k} and ϵ_{2l} are the calibration constants for zone k and l where the first electron is located

in zone k and the second electron located in zone l, m_i and $\bar{m}_i$ are the invariant mass of the lepton pair before and after the EM scale correction. ϵ is found to be the order of several percent ($\sim 2-4\%$) and has a strong dependence on η and ϕ [67].

6.2 Determination of Electron Energy Scale

As mentioned in Sec. 6.1, the electron energy is measured as the energy in a window of 5×5 towers, consisting of the four EM layers and FH1, centered on the tower in which the electron deposited the most energy. We use five parameters α, β, C_{EM}, S_{EM} and N_{EM} (discussed in Sec. 5.1) to simulate the detector response to the electrons.

Since the electrons coming from Z decay have a wide energy distribution, we can just use the EM clusters from the $Z \to ee$ resonance to determine the energy scale α and energy offset β. We apply the Z selection criteria to the data sample and require both electrons to have a matched track to get pure signal events; the QCD background is totally negligible. We compare data and the fast Monte Carlo simulation, and then use three different methods to determine the two parameters.

6.2.1 Binned Maximum Likelihood Method

We bin the invariant mass distribution for the Monte Carlo and data from 75 to 105 GeV, and then calculate a binned likelihood function:

$$L = -\sum_{bins}[x_i \times \ln(y_i) - y_i - \ln(x_i!)] \tag{6.10}$$

where x_i is the number of data points in bin i and y_i is the number of the Monte Carlo events in bin i. We first fix the other smearing parameters to some reasonable values and only vary the electron energy scale α (or energy offset β), and for each value of α (or β) evaluate L. To determine a minimum we then fit L to a quadratic function. Figure 6.5 and Fig. 6.6 show the results for all CCCC candidates. The results are: $\alpha_{CC} = 1.0054 \pm 0.0010$ and $\beta_{CC} = 0.038 \pm 0.048$ GeV.

Since α and β are strongly correlated, we do a consistency check in the following way: first we determine the energy offset and then fix the energy offset using the value determined and vary energy scale to determine the energy scale; the results are consistent with each other.

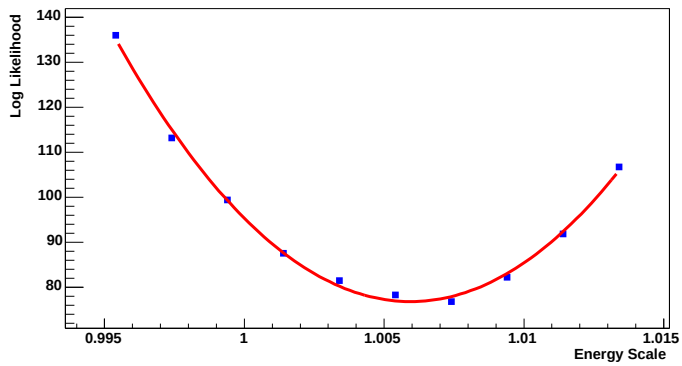

Figure 6.5: Electron Energy Scale vs likelihood.

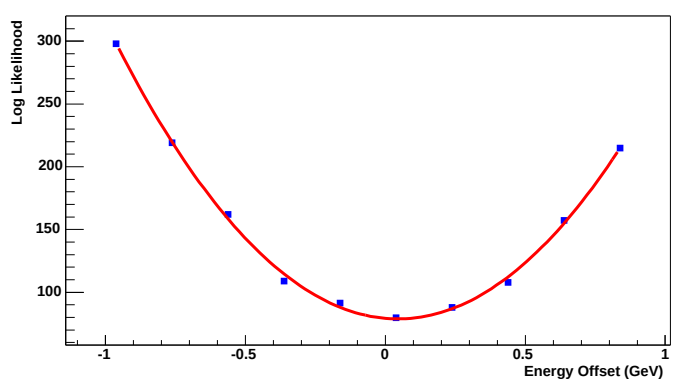

Figure 6.6: Electron Energy Offset vs likelihood.

6.2.2 $< M_{ee} >$ Method

As a cross check, we also fit for the energy scale and energy offset by comparing the mean value of the data invariant mass distribution with the mean value of the Monte Carlo. In order to avoid the fluctuations in the tail region, we only use events that are very close to the Z peak; hence we choose the mass window [75, 105] GeV with 1.5 GeV bins and calculate $< M_Z >$.

Figure 6.7 and Fig. 6.8 show $< M_Z >$ for the Monte Carlo as a function of the energy scale α and energy offset β for CCCC Z candidates. The mean value of the data is also shown on the plot. From here, the results are: $\alpha_{CC} = 1.0055^{+0.0014}_{-0.0015}$ and $\beta_{CC} = 0.010^{+0.055}_{-0.057}$ GeV.

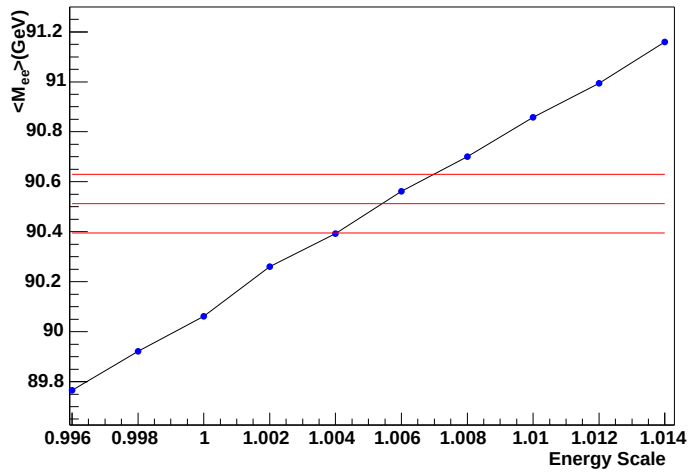

Figure 6.7: Electron Energy Scale vs $< M_{ee} >$.

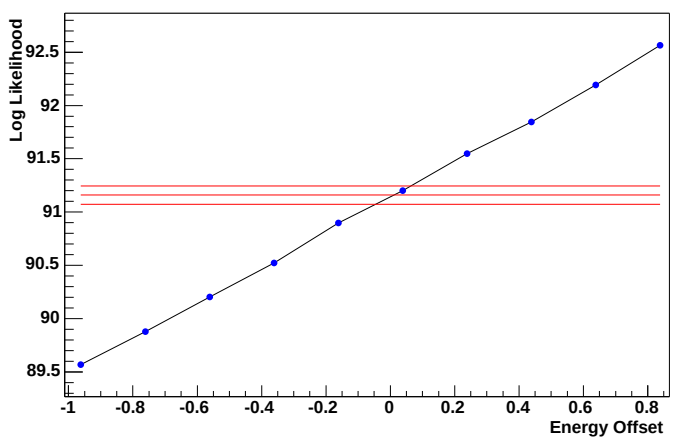

Figure 6.8: Electron Energy Offset vs $< M_{ee} >$.

6.2.3 Kolmogorov-Smirnov Test

Here we use Kolmogorov-Smirnov statistic (KS) to evaluate how well the Monte Carlo reproduces the data. The KS value is calculated without binning the data or the Monte Carlo and this allows us to check that the binning of the data in the above two sections does not significantly increase the statistical uncertainties. To calculate the KS value, we form the integrated distribution of M_Z for data and Monte Carlo. For data and Monte Carlo, we only consider events between 80 to 100 GeV (to minimize the effect of bin size, we use 20,000 bins for this 20 GeV region). Figure 6.9 shows the integrated distributions for data and MC.

The KS value is defined to be the maximum vertical distance between the Monte Carlo integrated distribution and the data integrated distribution. A KS value of 0 would mean perfect agreement between the two distributions.

Figures 6.10 and 6.11 show the KS value vs α and β for CCCC Z candidates. From here, we have $\alpha_{CC} = 1.004$ and $\beta_{CC} = 0.00$ GeV. Unfortunately for KS test, we can not get a statistical uncertainty for each parameter.

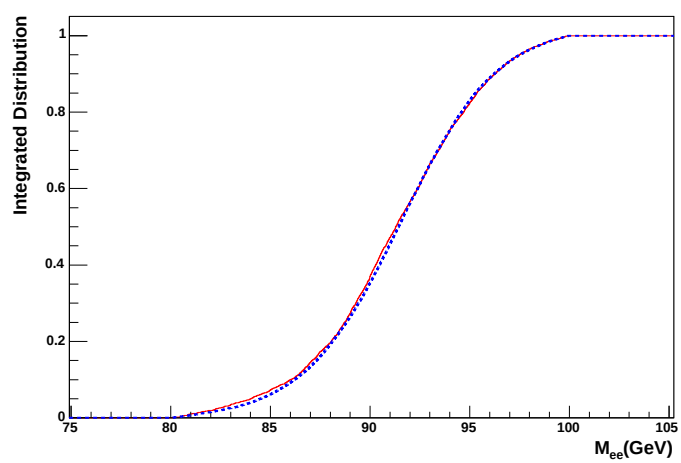

Figure 6.9: Integrated distribution of M_{ee} for data and MC, dashed line for data, solid line for MC.

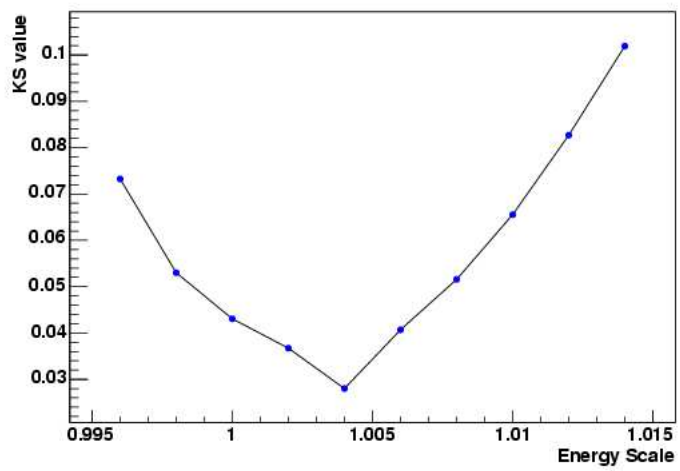

Figure 6.10: Electron Energy Scale vs KS value.

6.2.4 Final Results for EM Energy Scale and Energy Offset

We determined the EM energy scale and energy offset using three different methods; they all give consistent results. The $< M_{ee} >$ method only uses the mean value of the invariant mass distribution and Kolmogorov-Smirnov Test can not give uncertainties. In the fast Monte Carlo program, we use the values obtained from Binned Maximum Likelihood Method:
$\alpha_{CC} = 1.0054 \pm 0.0010$ and $\beta_{CC} = 0.038 \pm 0.048$ GeV.

6.3 Determination of Electron Energy Resolution

As discussed in Sec. 2.2.4, the sampling term is known to high precision from test beam studies and is 15% GeV$^{1/2}$ for CC electrons. Since we still use the Run I calorimeter and just add more material before it, we assign 3% for the uncertainty on the sampling term. The value of the constant term is determined using two methods:

6.3.1 Binned Maximum Likelihood Method

We also use the binned likelihood method to determine the EM energy resolution, this time we fix the energy scale and energy offset values to the best values and only change the smearing

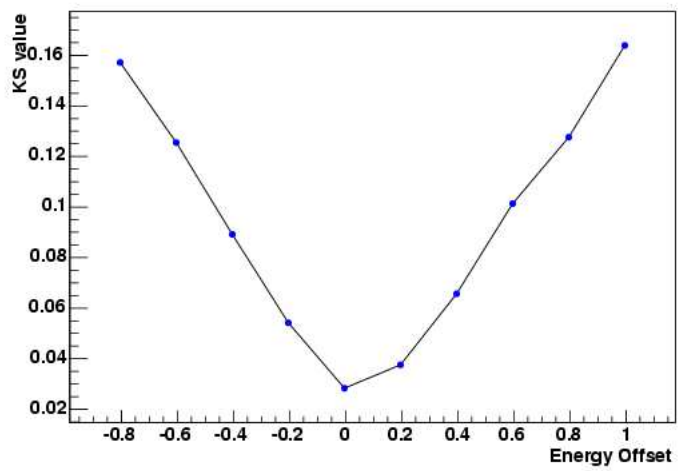

Figure 6.11: Electron Energy Offset vs KS value.

parameters used in modeling the energy resolution. The likelihood vs the constant term for CCCC Z candidates is shown at Fig. 6.12, and the constant term is determined to be $C_{CC} = (4.20 \pm 0.23)\%$.

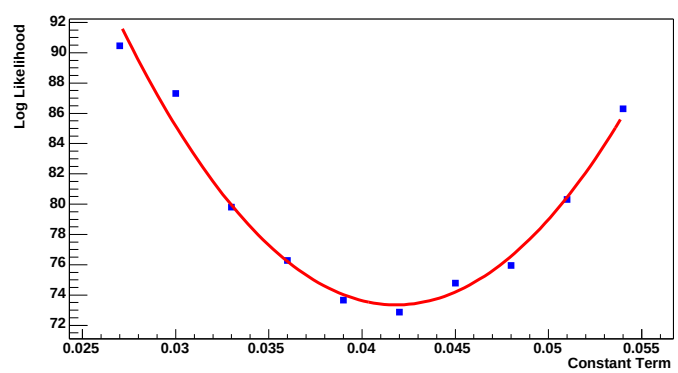

Figure 6.12: Constant Term vs likelihood.

6.3.2 Z Width Method

The constant term can also be measured from the width of the Z's. The observed width has contributions from the intrinsic Z width and from detector resolution. The intrinsic Z width is known to very high precision from the LEP experiments, and the detector component is

dominated by the energy resolution of the electromagnetic calorimeter.

To determine the constant term, Monte Carlo $Z/\gamma^* \to ee$ experiments are generated with different values of C. The predicted invariant mass distribution for each experiment is fit to a Breit-Wigner convoluted with a gaussian. The Breit-Wigner width is fixed to its measured value of 2.5 GeV, but the gaussian width is allowed to float. The data is fit in the same way, and C in the simulation is adjusted until the Monte Carlo and data distributions have the same width. Figure 6.13 shows the observed invariant mass distribution fitted with a Breit-Wigner convoluted with a Gaussian function, and Fig. 6.14 shows the rms of the gaussian that is obtained when the same procedure is applied to the Monte Carlo as a function of the CC constant term, along with the result from the data. The intersection of the two gives the constant term. The constant term in the CC is thus determined to be $(4.14 \pm 0.26)\%$, with the uncertainty being dominated by the statistics of the $Z \to ee$ sample. It is consistent with the result we got from the maximum likelihood method.

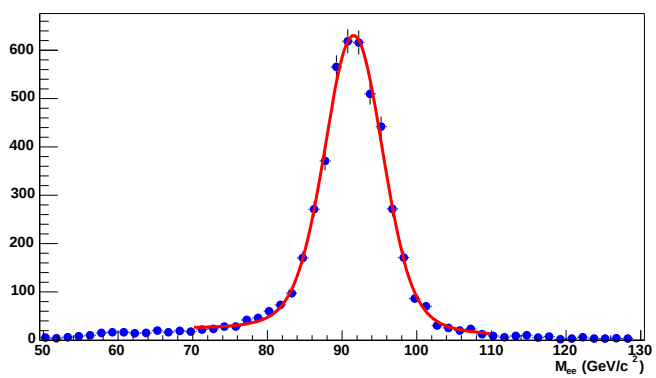

Figure 6.13: The observed invariant mass distribution for CC-CC Z candidates fitted with a Breit-Wigner convoluted with a Gaussian function.

6.3.3 Final Results for EM Energy Resolution

We use two different methods to determine the EM energy resolution; both of them give consistent results. Since the Z width method only uses the width of the invariant mass

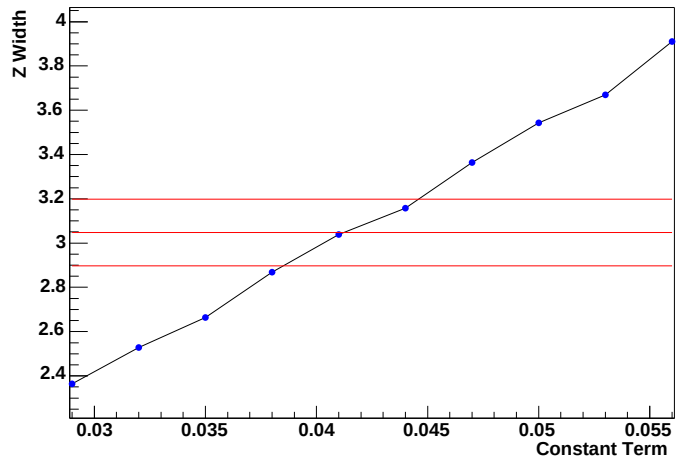

Figure 6.14: Constant Term vs Z Boson Width.

distribution, while Binned Maximum Likelihood Method uses the information for each bin, in the fast Monte Carlo program, we use the values obtained from the Binned Maximum Likelihood Method: $C_{CC} = (4.20 \pm 0.23)\%$. Compared with Run I, the energy resolution of the EM calorimeter is much worse. Possible sources for this are discussed in Appendix A.

6.4 Consistency Check of Electron Energy Simulation using E/p

The electron energy scale and electron energy resolution are also checked by comparing the lineshape of the observed E/p distribution for electrons from $W \to e\nu$ events to a Monte Carlo prediction of this distribution. The electron may lose energy to photons either as it is created from the W decay or as it passes through material. Since the associated photons are usually collinear with the electron, they often form one EM cluster in the calorimeter; accordingly the energy response is relatively unaffected by the bremsstrahlung process. However the electron momentum, p, measured by the tracker is typically lower than the electron energy E measured by the calorimeter, producing a long tail in the E/p distribution.

For events in the peak region, the peak position is determined by the electron energy scale and track momentum response; the width is determined by the electron energy resolution and track

momentum resolution. The electron energy scale and energy resolution are determined as described before, using the maximum likelihood method. The track momentum response and track momentum resolution are determined using $J/\psi \to \mu\mu$ and $Z \to \mu\mu$ events [85].

Figure 6.15 shows the comparison of the E/p lineshape between data and Monte Carlo simulation. The peak position of E/p is very sensitive to the electron energy scale and track momentum scale, the width is sensitive to the electron energy resolution and track momentum resolution, while the high tail region is sensitive to the amount of material before the solenoid. Good agreement between data and MC simulation is observed. The low E/p events ($E/p < 0.9$) are the result of a pathology in the measurement of tracker p_T, and is further discussed in Appendix B.

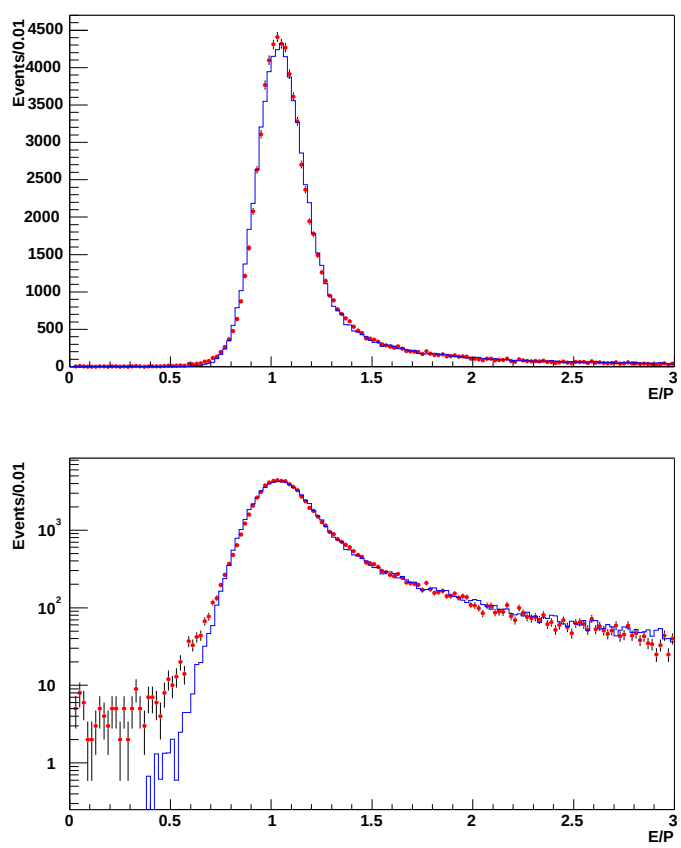

Figure 6.15: E/p distribution for W events (Dots for data, line for the Monte Carlo simulation (Top: linear scale; Bottom: log scale).

6.5 Determination of Calorimeter Position Resolution

As mentioned before, the shower centroid of an EM cluster is determined from the energy depositions in the third EM layer by computing the weighted mean of the position $\vec{x}_i$ of the cell centers:

$$\vec{x}_{cal} = \frac{\sum_i w_i \vec{x}_i}{\sum_i w_i} \tag{6.11}$$

The weights are given by

$$w_i = \max(0, w_0 + \log\left(\frac{E_i}{E(e)}\right)) \tag{6.12}$$

where E_i is the energy in cell i, w_0 is a parameter which depends upon $\eta(e)$, and $E(e)$ is the energy of the electron. We calibrate the algorithm using Monte Carlo electrons simulated using GEANT. If an EM cluster is found to have a matched track, the electron direction is then given by the direction of the matched track. The position resolution of the EM calorimeter is measured as the root mean square of the difference in the calorimeter and track position distributions. The η and ϕ resolutions were found to be $\sigma_\eta = 0.0070 \pm 0.0040$ and $\sigma_\phi = 0.0070 \pm 0.0035$ radian.

6.6 Radiative Decay

Radiation from the decay electron or the W boson biases the electron p_T shape and also the transverse mass shape, and thus will bias the W width measurement. For example, if the decay electron radiates a photon and the photon is well enough separated from the electron so that its energy is not included in the electron energy or if an on-shell W boson radiates a photon and therefore is off shell when it decays, the measured width is biased low. The parameter used in the modeling of radiative decays to decide if the photon retains its identity is the minimum separation $\Delta R(e\gamma)$ between the electron and photon (where $\Delta R(e\gamma) = \sqrt{[\eta(e) - \eta(\gamma)]^2 + [\phi(e) - \phi(\gamma)]^2}$). In general radiation shifts the Z boson invariant mass and also the W transverse mass down, because for a fraction of the events the photon energy is subtracted from the electron. The momentum of a photon with $\Delta R(e\gamma) < R_0$ is added to the electron momentum, while for $\Delta R(e\gamma) \geq R_0$ a photon is considered part of the recoil

momentum. We use $R_0 = 0.2$, which is the approximate size of the window in which the electron energy is measured and the uncertainty is assigned to be ± 0.1.

6.7 Electron Simulation Results

Figure 6.16 to Fig. 6.18 show the invariant mass distribution for $Z \to ee$ events, as well as electron p_T spectrum and p_T^Z from the Z sample.

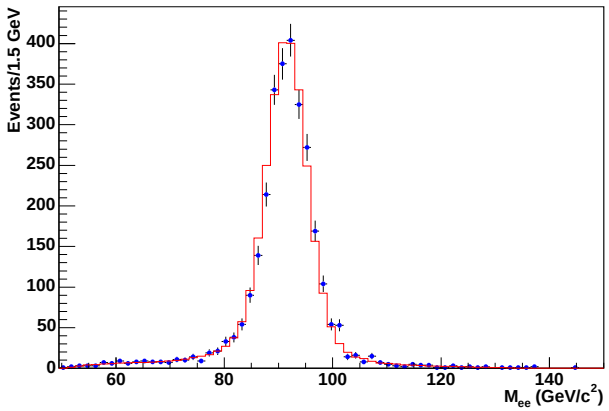

Figure 6.16: Invariant Mass distribution for $Z \to ee$ events (Dots for data, line for MC).

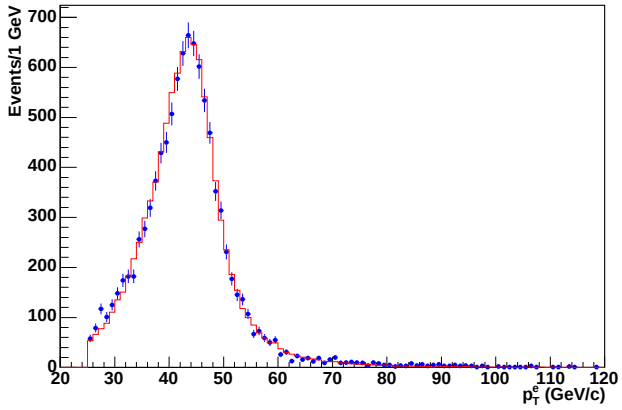

Figure 6.17: Electron p_T distribution for $Z \to ee$ events (Dots for data, line for MC).

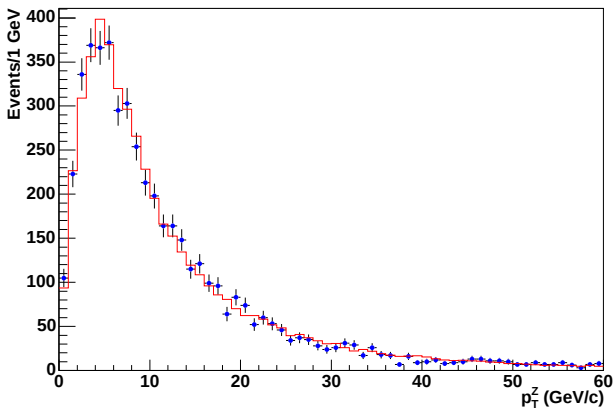

Figure 6.18: p_T^Z for $Z \to ee$ events (Dots for data, line for MC).

Chapter 7

Recoil Measurement and Simulation

In this chapter, the recoil momentum measurement is discussed.

7.1 Hadronic Momentum Response

The energy scale of the measured recoil momentum differs from the electron energy scale because the recoil measurement also includes energy from hadronic showers and suffers from loss of energy in uninstrumented regions of the calorimeter. The response of the hadronic calorimeter relative to the response of the electromagnetic calorimeter was determined from $Z \to ee$ events. In $Z \to ee$ events the transverse momentum of the Z boson, $\vec{p}_T^{\,Z}$, can be obtained from either the measurement of the transverse momenta of the two electrons, $\vec{p}_T^{\,ee}$, or from the recoil activity in the event $-\vec{p}_T^{\,rec}$. To minimize the effect of the hadronic momentum response relative to the electromagnetic energy scale, the momentum imbalance was measured with respect to the (η, ξ)-coordinate system as first introduced by UA2 [71]. The η axis is defined as the bisector of the two electron transverse directions. In the transverse plane, the axis orthogonal to the η axis is the ξ axis. Figure 7.1 illustrates these definitions.

The determination of the hadronic momentum response requires selecting $Z \to ee$ events with the same event topology as the $W \to e\nu$ events. $Z \to ee$ events were selected with at least one electron in the central calorimeter, while the other electron can be in the CC or EC regions. As a consistency check, Z boson events with both electrons in the central calorimeter have been used and a consistent result for the hadronic energy scale was observed. Three related determinations of the hadronic energy response relative to the electromagnetic response have been carried out:

- The first method of obtaining the calorimeter response used was the measurement of the $\vec{p}_T^{\,rec} \bullet \hat{\eta}$ as function of $< \vec{p}_T^{\,ee} \bullet \hat{\eta} >$, shown in the left plot of Fig. 7.2. The slope is $\kappa = 0.67 \pm 0.02$.

- A second method was the measurement of $< (\vec{p}_T^{\,ee} + \vec{p}_T^{\,rec}) \bullet \hat{\eta} >$, as a function of $\vec{p}_T^{\,ee} \bullet \hat{\eta}$ as shown in the right plot of Fig. 7.2; the slope is 0.33 ± 0.02. From this we also determine κ to be 0.67 ± 0.02.

- The hadronic momentum response κ was also determined using a third method which yielded both the hadronic momentum response and the magnitude of the underlying event vector $\vec{U}_T$. The transverse momentum balance in $Z \to ee$ events is given by

$$\vec{p}_T^{\,e1} + \vec{p}_T^{\,e2} + \vec{\not{E}}_T = -\vec{p}_T^{\,rec} - \vec{U}_T \tag{7.1}$$

Squaring both sides, one finds for the average

$$< |\vec{p}_T^{\,e1} + \vec{p}_T^{\,e2} + \vec{\not{E}}_T|^2 > = < |\vec{p}_T^{\,rec} + \vec{U}_T|^2 > = \kappa^2 |\vec{p}_T^{\,ee}|^2 + |\vec{U}_T|^2 \tag{7.2}$$

assuming again that $|\vec{p}_T^{\,rec}| = \kappa |\vec{p}_T^{\,ee}|$. The cross term on the right-hand side averages to zero since the underlying event vector is randomly distributed with respect to the Z boson recoil system. Figure 7.3 shows the distribution of $|\vec{p}_T^{\,e1} + \vec{p}_T^{\,e2} + \vec{\not{E}}_T|^2$ versus $|\vec{p}_T^{\,ee}|^2$ for $Z \to ee$ events. The straight line is a fit to the data and yields $\kappa = 0.63 \pm 0.01$, which is slightly lower than the value determined using the other two methods, and which may indicate we cannot neglect the cross term.

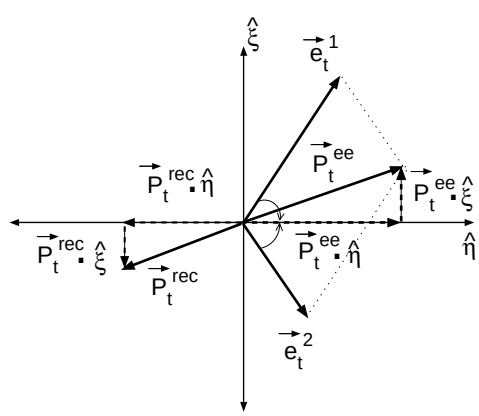

Figure 7.1: Definition of η and ξ axis for $Z \to ee$ events.

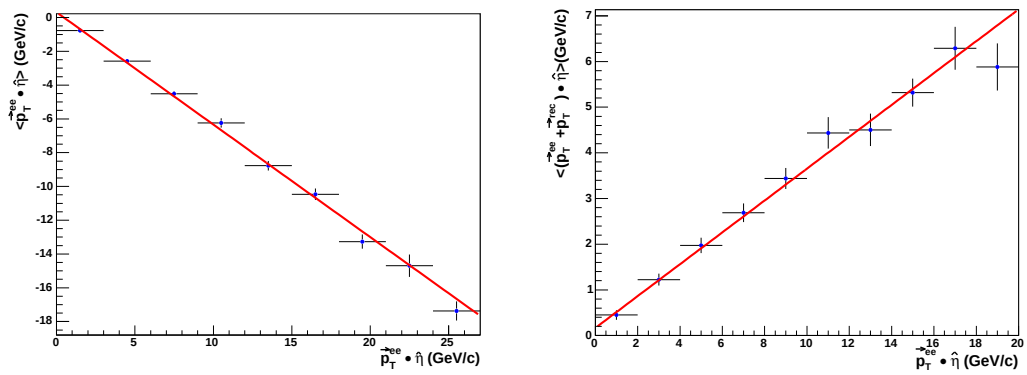

Figure 7.2: Average $\vec{p}_T^{\,rec} \bullet \hat{\eta}$ versus $\vec{p}_T^{\,ee} \bullet \hat{\eta}$ for $Z \to ee$ events, the line is a linear fit (Left); Average $\hat{\eta}$ imbalance versus $\vec{p}_T^{\,ee} \bullet \hat{\eta}$ for $Z \to ee$ events, the line is a linear fit. (Right)

7.2 Hadronic Energy Resolution

The W/Z recoil energy is treated as a single hadronic jet in the fast Monte Carlo. The hadronic energy resolution is parameterized in the same way as the electron energy resolution. From studies done by the Jet Energy Scale (JES) group [70], the resolution was found to have a constant term of 0.05 ± 0.01 and a sampling term of 0.80 ± 0.20 GeV$^{1/2}$.

7.3 $u_{\|}$ Efficiency

The recoil of the W boson may affect the electron identification, especially if the recoil system is close to the electron. A measurement of the event selection biases, due to the electron isolation cut, can be obtained by studying the projection of the momentum recoil along the electron direction ($u_{\|}$) [72]:

$$u_{\|} = \vec{p}_T^{\,rec} \bullet \hat{e} \tag{7.3}$$

where $\hat{e}$ is a unit vector in the electron direction. $u_{\perp}$ is the projection on the direction perpendicular to the electron direction and is defined as:

$$u_{\perp} = \vec{p}_T^{\,rec} \bullet [\hat{e} \times \hat{z}] \tag{7.4}$$

Figure 7.4 illustrates these definitons. A bias in the electron identification as function of $u_{\|}$

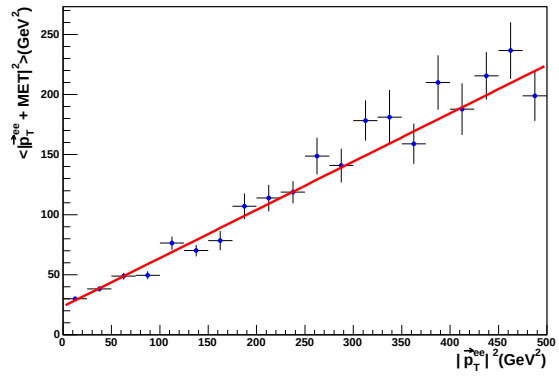

Figure 7.3: Distribution of the average $|\vec{p}_T^{e1} + \vec{p}_T^{e2} + \not{E}_T|^2$ versus $|\vec{p}_T^{ee}|^2$ for $Z \to ee$ events, the line is a linear fit.

would distort the lepton p_T spectra. For example, an inefficiency in the electron identification for high positive values of $u_\parallel$, when the recoil is close to the electron, would result in a harder p_T^e and a softer p_T^ν spectrum.

The $u_\parallel$ efficiency is determined by studying the behavior of the isolation of electrons from W decays. Figure 7.5 shows the average electron isolation quantity f_{iso} versus $u_\parallel$ for the signal electron. For negative values of $u_\parallel$, when the recoil jet is opposite the electron, the mean isolation is constant. This indicates that, as expected, for these event topologies, the recoil system does not affect the electron. For positive values of $u_\parallel$ the mean isolation $\langle f_{iso} \rangle$ increases with $u_\parallel$. This indicates that there is a flow of energy in the direction of the recoil jet. The $u_\parallel$ efficiency can be determined by studying the distribution of the isolation quantity for different $u_\parallel$ ranges. To remove QCD background, we apply tight electron requirements on the electron (except isolation cut) and also require $\not{E}_T > 25$ GeV and $p_T^W < 15$ GeV. Figure 7.6 shows the distribution of the isolation variable for six different $u_\parallel$ ranges. Then, for each $u_\parallel$ bin, we apply the isolation cut $f_{iso} < 0.15$, and the fraction of events with the isolation quantity f_{iso} above 0.15 is the inefficiency due to the recoil jet spoiling the electron signature. The efficiency as a function

of $u_{\parallel}$ is shown in Figure 7.7; the line is a fit to a function of the form

$$\epsilon(u_{\parallel}) = \epsilon_0 \begin{cases} 1 & \text{for } u_{\parallel} < u_0; \\ 1 - s(u_{\parallel} - u_0) & \text{otherwise.} \end{cases}$$

The parameter ϵ_0 is an overall efficiency which is inconsequential for this measurement, u_0 is the value of $u_{\parallel}$ at which the efficiency starts to decrease as a function of $u_{\parallel}$, and s is the rate of decrease. We obtain the best fit for $\epsilon_0 = (98.48 \pm 0.06)\%$, u_0=-0.908 ± 0.599 GeV and $s = 0.004364 \pm 0.000587$ GeV^{-1}.

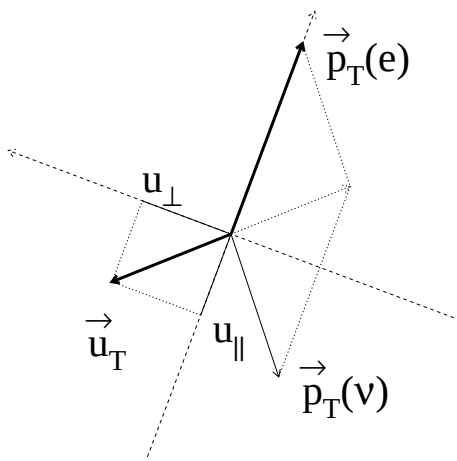

Figure 7.4: Definition of $u_{\parallel}$ and $u_{\perp}$ for $W \to e\nu$ events.

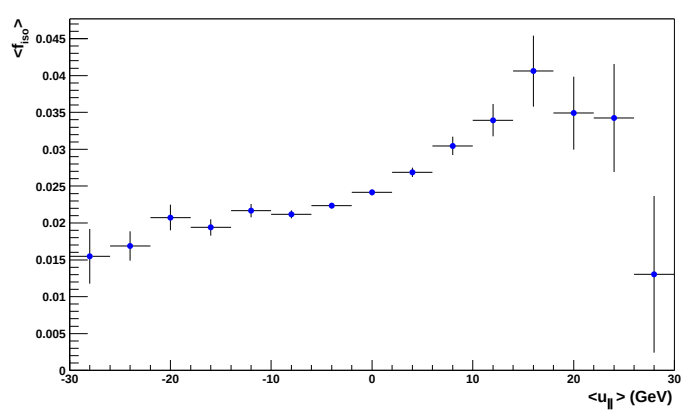

Figure 7.5: Average isolation f_{iso} versus $u_{\parallel}$ for signal electrons from W decays.

$u_{\parallel}$ range (GeV)	$< u_{\parallel} >$ (GeV)	efficiency(%)
$u_{\parallel} \leq -10$	-15.17	98.82 ± 0.13
$-10 < u_{\parallel} \leq -5$	-7.02	98.53 ± 0.10
$-5 < u_{\parallel} \leq 0$	-2.47	98.46 ± 0.08
$0 < u_{\parallel} \leq 5$	1.98	97.22 ± 0.14
$5 < u_{\parallel} \leq 10$	6.88	95.35 ± 0.37
$u_{\parallel} > 10$	13.54	91.76 ± 0.89

Table 7.1: $u_{\parallel}$ Efficiency.

7.4 Underlying Event Contribution

As discussed in Sec. 5.2, in the data the contribution from the underlying event cannot be separated from the measured recoil energy, and it affects the magnitude of the recoil measurement as well as its resolution. In the fast Monte Carlo simulation, the underlying event for W and Z events is modeled using collider minimum bias events, which mimic the debris in the event due to the spectator interactions and the pile-up associated with multiple interactions. The use of minimum bias events properly includes any residual energy which might be present from previous crossings as well as detector effects. To model the pileup correctly as a function of luminosity, we need to take minimum bias events at the same luminosities as the W events. To model the detector resolution correctly, the minimum bias events must have the same interaction multiplicity spectrum as the W events, which implies the same luminosity as the W events. Figure 7.8 shows the instantaneous luminosity profile for minimum bias events and W events. There is clearly a difference between the two luminosity profiles. We, therefore, weight the minimum bias events so that their luminosity profile approximates that of the W events. We measured the x and y component of the MET distribution for minimum bias events after luminosity reweighting; Figures 7.9 and 7.10 show the x, y components and also the $\not\!\!E_T$ distribution measured from the minimum bias events; the mean value of $\not\!\!E_T$ is found to be

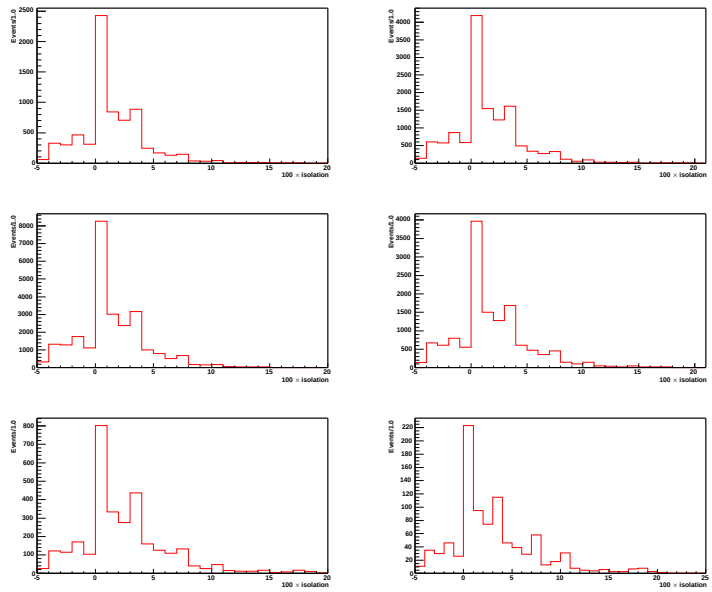

Figure 7.6: Distribution of the isolation quantity f_{iso} for signal electrons for different $u_{\parallel}$ ranges: $u_{\parallel} \leq -10$ GeV (Top Left), $-10 < u_{\parallel} \leq -5$ GeV (Top Right), $-5 < u_{\parallel} \leq 0$ GeV (Middle Left), $0 < u_{\parallel} \leq 5$ GeV (Middle Right), $5 < u_{\parallel} \leq 10$ GeV (Bottom Left) and $u_{\parallel} > 10$ GeV (Bottom Right).

3.99 ± 0.05 GeV. In the fast Monte Carlo simulation, we use a 2-dimensional plot $\not{E}_T^x$ versus $\not{E}_T^y$ from the minimum bias events, and for each W or Z event we just randomly pick $\not{E}_T^x$ and $\not{E}_T^y$ values from the 2-dimensional plot.

We also looked at the effect of the instantaneous luminosity on the MET distribution; Figure 7.11 shows $\not{E}_T$ for all minimum bias events versus the instantaneous luminosity, the line is a linear fit to the [0.2, 1.0] $\times$ $10^{30}\text{cm}^{-2}\text{s}^{-1}$ region and the slope is determined to be 0.6 GeV/$10^{30}\text{cm}^{-2}\text{s}^{-1}$. From Figure 7.8, it can be seen that the average luminosity for minimum bias events and W events differs by $0.1 \times 10^{30}\text{cm}^{-2}\text{s}^{-1}$. Thus on average, the luminosity reweighting will shift $\not{E}_T$ by 0.061 GeV.

As mentioned before, the underlying event contribution to the W events is not exactly the same as minimum bias events; we use the scale factor α_{mb} to describe the difference. α_{mb} is determined to be 0.95 ± 0.05 by varying α_{mb} in MC until the simulated $u_{\parallel}$ and $u_{\perp}$ distributions

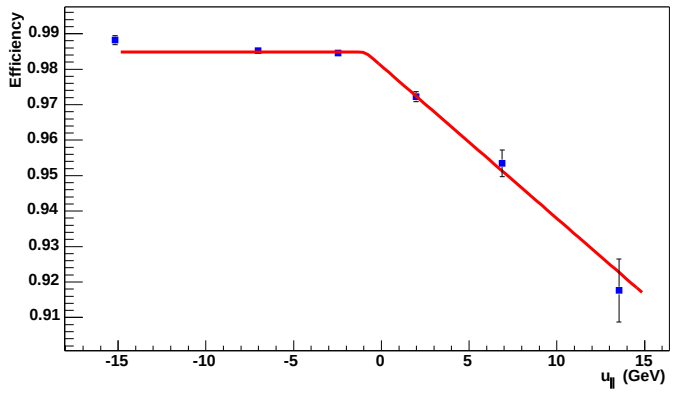

Figure 7.7: $u_{\|}$ efficiency.

agree with the data distributions.

The underlying event model and the resolution can be verified using the η-imbalance, $(\vec{p}_T^{\,ee} + \vec{p}_T^{\,rec}) \bullet \hat{\eta}$ and the ξ-imbalance, $(\vec{p}_T^{\,ee} + \vec{p}_T^{\,rec}) \bullet \hat{\xi}$ in $Z \to ee$ events. Since the magnitude of the energy vector of the underlying event is of the same order as that of the p_T of the vector boson, the widths of the distributions of η and ξ imbalances are very sensitive to the underlying event contribution. Figure 7.12 and Fig. 7.13 show the η-imbalance and ξ-imbalance from the Z data sample and the fast Monte Carlo with the parameters mentioned above; the agreement between data and Monte Carlo simulation is good.

7.5 $u_{\|}$ Correction

As mentioned above, the electron energy is measured as the energy in a window of 5×5 towers; this region is excluded from the computation of $\not{E}_T$. The size of the window is selected so that leakage of the electron shower out of the window is negligible. However, leakage of energy from the underlying event into the electron window can not be avoided; the underlying event energy in the electron window will bias the recoil measurement.

We must correct the recoil u_T for the momentum that is lost by excluding the electron window. The momentum that is lost always points in direction of the electron and therefore biases $u_{\|}$

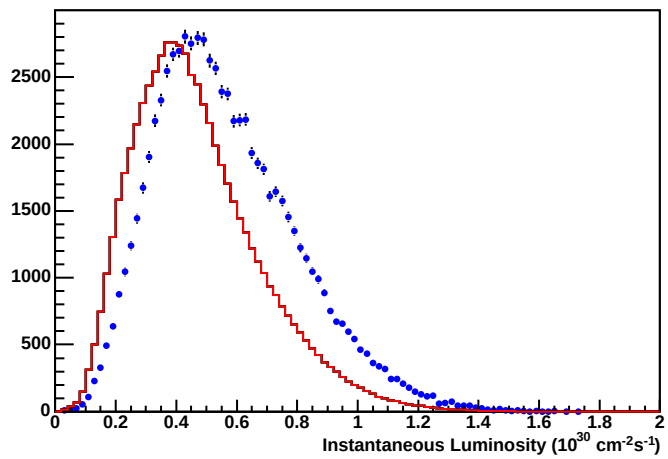

Figure 7.8: Instantaneous luminosity profiles for minimum bias events (line) and the W events (points).

towards negative values. Since for $p_T^W \ll M_W$

$$m_T \approx 2p_T(e) + u_{\parallel} \tag{7.5}$$

any $u_{\parallel}$ bias directly propagates into a bias on the transverse mass, we call this bias $\Delta u_{\parallel}$. The $u_{\parallel}$ correction is very sensitive to the ratio of W events with $u_{\parallel} > 0$ and $u_{\parallel} < 0$, and we change the $u_{\parallel}$ correction in the Monte Carlo simulation until it gives the same ratio as data. From Fig. 7.14, we determine the $u_{\parallel}$ correction to be -1.78 ± 0.01 GeV. The $u_{\parallel}$ correction depends on the instantaneous luminosity, and $u_{\parallel}$ itself. In this study, we only apply the average correction. Further studies about $u_{\parallel}$ correction are still undergoing.

7.6 Recoil System Simulation Results

The recoil system simulation is one of the most important parts of the fast Monte Carlo simulation. Figure 7.15 compares the $u_{\parallel}$ and $u_{\perp}$ spectra observed in the $W \to e\nu$ data to that predicted by the fast Monte Carlo. The mean value of $u_{\parallel}$ for the data is -2.08 GeV; there are two sources for this. The dominant effect is simply the kinematics of $W \to e\nu$ decays, the electron is preferentially emitted in the direction the W was traveling, and the second effect is due to the $u_{\parallel}$

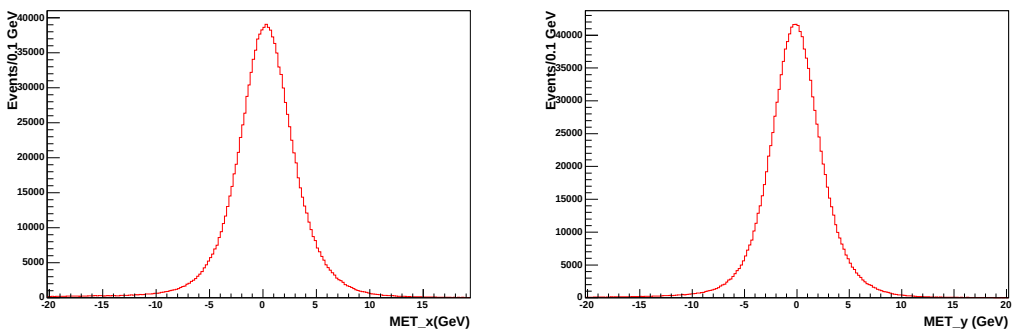

Figure 7.9: x and y Component of MET distribution from minimum bias events.

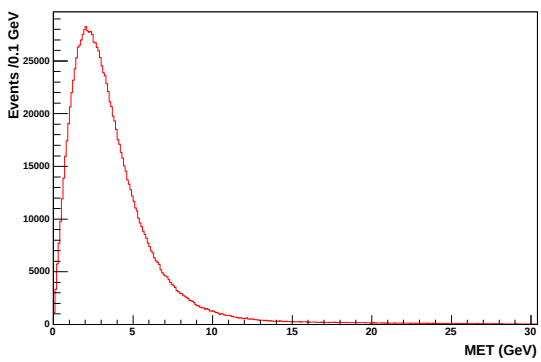

Figure 7.10: $\not\!\!E_T$ distribution from minimum bias events.

efficiency. The observed good agreement between the data and MC simulation indicates that the event kinematic and the electron identification efficiency are modeled adequately.

Figure 7.16 and 7.17 show the electron η distribution and $\Delta\phi$ between the electron and $\not\!\!E_T$ from $W \to e\nu$ decays compared to the Monte Carlo simulation. Figures 7.18 to 7.21 show the correlation between $< u_{\parallel} >$ and p_T^e, p_T^ν, M_T and p_T^W. The simulation tracks the correlation very well. Note that no p_T^W cut was used when making these distributions. An important feature of the transverse mass is that, unlike p_T^e and p_T^ν, M_T is relatively uncorrelated with $u_{\parallel}$. This shows clearly one of the advantage of using the transverse mass to obtain the W mass and W width. Figure 7.22 to Figure 7.24 show the p_T^e, p_T^ν and M_T spectra from the collider data for the sub-samples with $u_{\parallel} < 0$ and $u_{\parallel} > 0$ and the corresponding Monte Carlo predictions.

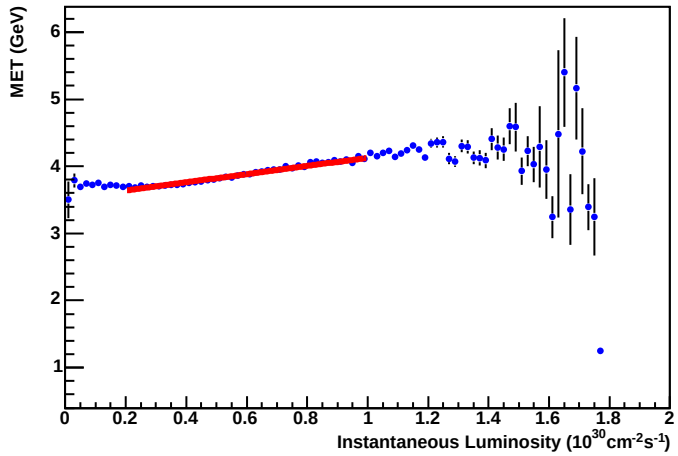

Figure 7.11: $\not\!\!E_T$ vs instantaneous luminosity for minimum bias events, the line is a fit from 0.2 to 1.0, the slope is 0.61 GeV/10^{30}cm^{-2}s^{-1} and the offset is 3.5 GeV.

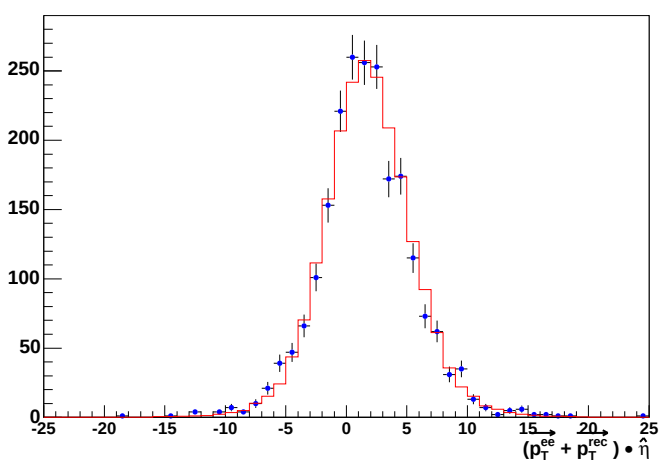

Figure 7.12: η imbalance (defined as $(\vec{p}_T^{\,ee} + \vec{p}_T^{\,rec}) \bullet \hat{\eta}$) for $Z \to ee$ events. Dots for data, line for the fast Monte Carlo simulation.

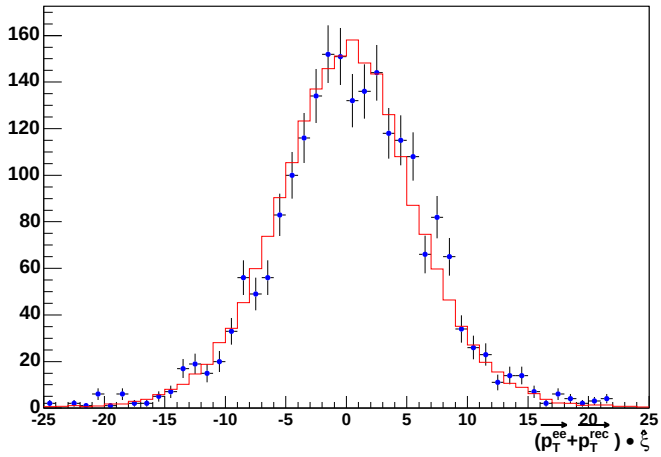

Figure 7.13: ξ imbalance (defined as $(\vec{p}_T^{\,ee} + \vec{p}_T^{\,rec}) \bullet \hat{\xi}$) for $Z \to ee$ events. Dots for data, line for the fast Monte Carlo simulation.

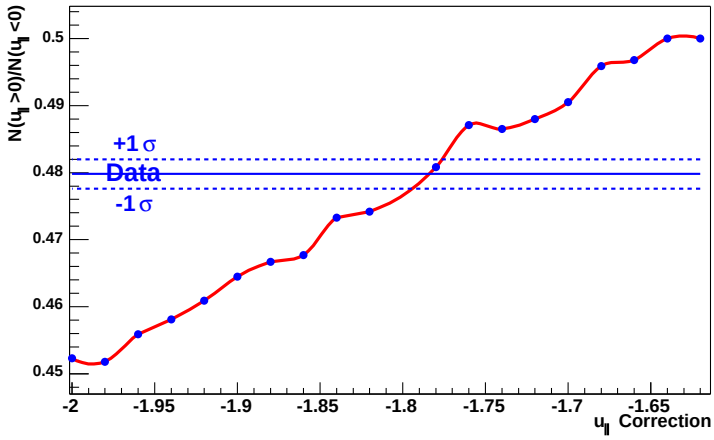

Figure 7.14: Determination of $u_\parallel$ correction $\Delta u_\parallel$. The curved line connecting the Monte Carlo points shows the correlation between $u_\parallel$ correction vs $N(u_\parallel > 0)/N(u_\parallel < 0)$ from Monte Carlo. The horizontal solid line shows the ratio $N(u_\parallel > 0)/N(u_\parallel < 0)$ measured from data and the horizontal dashed lines the uncertainty on $N(u_\parallel > 0)/N(u_\parallel < 0)$. From the intersection of the data line with the curved line we determin the $u_\parallel$ correction to be -1.78 ± 0.01 GeV.

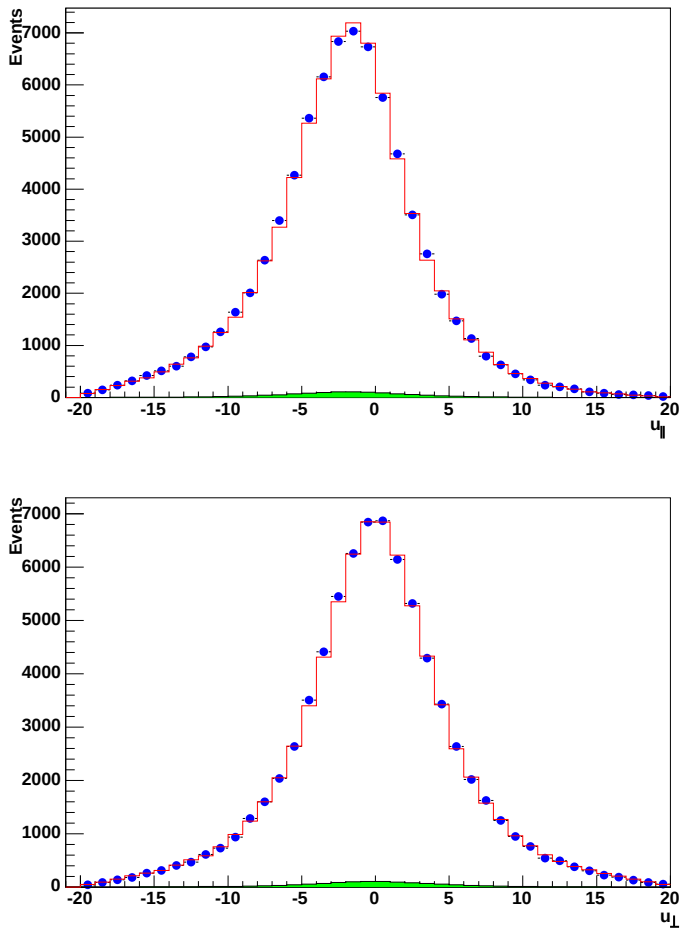

Figure 7.15: $u_{\parallel}$ (Top) and $u_{\perp}$ (Bottom) distributions for $W \to e\nu$ events (Dots for data, line for MC).

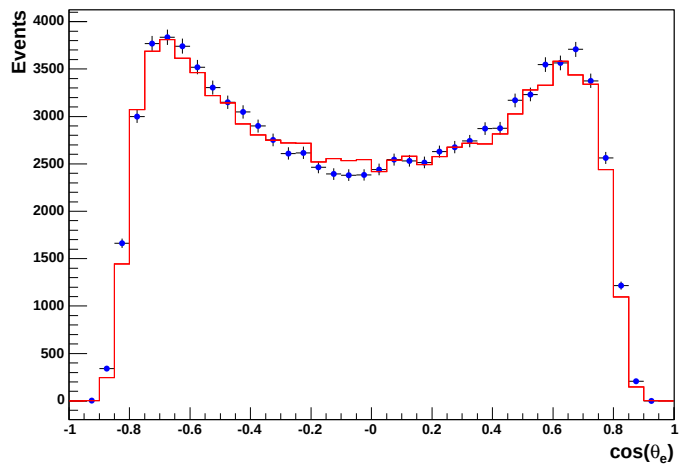

Figure 7.16: $\cos(\theta_e)$ for electrons from $W \to e\nu$ events (Dots for data, line for MC).

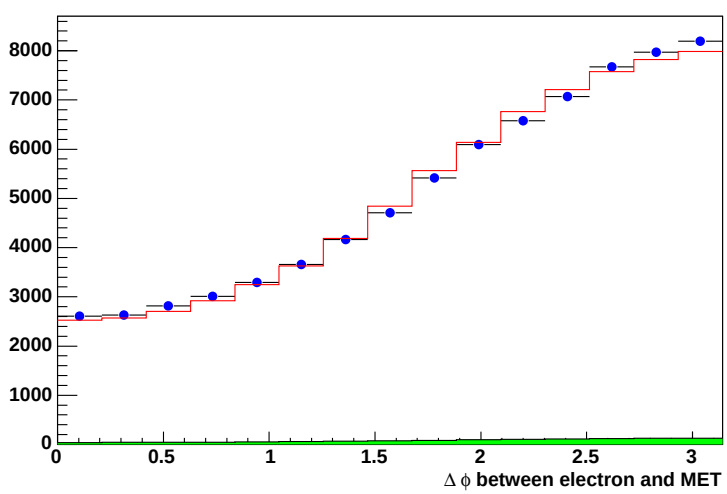

Figure 7.17: Azimuthal angle difference between electron and $\not{E}_T$ from $W \to e\nu$ decays from $W \to e\nu$ decays compared to the Monte Carlo simulation (Dots for data, line for MC, shadowed area for QCD background).

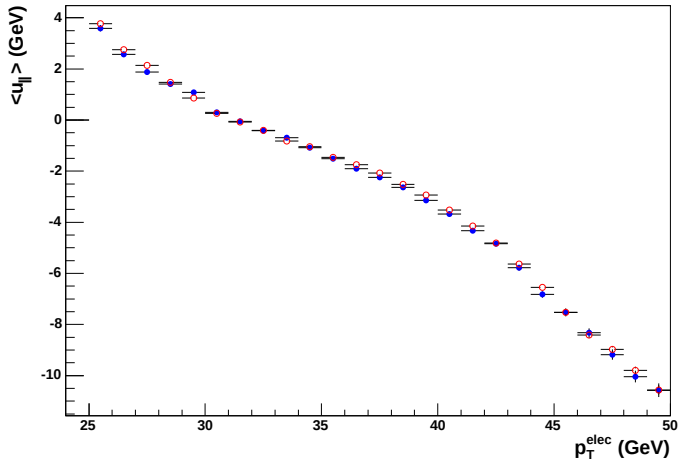

Figure 7.18: Distribution of the mean $u_{\parallel}$ versus p_T^e from $W \to e\nu$ decays compared to the Monte Carlo simulation (Dots for data, circles for MC, no p_T^W cut).

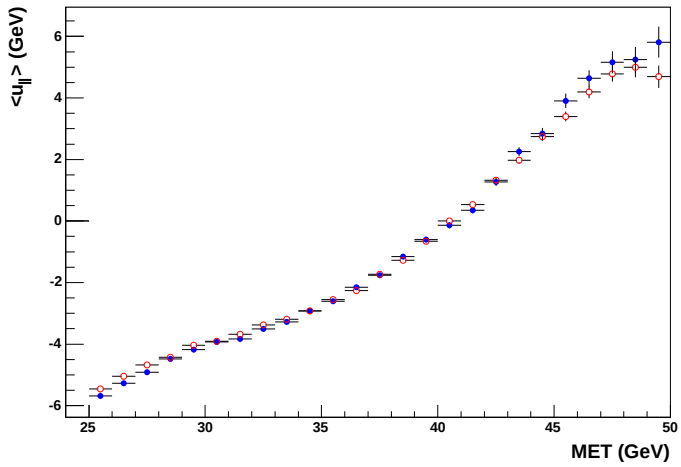

Figure 7.19: Distribution of the mean $u_{\parallel}$ versus p_T^{ν} from $W \to e\nu$ decays compared to the Monte Carlo simulation (Dots for data, circles for MC, no p_T^W cut).

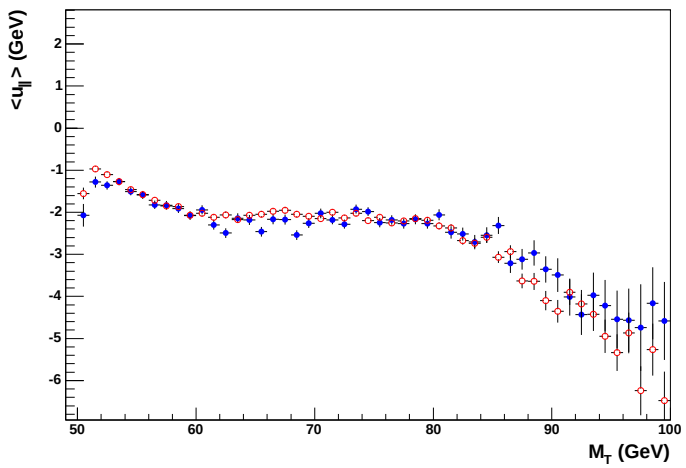

Figure 7.20: Distribution of the mean $u_{\parallel}$ versus M_T from $W \to e\nu$ decays compared to the Monte Carlo simulation (Dots for data, circles for MC, no p_T^W cut).

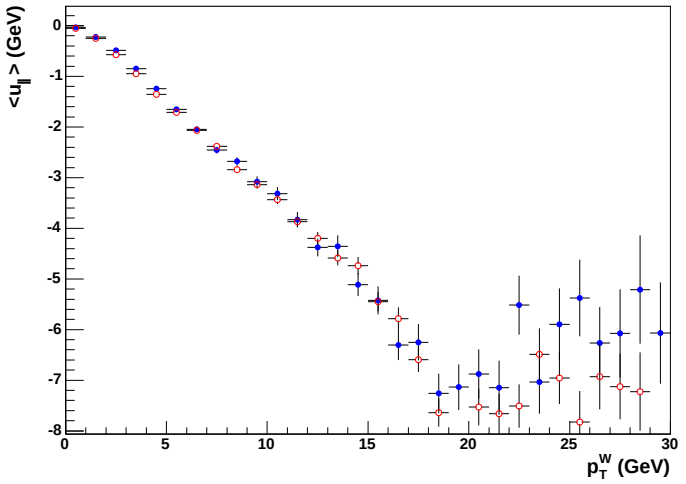

Figure 7.21: Distribution of the mean $u_{\parallel}$ versus p_T^W from $W \to e\nu$ decays compared to the Monte Carlo simulation (Dots for data, circles for MC, no p_T^W cut).

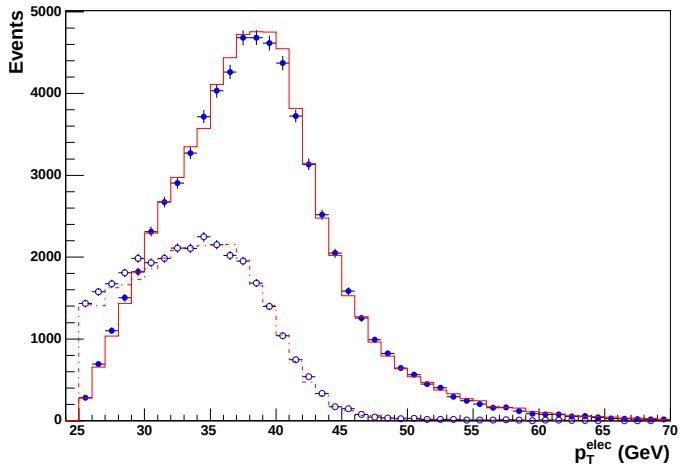

Figure 7.22: Spectrum of p_T^e from W data with $u_\parallel < 0$ (dots) and $u_\parallel > 0$ (circles) compared to the Monte Carlo simulations (Solid line for $u_\parallel < 0$ and dashed line for $u_\parallel > 0$).

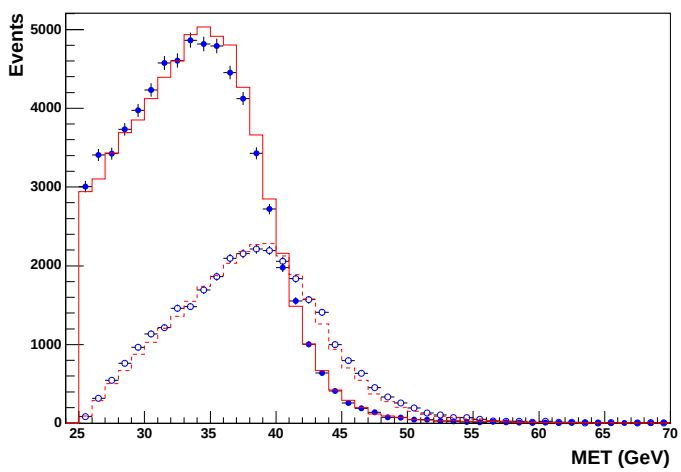

Figure 7.23: Spectrum of p_T^ν from W data with $u_\parallel < 0$ (dots) and $u_\parallel > 0$ (circles) compared to the Monte Carlo simulations (Solid line for $u_\parallel < 0$ and dashed line for $u_\parallel > 0$).

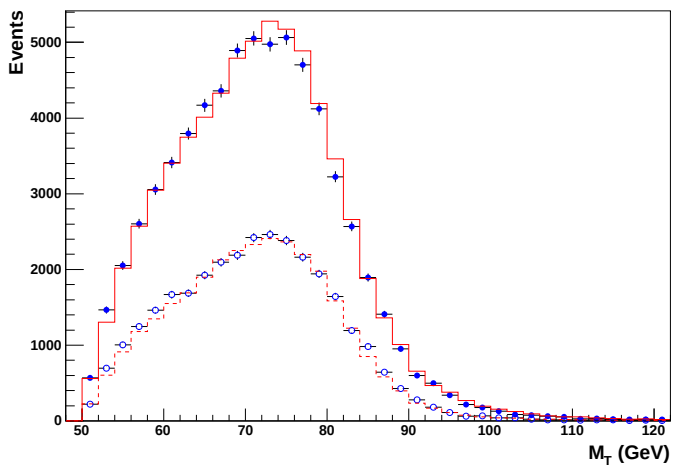

Figure 7.24: Spectrum of M_T from W data with $u_{\|} < 0$ (dots) and $u_{\|} > 0$ (circles) compared to the Monte Carlo simulations (Solid line for $u_{\|} < 0$ and dashed line for $u_{\|} > 0$).

Chapter 8

Fitting

We determine the W width by performing binned maximum likelihood fits of the transverse mass distribution in the data to Monte Carlo templates with different values of Γ_W.

8.1 Maximum Likelihood

The likelihood for a given width Γ is

$$\mathrm{L}(\Gamma) = \prod_i P_i(\Gamma) \tag{8.1}$$

where $P_i(\Gamma)$ is the probability of each event. In the case of binned data, it is the probability for each bin to have the given number of events for the width Γ. Usually, the log likelihood is used, and is given by

$$L = -ln\mathrm{L}(\Gamma) = -ln\prod_i P_i(\Gamma) = -\sum_i lnP_i(\Gamma) \tag{8.2}$$

The fitted width is that Γ_W at which L is minimum:

$$\Gamma_W = \Gamma(L = L_{minimum}) \tag{8.3}$$

The probability of x_i events in the ith bin is given by a Poisson distribution and the log-likelihood is

$$L = -\sum_i [x_i \times ln(\mu_i) - \mu_i - ln(x_i!)] \tag{8.4}$$

where the sum is over the bins in the fitting region of transverse mass distribution, and μ_i is the expected number of events in each bin $\mu_i = bkg_i + W_i$, where bkg_i is the background in the ith bin and W_i is the MC signal in the ith bin.

8.2 Reweighting

It is not possible to generate a large set of simulated events for each W-width point; however, with the help of a reweighting procedure described below, it is possible to produce a distribution

for any arbitrary value of W width Γ_W from a sample of Monte Carlo events generated at just one Γ_W^{gen}. This method is particularly valuable for small excursions from $\Gamma_W = \Gamma_W^{gen}$.

Assume $P(x|\Gamma_W)$ is the probability density for an event with an observable x in a Monte Carlo simulation that is generated with a value Γ_W for the W width. The reweighting technique is based on the fact that the difference between MC simulations that correspond to different W width is given by the probability $P(x|\Gamma_W)$. We can define a weight function:

$$w(x, \Gamma_W^{gen}, \Gamma_W^{reweight}) = \frac{P(x|\Gamma_W^{reweight})}{P(x|\Gamma_W^{gen})} \tag{8.5}$$

which can be used to obtain a distribution that corresponds to a W width $\Gamma_W^{reweight}$, by taking events generated with Γ_W^{gen} and multiplying each by this weight. Since for W production, we use a relativistic Breit-Wigner with a fixed width:

$$BW(m_W, M_W, \Gamma_W) \propto \frac{(m_W \Gamma_W / M_W)^2}{(m_W^2 - M_W^2)^2 + (m_W^2 \Gamma_W / M_W)^2} \tag{8.6}$$

Assuming

$$P(x|\Gamma_W) \propto BW(m_W, M_W, \Gamma_W) \tag{8.7}$$

we have the weight factor

$$w(x, \Gamma_W^{gen}, \Gamma_W^{reweight}) = \left(\frac{\Gamma_W^{reweight}}{\Gamma_W^{gen}}\right)^2 \times \frac{M_W^2(m_W^2 - M_W^2)^2 + (m_W^2 \Gamma_W^{gen})^2}{M_W^2(m_W^2 - M_W^2)^2 + (m_W^2 \Gamma_W^{reweight})^2} \tag{8.8}$$

8.3 Fitting

Monte Carlo templates are prepared of the W boson transverse mass using the detector parameters described in Sections 6 and 7. About 10 million $W \to e\nu$ events are generated with PYTHIA and using CTEQ6 as the central PDF set [73]. The default W mass is 80.45 GeV and the default W width is 2.071 GeV. Families of templates are made for W boson widths varied in 50 MeV steps between 1.6 GeV to 3.6 GeV using the reweighting method described above. The templates are normalized to the number of real W events in data in the region $50 < M_T < 100$ GeV, with bins of 2 GeV. The background distributions of QCD and $W \to \tau\nu$ events are added to the templates, and a binned maximum likelihood is calculated for the data. The fitting region

is chosen to be 100 GeV $< M_T <$ 200 GeV to minimize the total systematic uncertainty. From the dependence of the likelihood on Γ_W (Figure 8.1), we obtain the W boson width and its error as $\Gamma_W = 2.011 \pm 0.093$ GeV by fitting it with a fourth order polynomial function. The top plot of Fig. 8.2 shows the data and MC comparison plot with the best W width for M_T.

As a goodness-of-fit test, we compute $\chi 2 = \sum_{i=1}^{N}(y_i - P_i)^2/P_i$ for the whole region [50, 200] GeV, where the sum runs over all 75 bins for this region, y_i is the observed number of events in bin i, and P_i is the expected number of events from MC in bin i. We have a $\chi^2/d.o.f$ of 122.6/75 for the whole region, the bottom plot of Fig. 8.2 shows the contribution of $\chi_i = (y_i - P_i)/\sqrt{P_i}$ for the whole transverse mass region.

The top plots of Fig. 8.3, 8.4 and 8.5 show the data and MC comparison plots for electron p_T, $\not{E}_T$ and p_T^W with the best W width. The bottom plots of Fig. 8.3, 8.4 and 8.5 show the χ contribution from each bin. The $\chi^2/d.o.f$ are 83.1/75, 82.5/75 and 18.9/20 for electron p_T, $\not{E}_T$ and p_T^W distributions in the whole range. Figure 8.6 shows the data-MC comparison plots for M_T in [100, 200] GeV, electron p_T and $\not{E}_T$ in [50, 100] GeV.

8.4 Systematic Uncertainties

The systematic uncertainties in the determination of W width are due to effects that could alter the transverse mass distribution. Basically, every input parameter in the MC could cause errors in the final result. These parameters are in most cases constrained by the $Z \to ee$ data; since there is only a finite Z sample, there is an error associated with each part of the detector model. Although these errors are considered as systematic errors for the width measurement, they are really statistical errors which depend on the number of Z events.

To estimate the effects, we allow these input parameters to vary by one standard deviation and then re-generate the transverse mass spectrum. The procedure is the same as was done to determine the mean value of W width. If the variation of the W boson width with respect to a parameter is not symmetric, the error is symmetrized by assigning to it the larger of the two values. Additional uncertainties arise from uncertainties in the value of the W mass (constrained

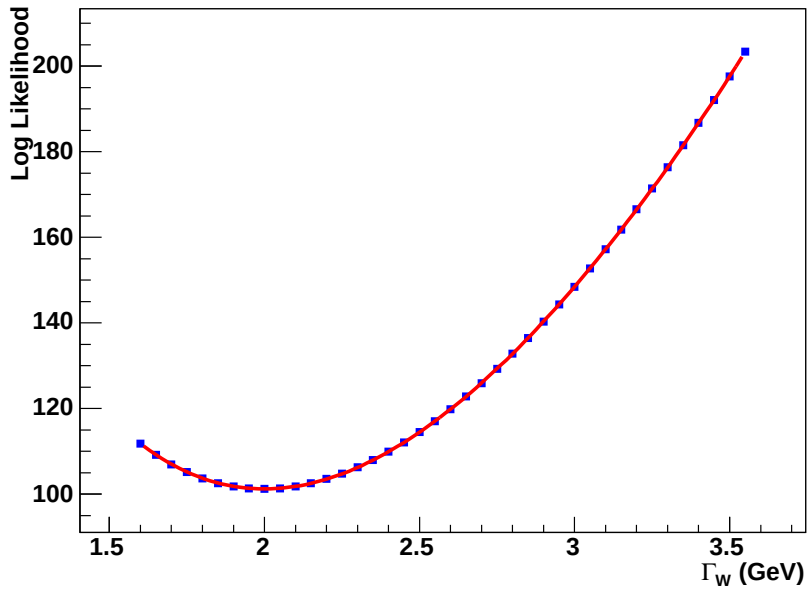

Figure 8.1: Results of the maximum likelihood fit of the data to Monte Carlo templates. Monte Carlo templates are generated with Γ_W between 1.6 and 3.6 GeV at 50 MeV intervals. Each point represents a log-likelihood fit performed over the range $100 < M_T < 200$ GeV. The curve is the best fit of the likelihood points to a fourth order polynomial. The best value is 2.011 ± 0.093 GeV.

to its world average) and from uncertainties in the production model and the parton distribution. Pending further investigation these uncertainties are taken from our previous measurement [30]. Table 8.1 lists the uncertainties in the measured W width caused by each individual source for the fitting region $100 < M_T < 200$ GeV region, and Table 8.2 shows the uncertainties for the other two fitting regions $90 < M_T < 200$ GeV and $110 < M_T < 200$ GeV.

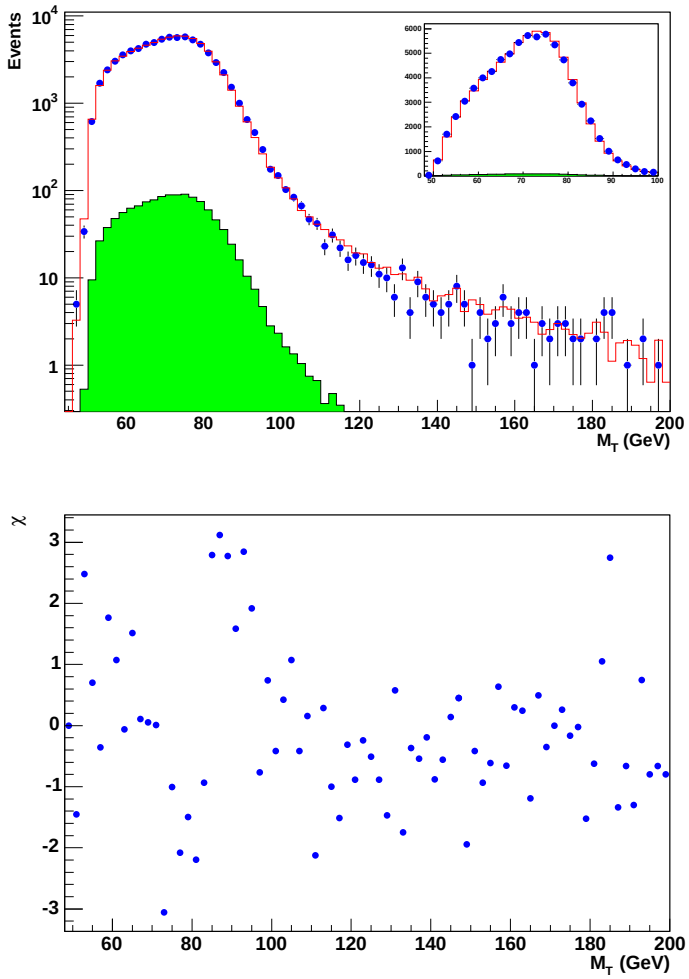

Figure 8.2: Top: Comparison of data to Monte Carlo templates for the transverse mass shape. The dots with error bars are data, the shadowed area is QCD background and the line corresponds to QCD + MC $W \to e\nu$ + MC $W \to \tau\nu$ with the best W width. Bottom: χ distribution for the fit to the M_T spectrum.

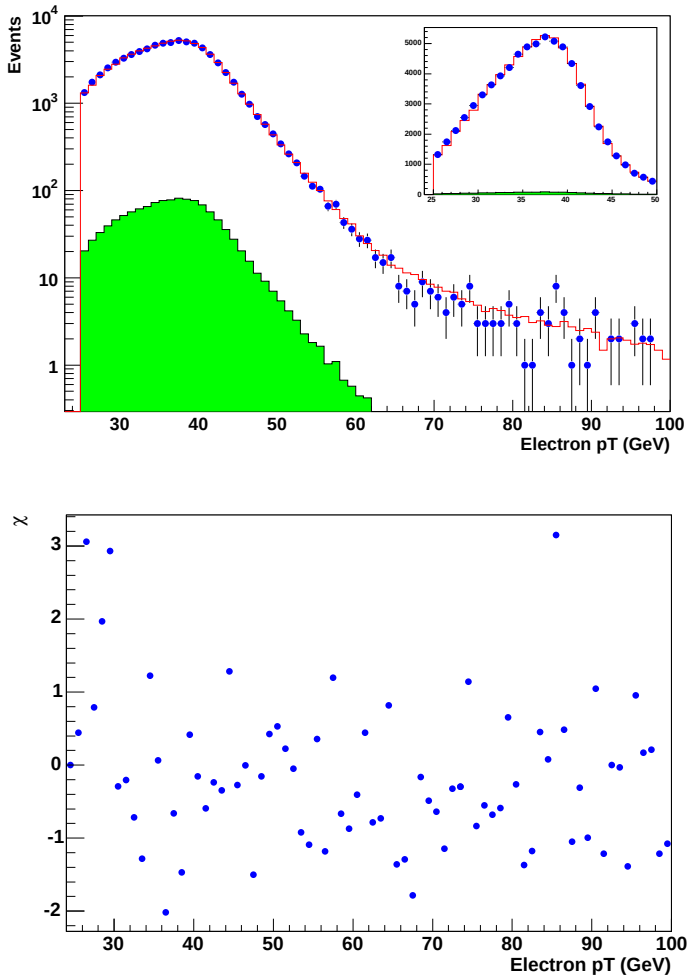

Figure 8.3: Top: Comparison of data to Monte Carlo templates for electron p_T spectrum. The dots with error bars are data, the shadowed area is QCD background and the line corresponds to QCD + MC $W \to e\nu$ + MC $W \to \tau\nu$ with the best W width. Bottom: χ distribution for the fit to the electron p_T spectrum.

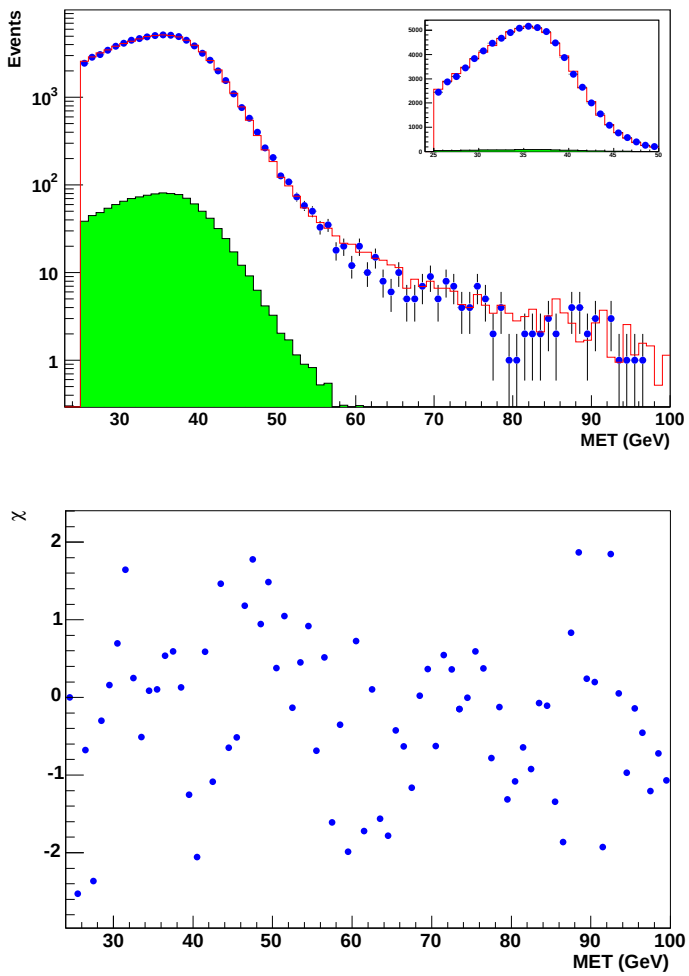

Figure 8.4: Top: Comparison of data to Monte Carlo templates for $\not\!\!E_T$ spectrum. The dots with error bars are data, the shadowed area is QCD background and the line corresponds to QCD + MC $W \to e\nu$ + MC $W \to \tau\nu$ with the best W width. Bottom: χ distribution for the fit to the $\not\!\!E_T$ spectrum.

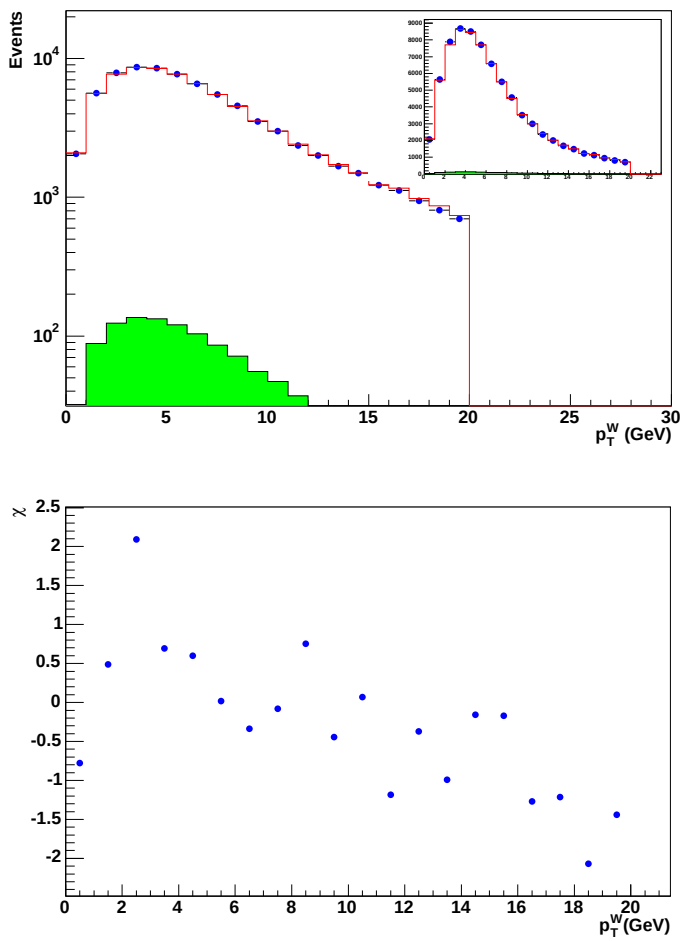

Figure 8.5: Top: Comparison of data to Monte Carlo templates for p_T^W spectrum. The dots with error bars are data, the shadowed area is QCD background and the line corresponds to QCD + MC $W \to e\nu$ + MC $W \to \tau\nu$ with the best W width. Bottom: χ distribution for the fit to the W p_T spectrum.

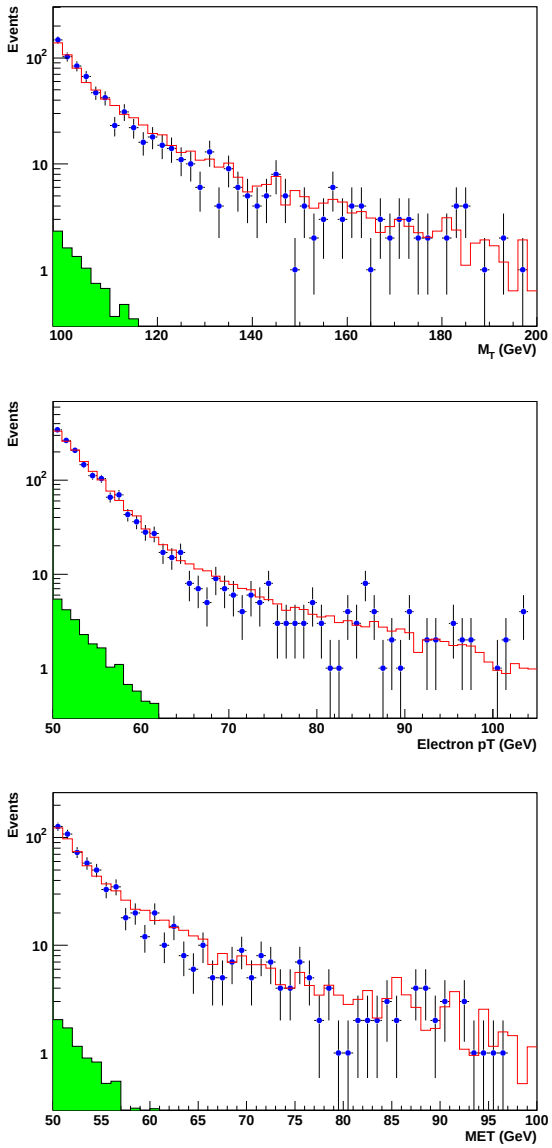

Figure 8.6: Data-MC comparison plots for M_T in [100, 200] GeV, electron p_T and $\not{E}_T$ in [50, 100] GeV.

Parameter	Value	$\Delta\Gamma_W$ (MeV)
EM Energy Scale	1.0054 ± 0.0010	15
EM Energy Offset	(0.038 ± 0.048) GeV	17
EM Energy Resolution, Sampling	(0.15 ± 0.03) GeV$^{1/2}$	30
EM Energy Resolution, Constant	$(4.20 \pm 0.23)\%$	41
HAD Momentum Response	0.67 ± 0.02	40
HAD Energy Resolution, sampling	(0.80 ± 0.20) GeV$^{1/2}$	50
HAD Energy Resolution, constant	0.05 ± 0.01	7
Primary Vertex	(25.00 ± 0.15)cm	10
Calorimeter Position Resolution $\sigma_{\eta^{det}}$	0.007 ± 0.007	5
Calorimeter Position Resolution $\sigma_{\phi^{det}}$	(0.007 ± 0.007) rad	5
Underlying Event	–	47
$u_{\parallel}$ Correction ($\Delta u_{\parallel}$)	(1.78 ± 0.01) GeV	4
$u_{\parallel}$ Efficiency s	0.0044 ± 0.0006	1
$u_{\parallel}$ Efficiency u_0	0.908 ± 0.599	1
Selection Bias	–	10
QCD Backgrounds	–	3
$Z \to ee$ and $W \to \tau\nu$ Backgrounds	–	negligible
p_T^W	–	29
M_W	–	15
PDF	–	27
Radiative Decays $\Delta R(e\gamma)$	0.20 ± 0.10	3
Systematic Uncertainty	–	107
Statistical Uncertainty	–	93
Total Uncertainty	–	142

Table 8.1: Uncertainties on the W Width Measurement for the fitting region $100 < M_T < 200$ GeV.

Parameter	Value	$\Delta\Gamma_W$ (MeV) M_T in $[90, 200]$ GeV	$\Delta\Gamma_W$ (MeV) M_T in $[110, 200]$ GeV
EM Energy Scale	1.0054 ± 0.0010	23	15
EM Energy Offset	(0.038 ± 0.048) GeV	19	16
EM Energy Resolution, Sampling	(0.15 ± 0.03) GeV$^{1/2}$	37	23
EM Energy Resolution, Constant	$(4.20 \pm 0.23)\%$	45	37
HAD Momentum Response	0.67 ± 0.02	51	6
HAD Energy Resolution, sampling	(0.80 ± 0.20) GeV$^{1/2}$	52	24
HAD Energy Resolution, constant	0.05 ± 0.01	3	5
Primary Vertex	(25.00 ± 0.15)cm	12	6
Calorimeter Position Resolution $\sigma_{\eta^{det}}$	0.007 ± 0.007	6	11
Calorimeter Position Resolution $\sigma_{\phi^{det}}$	(0.007 ± 0.007) rad	6	11
Underlying Event	–	47	47
$u_{\parallel}$ Correction ($\Delta u_{\parallel}$)	(1.78 ± 0.01) GeV	6	6
$u_{\parallel}$ Efficiency s	0.0044 ± 0.0006	1	2
$u_{\parallel}$ Efficiency u_0	0.908 ± 0.599	1	1
Selection Bias	–	18	10
QCD Backgrounds	–	3	4
$Z \to ee$ and $W \to \tau\nu$ Backgrounds	–	negligible	negligible
p_T^W	–	29	29
M_W	–	15	15
PDF	–	27	27
Radiative Decays $\Delta R(e\gamma)$	0.20 ± 0.10	9	8
Systematic Uncertainty	–	119	87
Statistical Uncertainty	–	79	116
Total Uncertainty	–	143	145

Table 8.2: Uncertainties on the W Width Measurement for the two fitting regions $90 < M_T < 200$ GeV and $110 < M_T < 200$ GeV.

Chapter 9

Consistency Checks

To verify the stability of the W boson width result, consistency checks have been performed in which the W boson width is determined from various modified data samples. These samples include those in which the fitting range was varied, the p_T^W cut was changed, and different fitting functions were used.

9.1 Ratio Fit

This method consists of measuring the fraction of events in a transverse mass window which a Monte Carlo study indicates good sensitivity to the width. The M_T window has been chosen to be from 100 to 200 GeV; the ratio is defined as the number of events in the window over the number of events in the total M_T range (50 to 200 GeV). Figure 9.1 shows the results of the ratio fit of the data to Monte Carlo templates of different W widths. This ratio fit gives a value 2.004 ± 0.091 GeV.

9.2 Electron p_T and $\not\!\!E_T$ Spectra

Figure 9.2 and Fig. 9.3 show data and MC comparisons for electron p_T and $\not\!\!E_T$ distributions for events with M_T between 100 and 200 GeV; good agreement is observed.

9.3 Dependence on Fitting Region

We can use different parts of the transverse mass spectrum for the likelihood fitting. We expect different fitting regions will give different results, but these results should be consistent with each other. Since the decay width is sensitive to the high tail region, we expect that fitting only the high-end region will have a smaller systematic error. However, a smaller fitting region includes

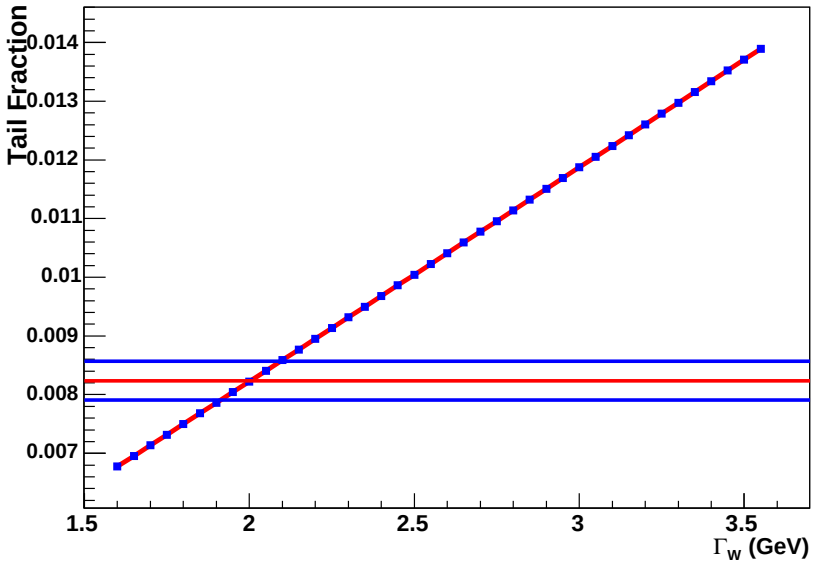

Figure 9.1: The ratio checking. The dots are the ratio from MC for different W widths, the center horizontal line represents the ratio from data. The two horizontal lines are for uncertainties. The intercept of two curves give the value 2.004 ± 0.091 GeV.

less events, which results in a larger statistical uncertainty. For the central value, we fit the transverse mass region from 100 GeV to 200 GeV. If we change the fitting region to [90, 200] GeV and [110, 200] GeV, the maximum change of Γ_W is 0.061 GeV.

9.4 Dependence on p_T^W Cut

We change the cuts on p_T^W (also known as the recoil momentum u_T) and study how well the Monte Carlo simulation reproduces the variations in the spectra. We split the W sample into four subsamples with $p_T^W < 5$ GeV, $5 < p_T^W < 10$ GeV, $10 < p_T^W < 15$ GeV and $15 < p_T^W < 20$ GeV. Then we determine the W width using the maximum likelihood method described above, and the results are 1.732 ± 0.137 for $p_T^W < 5$ GeV, 2.209 ± 0.161 GeV for $5 < p_T^W < 10$ GeV, 2.228 ± 0.271 GeV for $10 < p_T^W < 15$ GeV and 2.145 ± 0.455 GeV for $15 < p_T^W < 20$ GeV. Figures 9.4 to 9.5 show the M_T spectra from the collider data and Monte Carlo simulation for the above

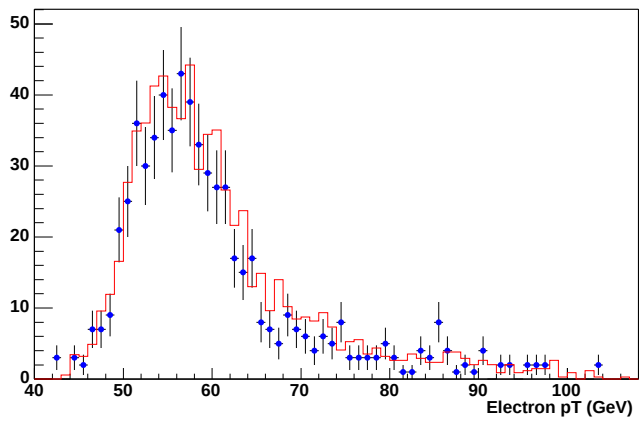

Figure 9.2: Electron p_T distribution for events with $100 < M_T < 200$ GeV (Dots for data, line for the Monte Carlo simulation. For data, the electron is required to have a matched track, and no background subtraction is applied).

four subsamples. Although there is significant variation among the shapes of the spectra for different p_T^W cuts, the Monte Carlo simulation models them well.

To study the dependence on p_T^W, we change the p_T^W both in data and MC. For $p_T^W < 18$ GeV, Γ_W derived from the likelihood method changes by 27 MeV; for $p_T^W < 23$ GeV, Γ_W changes by 7 MeV.

9.5 Dependence on Fitting Function

To get the final W width, we use a fourth order polynomial function to fit the likelihood vs Γ_W histogram. As a cross check, we also fit it with a third order polynomial and the width changes by 4 MeV; if we fit it with a fifth order polynomial, the width changes by 1 MeV.

9.6 Dependence on Instantaneous Luminosity

Figure 9.6 shows the instantaneous luminosity profile of the colliding beams during the W and Z data collection. To check the dependence of the W width on luminosity, we divide the W and Z data samples into four luminosity bins $L \leq 0.4 \times 10^{30}$ cm^{-2}s^{-1}, $0.4 < L \leq 0.6 \times 10^{30}$ cm^{-2}s^{-1},

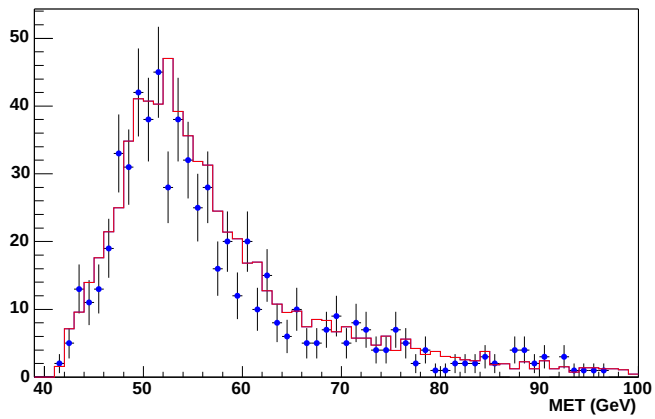

Figure 9.3: $\not\!\!E_T$ distribution for events with $100 < M_T < 200$ GeV (Dots for data, blue line for the Monte Carlo simulation. For data, the electron is required to have a matched track, and no background subtraction is applied).

$0.6 < L \leq 0.8 \times 10^{30}$ cm^{-2}s^{-1} and $L \geq 0.8 \times 10^{30}$ cm^{-2}s^{-1}. Then we determine the W width for each luminosity bin. The M_T data-MC comparison plots for each luminosity bin are shown from Fig. 9.7 to Fig. 9.8, and the variation of the fitted W width as a function of the instantaneous luminosity is shown in Fig. 9.9. Since we use $Z \to ee$ events to do the electron energy calibration, any dependence of the Z peak position and width on the luminosity will bias our results. We also divide the $Z \to ee$ candidates into four luminosity bins and fit the invariant mass distribution with a Breit-Wigner convoluted with a Gaussian distribution. Figure 9.10 and 9.11 show the Z peak position and the width of the Gaussian as a function of the instantaneous luminosity.

9.7 Dependence on Calorimeter non-linearity

The average E_T for Z decay electrons is about 43.0 GeV while the average E_T for W decay electrons is about 37.6 GeV, so the average E_T for electrons from Z decays is 5.4 GeV higher than those from W decay (See Fig. 9.12 (Top)). Since the energy calibration is done with the Z's, any non-linearity in the energy response would translate to an incorrect energy scale at the W. Assuming the p_T measurement is linear over the E_T range of W and Z events, we can use

the E/p lineshape to determine the calorimeter non-linearity. The non-linearity over a small range of E_T can be expressed as

$$\frac{\Delta\alpha}{\alpha} = \xi \times \Delta E_T \tag{9.1}$$

where the slope ξ is the calorimeter non-linearity parameter. The near equality of E/p for the W and Z samples indicates that the calorimeter non-linearity is very small (See Fig. 9.12 (Bottom)). Since the electron energy response is assumed to be linear in the Monte Carlo simulation, the difference between the energy responses with respect to electron transverse energy in the data and simulation reflects the calorimeter non-linearity. Figure 9.13 shows the strong dependence of $< E/p >$ on electron E_T both in the data and simulation, where the mean has been taken over the interval $0.9 < E/p < 1.2$ (See Appendix for E/p studies). The residuals, obtained by subtracting the MC from the data, are also shown fit to a line. The slope of the residuals is the calorimeter non-linearity, determined to be 2.882×10^{-4} GeV^{-1}. This correction is not applied to the Z data since the energy scale is derived from the Z data. However, the correction is applied to the W data and the uncertainty due to the non-linearity of the calorimeter is less than 1 MeV, and is thus negligible compared to other systematic errors.

9.8 Dependence on Calorimeter non-uniformity

For the central EM calorimeter, we have 32 modules and the variation of the energy scale between different modules will change the transverse mass shape. We divide the azimuthal direction of the electron $\phi(e)$ into 32 bins corresponding to the 32 azimuthal modules. Figure 9.14 shows the fitted W width values versus ϕ module. Also shown in Fig. 9.15 is the energy scale determined from the electron p_T spectrum from $W \to e\nu$ events versus ϕ module. Figure 9.16 shows M_T data-MC comparison for one typical module (Module 18).

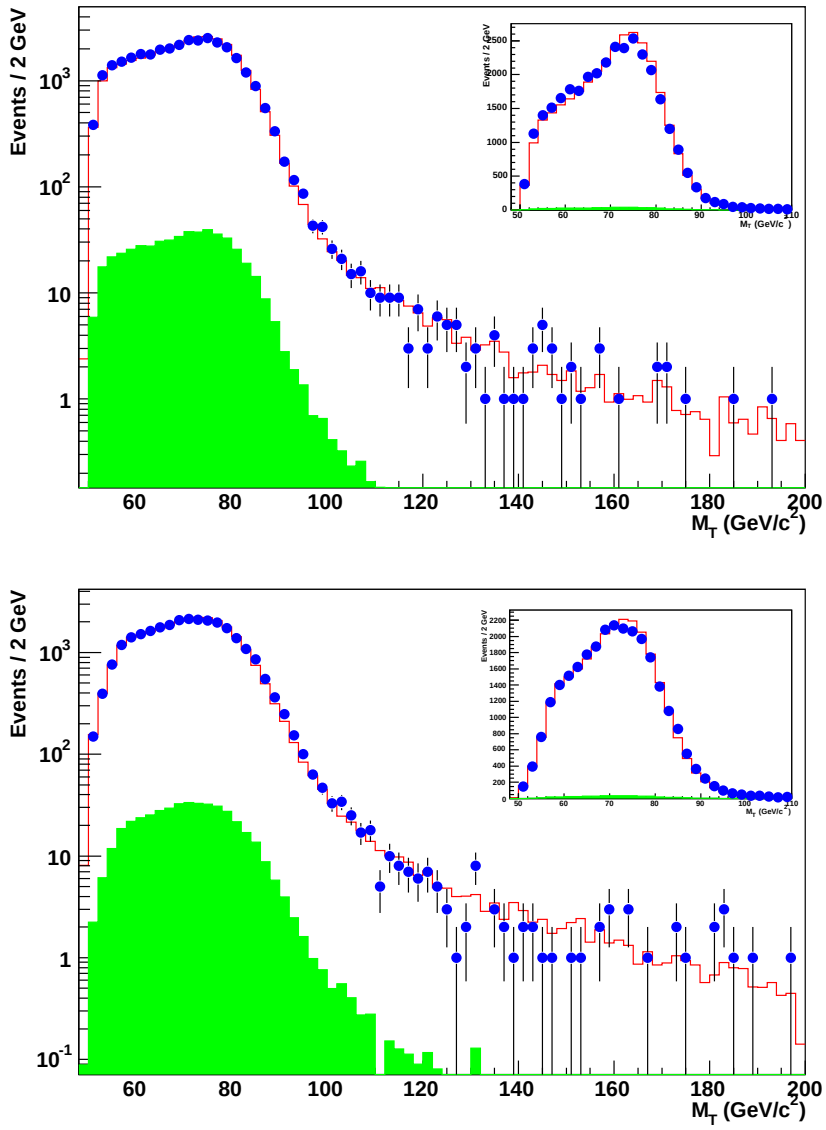

Figure 9.4: Comparison of the M_T spectra between the data (point) and the Monte Carlo simulation (solid line) for data selected with $p_T^W < 5$ GeV (Top) and $5 < p_T^W < 10$ GeV (Bottom).

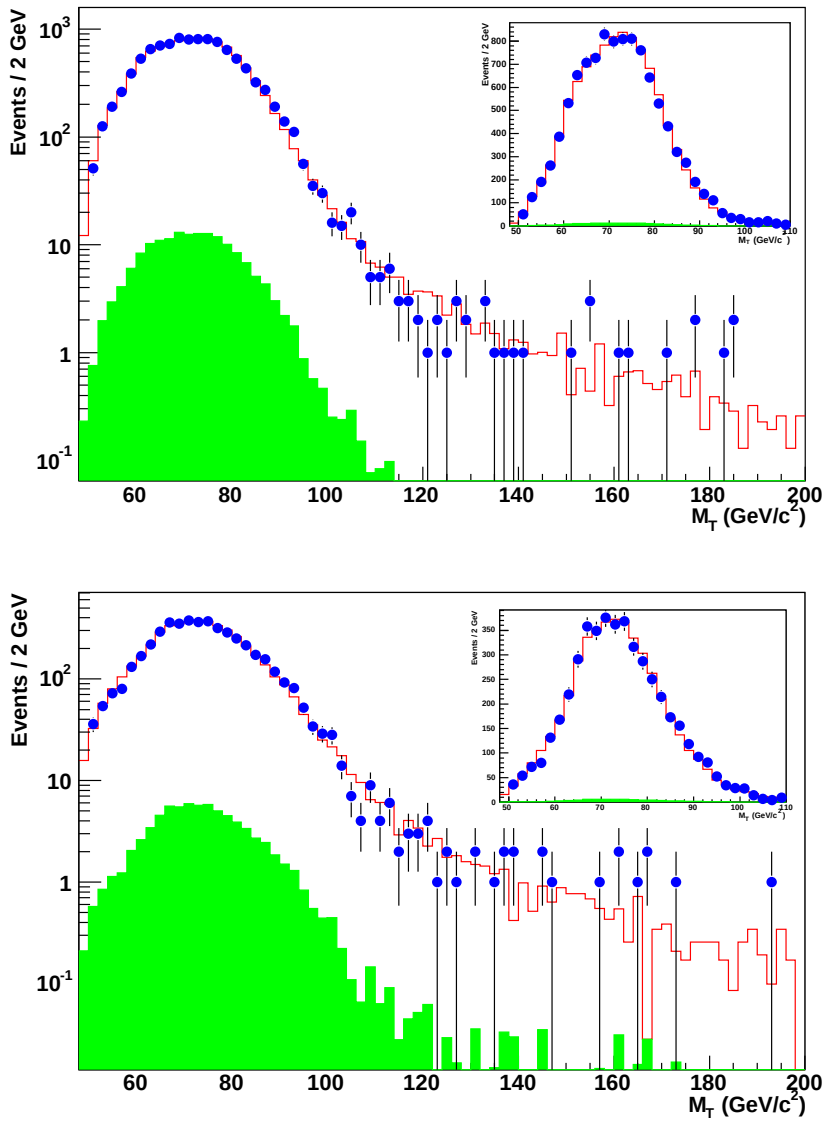

Figure 9.5: Comparison of the M_T spectra between the data (point) and the Monte Carlo simulation (solid line) for data selected with $10 < p_T^W < 15$ GeV (Top) and $15 < p_T^W < 20$ GeV (Bottom).

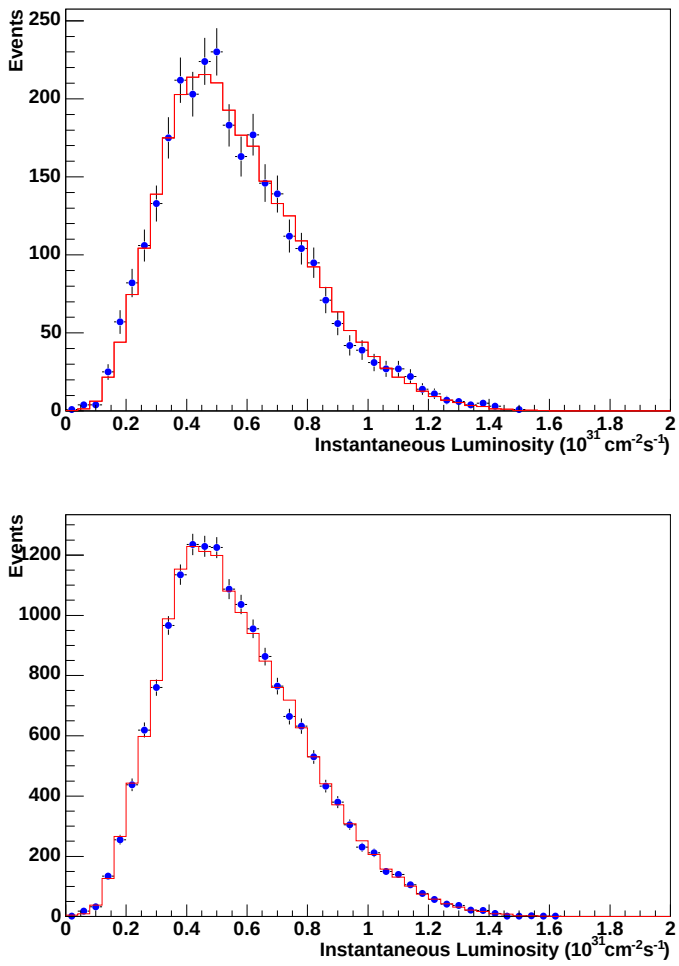

Figure 9.6: Instantaneous Luminosity distribution of the W (solid line) and the Z (blue points) samples for events where electrons with (Top) and without (Bottom) track matching requirement.

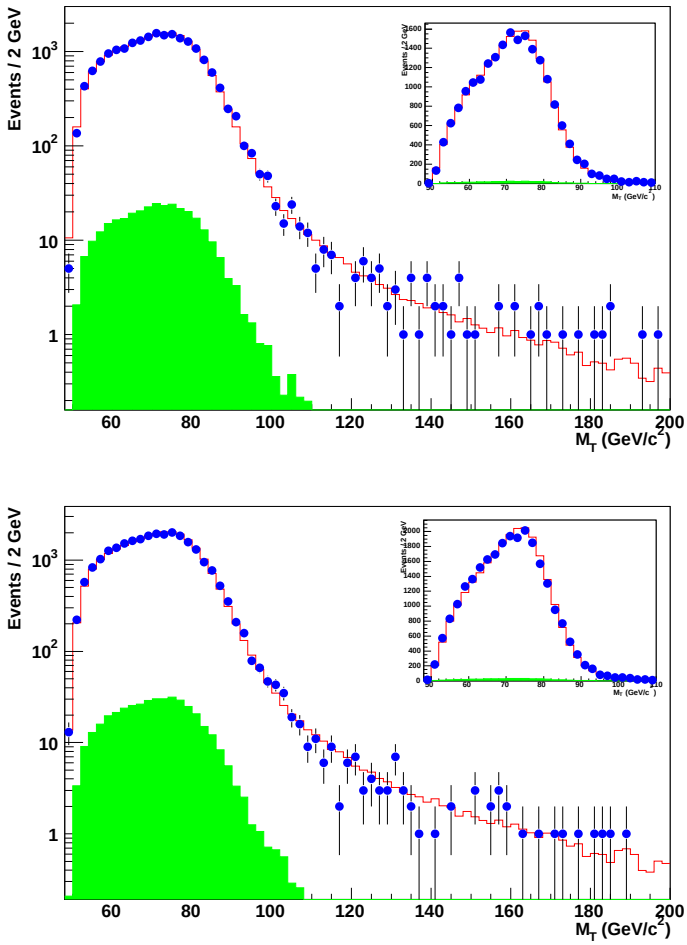

Figure 9.7: M_T data-MC comparisons for events with instantaneous luminosity $L \leq 0.4 \times 10^{30}$ cm^{-2}s^{-1} (Top) and $0.4 < L \leq 0.6 \times 10^{30}$ cm^{-2}s^{-1} (Bottom).

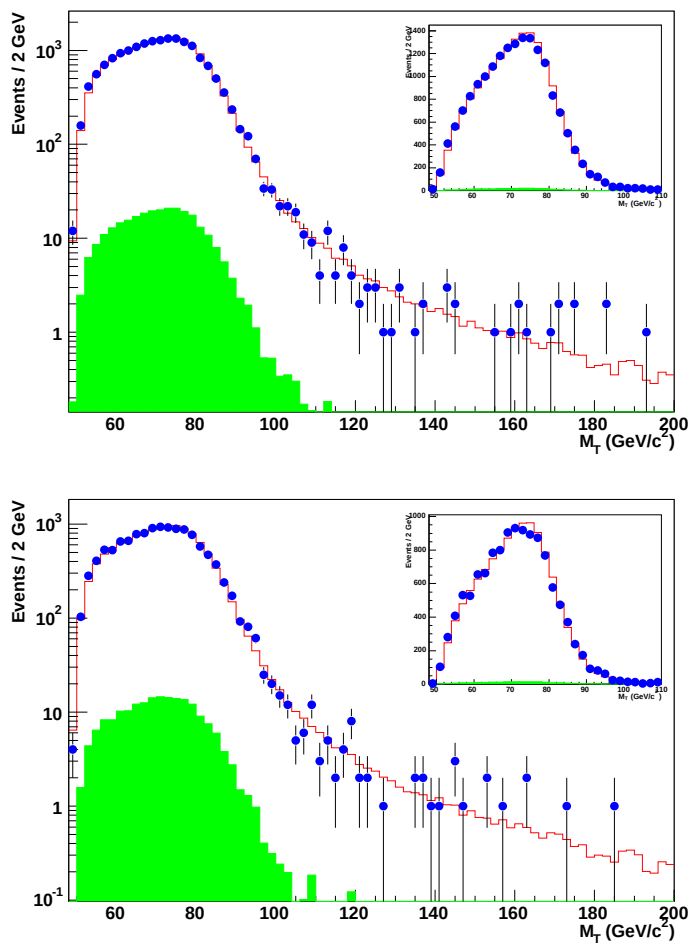

Figure 9.8: M_T data-MC comparisons for events with instantaneous luminosity $0.6 < L \leq 0.8 \times 10^{30}$ cm^{-2}s^{-1} (Top) and $L \geq 0.8 \times 10^{30}$ cm^{-2}s^{-1} (Bottom).

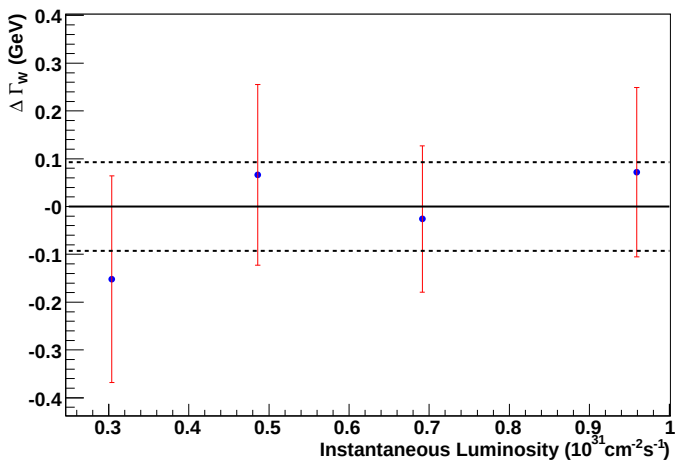

Figure 9.9: Variation in the fitted W width as a function of the instantaneous luminosity.

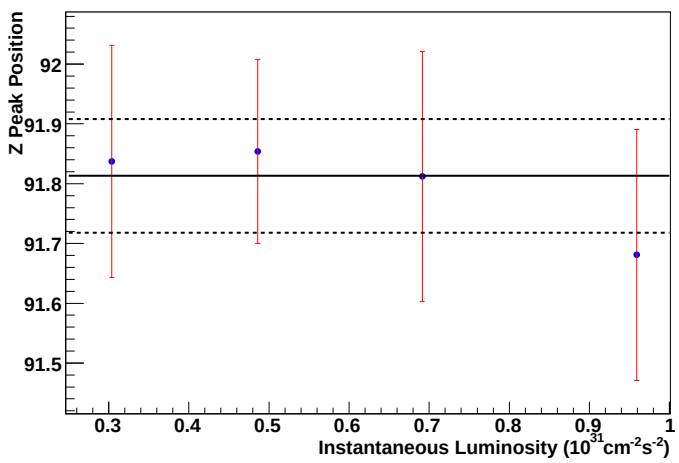

Figure 9.10: The peak position of the $Z \to ee$ invariant mass distribution vs instantaneous luminosity.

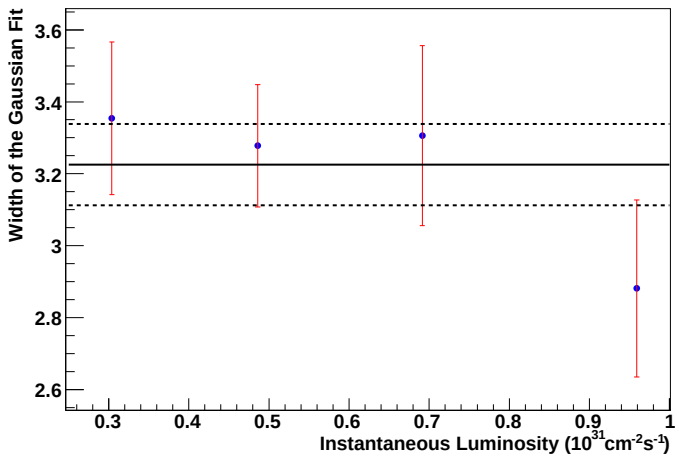

Figure 9.11: The width of the fitted Gaussian for the $Z \rightarrow ee$ invariant mass distribution vs instantaneous luminosity.

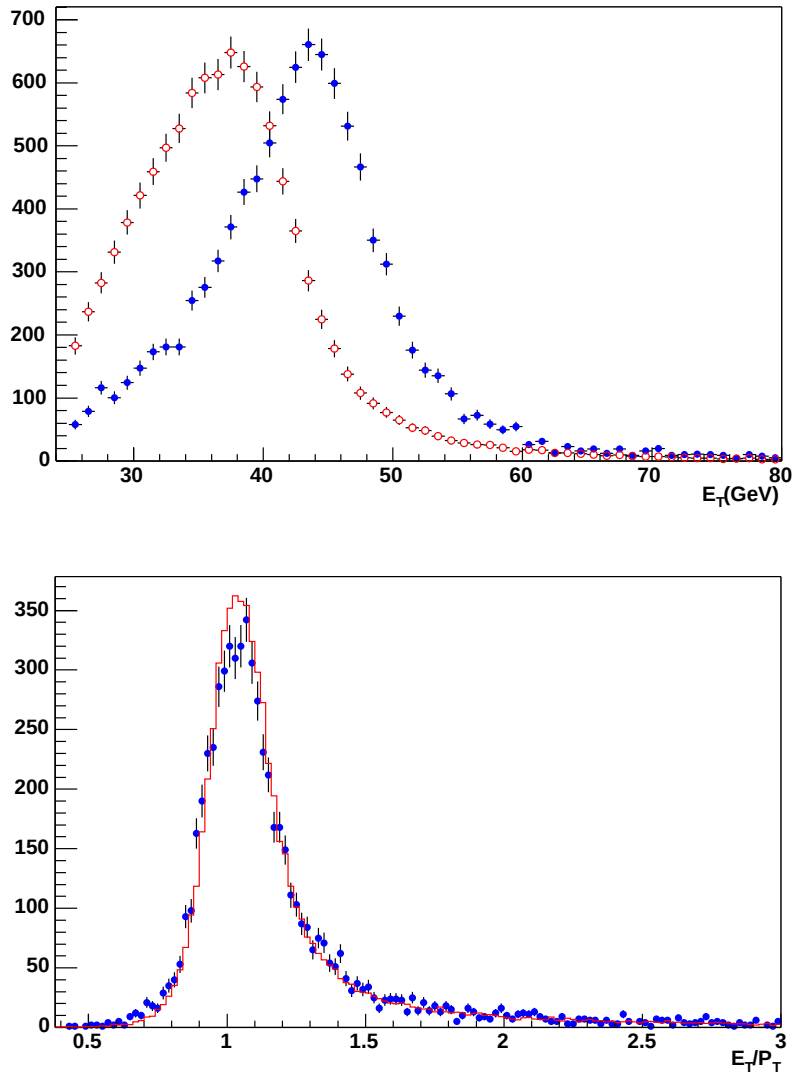

Figure 9.12: Top: The E_T distributions of electrons from W and Z decays (Blue dots for Z electrons and red circles for W electrons). Bottom: The E/P distributions of electrons from W and Z decays (Blue dots for Z electrons and red line for W electrons).

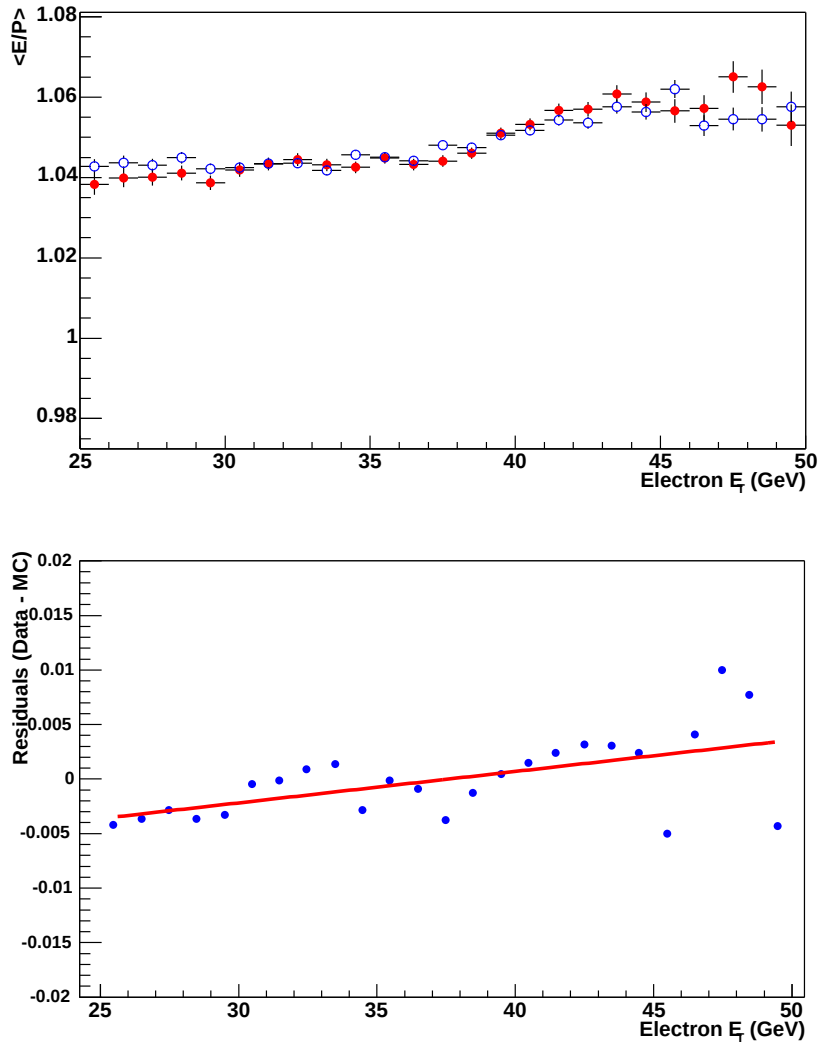

Figure 9.13: Top: Variation of the mean of E/P with electron transverse energy in the data and the Monte Carlo simulation (Dots for data, circles for MC). Bottom: Data minus the simulation.

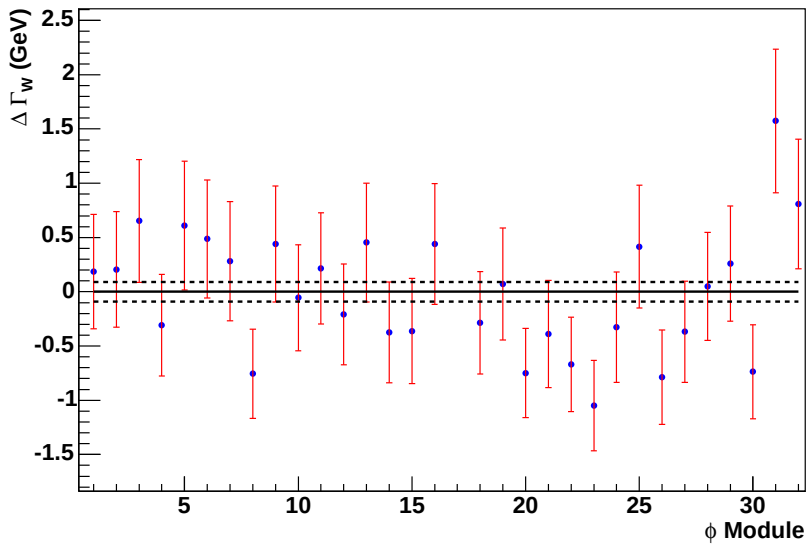

Figure 9.14: Variation in the fitted W width as a function of ϕ module (x axis is ϕ module, defined as (int)$(32 \times \phi^{elec}_{det}/2\pi)$).

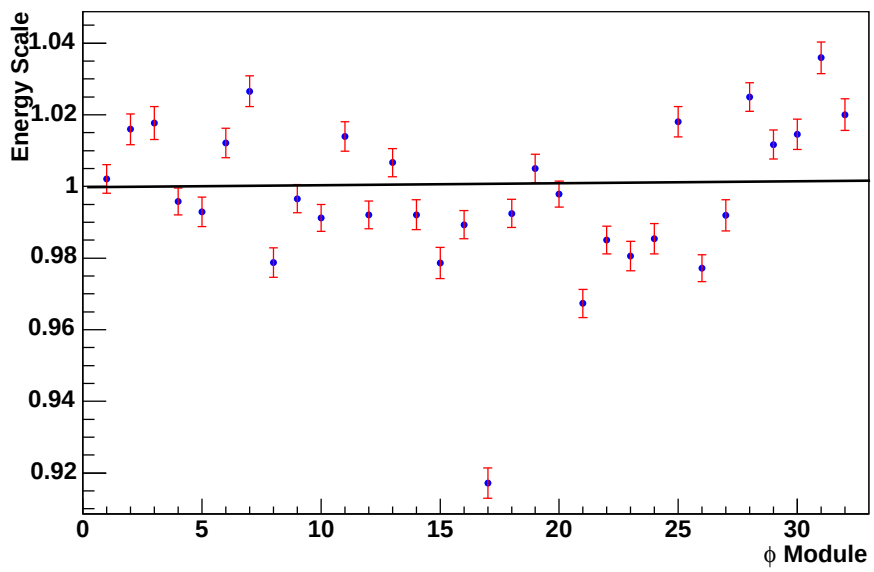

Figure 9.15: Electron energy scale as a function of ϕ module (y axis is ϕ module, defined as (int)$(32 \times \phi^{e}_{det}/2\pi)$).

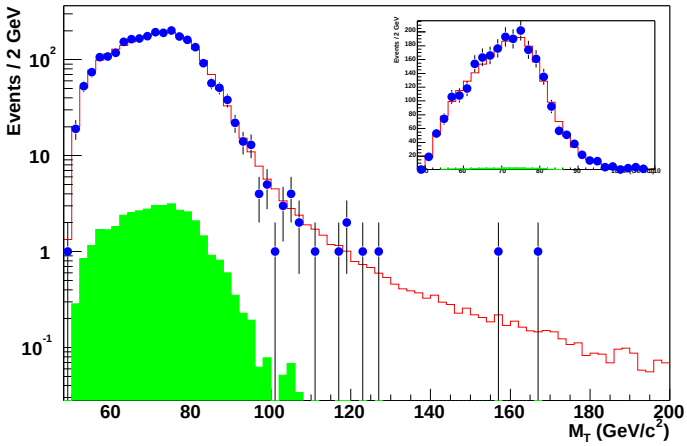

Figure 9.16: M_T data and the Monte Carlo comparison for one typical module (Module 18).

Chapter 10

Conclusions and Future Prospects

In this dissertation, we describe a direct measurement of the W boson total decay width Γ_W, using 117.3 pb^{-1} data collected at DØ during the Tevatron 2002 - 2003 run. The result is $\Gamma_W = 2.011 \pm 0.093$ (stat) ± 0.107 (syst) $= 2.011 \pm 0.142$ GeV. Compared with our Run I measurement, $\Gamma_W = 2.231 \pm 0.172$ GeV, done with 85 pb^{-1} data collected at Run Ib, the total uncertainty has decreased by about 30 MeV. Figure 10.1 shows the W boson width results compared with the SM prediction, as well as with previous measurements. Our result is consistent with the SM and shows no evidence of new physics.

This analysis has a large statistical uncertainty, with an expectation of about 2 fb^{-1} in the Run II, we will have at least 10 times more W's and Z's. Assuming the statistical uncertainty scales as $1/\sqrt{N} \propto 1/\sqrt{L}$, the statistical uncertainty will reduce to around 30 MeV for 2 fb^{-1} of data. Due to the rapid decrease of M_T in the tail region, only a small fraction of the events can be used for fitting. In the $W \to e\nu$ sample used in this analysis, we have 625 events with $100 < M_T < 200$ GeV (0.81%) and 2,356 events with $90 < M_T < 200$ GeV (3.10%). In Run I, the fitting region was chosen to be 90 - 200 GeV to have more events in the high tail region. Since currently the performance of the calorimeter is worse than Run I, we decided to choose the fitting region to be 100 - 200 GeV to avoid the transverse mass region affected by the calorimeter energy resolution. Now we are working on a more precise calibration of our calorimeter, and we have already found several sources that contribute to the large constant term. We expect that we can recover the Run I calorimeter performance within the next year or two. After that, we may be able to use the Run I fitting region to get a smaller statistical uncertainty of about 20 MeV. In addition, it should also be possible for DØ to make this measurement in muon channel, reducing the statistical error even further.

The biggest systematic uncertainties for the W width measurement come from our understanding

of the response and resolution of the electromagnetic and hadronic calorimeters, the underlying event contribution and the production model. These effects are parameterized in the Monte Carlo simulation, where most of these parameters were determined using $Z \to ee$ data. With at least 10 times more Z's, we should be able to determine these parameters more accurately. Also, we require each electron to have a matched track for the $Z \to ee$ candidates used for the calibration of the Monte Carlo simulation. In the future, we can relax this to at least one track match for the two electrons, which will increase the $Z \to ee$ size by about 20%, though the QCD background will also increase to about 5%. If all systematic uncertainties scale as $1/\sqrt{N}$ [1], the total systematic uncertainty is expected to be around 40 MeV for 2 fb^{-1}.

Work is currently being done to try to reduce the theoretical uncertainties arising from NLO electroweak corrections, p_T^W modeling [2] and the PDF's [3], and these uncertainties are also expected to be reduced significantly within several years.

One of the most important measurements that can be done at the Tevatron is to determine the W boson mass, which can be used together with the measured top mass to constrain the unobserved Higgs mass (discussed in Sec. 1.3.2). The W mass measurement uses the same method as the W width measurement (discussed in Sec. 1.4); by performing the width measurement, we have gained more understanding of the performance of the DØ detector and the systematic uncertainties for the W mass measurement.

[1] the only source of uncertainties in this measurement not expected to scale statistically with the size of the data set is from parton distribution functions (PDF).

[2] increase in the number of $Z \to ee$ events will help us to constrain the p_T^W model.

[3] use W charge asymmetry to constrain PDF sets.

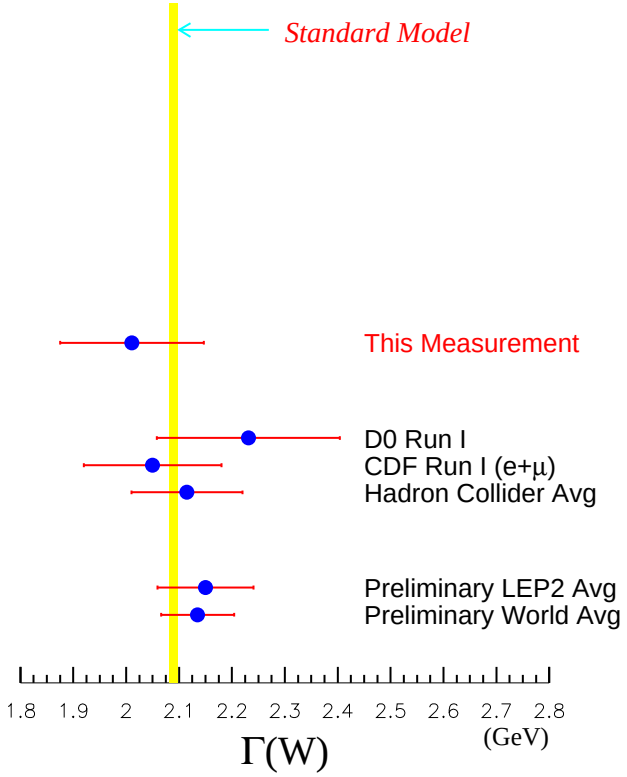

Figure 10.1: Comparison of this measurement with previously published direct measurements of the W boson width, the shaded region indicates the predicted W width value.

Appendix A

Discussion about the Constant Term

Unfortunately, compared with Run I, the CC EM calorimeter has poor energy resolution, the constant term is 4.2% in Run II compared with 1.6% in Run I. Since the constant term reflects how well we understand and calibrate the entire calorimeter, there are many sources that contribute to the constant term. I will use this appendix to discuss the possible sources and the work we are currently doing to improve the constant term.

A.1 Electronics Noise

A.1.1 Design Goal

The main design goals for the Run II calorimeter electronics were to minimize the noise contributions in the new environment and to maintain the calorimeter readout performance. The shorter shaping time in Run II (from 2.2 μs to 400 ns) increases the electronics noise by a factor that scales as $1/\sqrt{t} = 2.3$. The two FET inputs of the preamplifier give a reduction of $\sqrt{N_{FET}} = \sqrt{2}$, the electronics noise performance is expected to be about 1.6 times that for Run I. The shorter shaping time decreases the contribution from the uranium noise and from the pile-up effects by a factor of 2.3. The pile-up contribution also increases with the higher instantaneous luminosity as $\sqrt{L}$ (about a factor of 3), so the noise contribution due to pile-up will increase by a factor of $3 \times 1/2.3 = 1.3$. The overall noise performance expected is about the same as that for Run I.

A.1.2 Electronics Calibration

As mentioned in Sec. 6.1, we measured the response of each channel using the pulser signal. There are several differences between the calibration signal and the physical signal. For example, it is not possible to generate a calibration signal which accurately mimics the physical signal, the

Electronics noise: $\uparrow \times 1.6$	$\uparrow \times 2.3$ Shaping time (2 μ s $\rightarrow$ 400 ns) ($\sim \sqrt{t}$)
	$\downarrow \div \sqrt{2}$ Lower noise preamp (2 FET) ($\sim 1/\sqrt{N_{FET}}$)
Uranium noise: $\downarrow \div 2.3$	$\downarrow \div 2.3$ Shorter shaping time ($\sim \sqrt{t}$)
Pile-up noise: $\uparrow \times 1.3$	$\uparrow \times 3$ Luminosity ($\sim \sqrt{L}$)
	$\downarrow \div 2.3$ Shorter shaping time ($\sim \sqrt{t}$)

Table A.1: Electronics Noise Performance.

physical signal is a triangle signal with $\sim$ 400 ns drift time, while the calibration signal is an exponential signal with a short decay time. Moreover, due to reflection, the calibration signal is more sensitive than the physics signal to cable length and cell capacitance variations. Thus, it is almost impossible to simulate exactly the physics signal using the calibration signal. Even though a complete simulation of the calibration signal and physical signal shapes exists [64], we still can not correct the variation of the physical signal with an accuracy better than 1%.

We tuned the timing to sample the shaped calorimeter signal at its peak. The timing measurement was done by taking 3 samples of the same signal, with the nominal peak sample taken at the point defined by the trigger, an early sample taken 132 ns earlier and a late one 132 ns later. By comparing the ratios of these three samples with a simulated model, we can accurately determine the nominal sampling position with respect to the shaped signal peak. We have measured that the channel-to-channel variation of the nominal sampling time is less than 10 ns, which implies less than 0.1% variation in the peak sampled value due to timing differences [74].

A.1.3 Coherent Noise

Coherent noise will also contribute to the constant term, when summing up the readout of a large number of channels. Initial measurements have been performed to check this in the readout electronics. The idea is the variance of the sum of two or more random variables is equal to the sum of each of their variances only when the random variables are independent, $\sigma^2_{x+y} = \sigma^2_x + \sigma^2_y$.

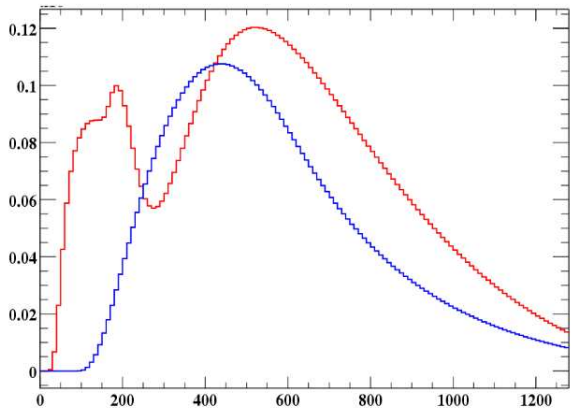

Figure A.1: Comparison of physical signal (the histogram with only one peak) and calibration signal (the histogram with two peaks).

However, if there is some correlation between variables, then the variance will be $\sigma^2_{x+y} = \sigma^2_x + 2\sigma_{xy} + \sigma^2_y$, thus we can quantify the correlation by comparing the sum of the individual variances to the whole. Pedestal data were recorded during a pedestal run and analyzed to measure the individual channel noise and the channel-to-channel correlated noise. The distribution of correlation coefficients for pairs of channels in one BLS crate is shown in Fig. A.2. These coefficients follow a mostly Gaussian distributions with a width ~ 0.07 for a 2,000 event run [75]. There are still some deviations from the Gaussian, which implied that the coherent noise between channels still exists.

A.2 Operation and Maintenance

During the data taking period, we regularly check the entire readout by checking the mean values of pedestals and the noise for every channel, as well as the response of every channel to the injected calibration pulses. Efforts are made to fix bad channels and maintain the percentage of bad channels within 0.1%. These are channels randomly distributed over the entire detector and are suppressed during data taking.

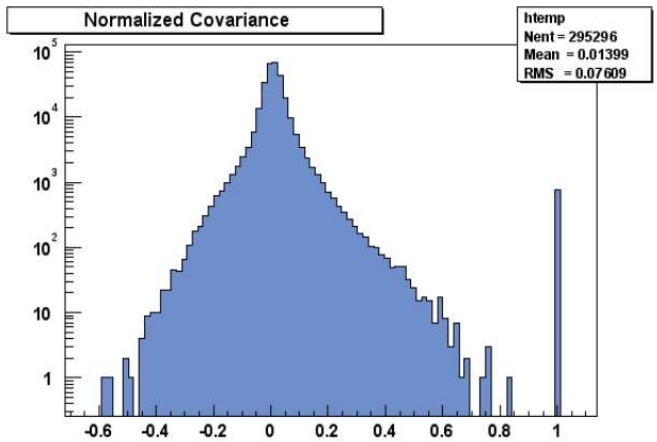

Figure A.2: Normalized pair-wise correlation coefficients based on pedestal ADC counts for all 4608 channels in one ADC crate.

A.2.1 Liquid Argon Monitoring

The purity of the liquid argon is critical to the detector performances as electronegative contaminants (e.g. oxygen and nitrogen) can combine with electrons traversing the gap and can severely impact the energy measurement. Radioactive sources are used to monitor these level. Each of the three calorimeter cryostats is equipped with four ^{241}Am sources with an activity of 0.1 μCi and four ^{106}Ru sources. Three of the beta sources in each cryostat now have very low levels of activity ($\leq$ 1 Bq), ten years after the initial detector construction. One slightly stronger source has an activity of about 4 Bq [40].

A.2.2 Hardware Problems

During the three years' run, we fixed many problems with the calorimeter hardware, but we also introduced some new problems: Energy Sharing problem [76], Tower 2 problem [77], calorimeter cable swap, etc. These problems are most related to the electronics and affects a large fraction of the data used for this analysis. As an example, Fig. A.3 shows the electron candidate η_{det} vs ϕ_{det} distribution for runs 179762 to 180956. Some calorimeter regions are not working or at least not working properly. For these analysis, if an electrons is located at these regions, the whole event is

not used. This will not affect the electron energy resolution, but since it definitely has an effect on $\not\!\!E_T$ resolution. Fortunately, most problems can be fixed or partially fixed offline.

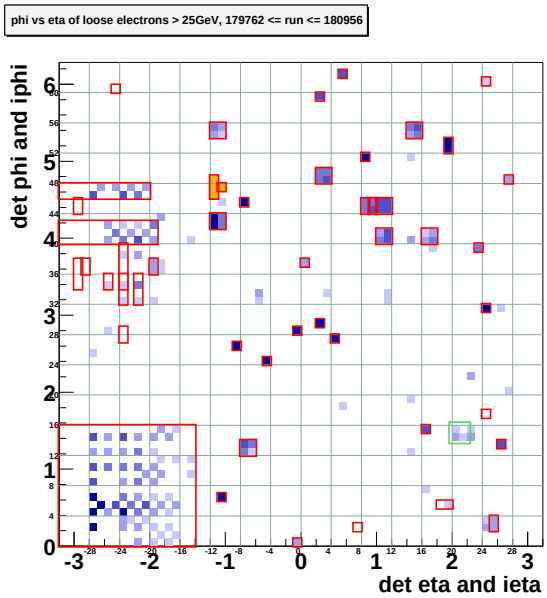

Figure A.3: η_{det} vs ϕ_{det} calorimeter plots for runs 179762 to 180956. Hollow boxes are regions cut out, blue solid boxes are inefficient cells (lightest $< 60\%$ normal, darkest $< 20\%$), orange have at least twice normal acceptance.

A.3 Clustering Algorithms and T42

The clustering algorithm used in this analysis is the Simple Cone algorithm (SC), and there is another energy flow algorithm (CellNN) [78] available in DØ. The energy flow algorithm is designed to reconstruct the flow of energy in an event, producing a list of energy flow particles. Instead of using a fixed cone size in SC algorithm, CellNN clusterize cells layer by layer and then builds cluster by association of the floor clusters. It is particularly powerful for reconstructing electrons inside a jet. The CellNN calibration is derived from single particle MC events. Initial studies have been performed and showed that calibrated CellNN algorithm has almost the same EM resolution as the SC algorithm.

The performance of these two algorithms is strongly influenced by the quantity of noise cells

present in the event. The number of noise cells depends on the zero-suppression cuts applied online and offline. For this analysis, we use 2.0 σ online and 2.5 σ offline, and very recently people proposed using an algorithm from H1 experiment called the T42 algorithm, which makes use of two thresholds, typically 4 and 2 sigma. The primary objective of the algorithm is to discard isolated low energy cells, since they are associated to first approximation with noisy cells. For the T42 algorithm, an isolated cell is considered "noise" and thus discarded if it is not "signal-like" and if it has no "signal-like" 3-d neighbor, or if it has a negative energy. A cell is considered "signal-like" if its energy is above a relatively high threshold: $+4\sigma$ typically [79]. The T42 algorithm is found to improve the jet energy resolution significantly, but gives only a very small improvement on the electron energy resolution. Figure A.4 shows the invariant mass distribution for electrons from $Z \to ee$ events with and without the T42 algorithm applied; the Z width only changes from 3.58 GeV to 3.55 GeV. The resolution of the missing transverse energy improves 4.91 GeV to 4.68 GeV, and the x and y components of $\not{E}_T$ are becoming more centered [80].

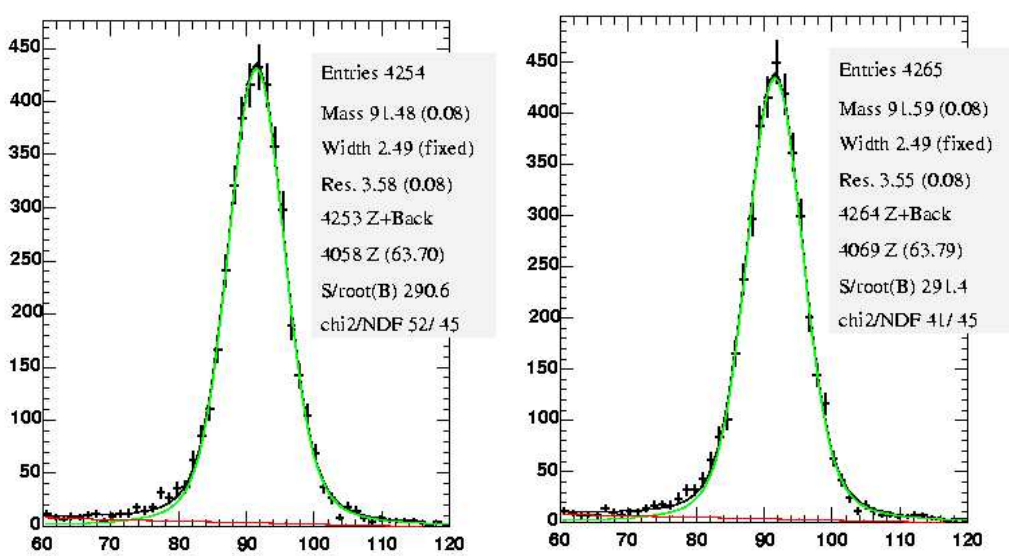

Figure A.4: Invariant Mass distribution for $Z \to ee$ events without (Left) and with (Right) T42 algorithm.

A.4 Offline Calibration

A.4.1 Calorimeter non-uniformity and ϕ intercalibration

As can be seen in Sec.9.8, the response of the 32 central EM modules are not uniform, and this will have a significant effect on the constant term. Further studies showed that within each module, the response for each ADC card is different. For example, Fig. A.5 shows the average E/p distribution for electrons from W decays inside each ADC card within four different ADC crates [81]. A large dispersion within each crate is seen.

Calorimeter non-uniformity studies are currently undergoing, which look at minimum bias events using the so-called "ϕ intercalibration" method. The goal is to obtain a better than 1% calibration. One of the reasons we choose to use minimum bias events is because there are plenty of them, but the disadvantage is that the energy deposition per cell is typically 50-100 MeV, and it is hard to give conclusive results when extrapolate these to high energy. The idea of ϕ calibration is based on the fact that since the $p\bar{p}$ beams in the Tevatron are not polarized. Therefore, the energy flow in the direction transverse to the $p\bar{p}$ beams should not have any azimuthal dependence. Any ϕ dependence must be the result of instrumental effects. By applying energy scale corrections for each cell, we can equalize the average energy in each ϕ module. Currently this study is one of the most highest priority projects in DØ [82].

A.5 Preshower Detectors

With the introduction of the solenoid and the preshower lead converters into the cavity of the DØ tracker, the amount of material a particle encounters before hitting the first layer of the central calorimeter has increased significantly. Therefore to optimize the energy response, the contributions from the preshowers must be included. Figure A.6 shows the improvement of the energy reconstruction for soft electrons with $E_T = 2$ GeV, comparing the reconstruction with and without the CPS detector. Since the CPS and FPS detectors are still under commissioning, the energy deposited in the preshower detector is still not included in this analysis. Once we have

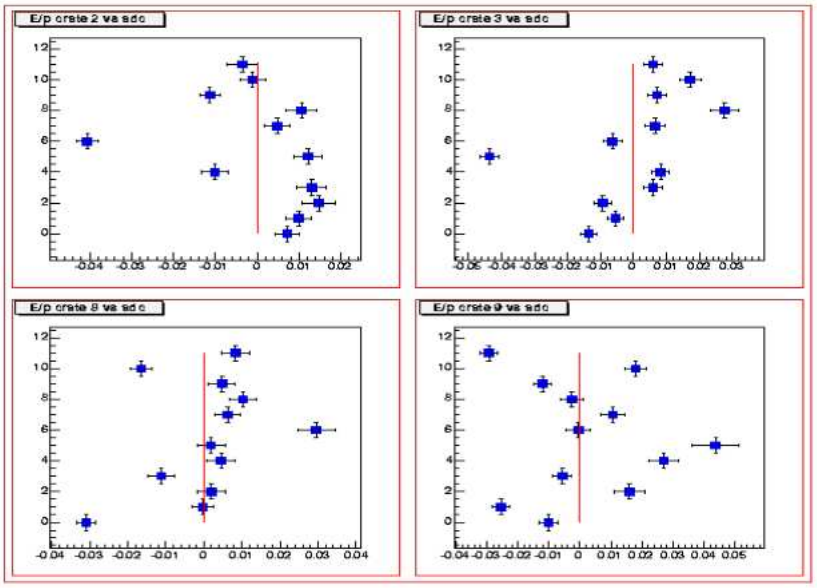

Figure A.5: E/p distribution for electrons from $W \to e\nu$ candidates for crate 2 (Top Left), crate 3 (Top Right), Crate 8 (Bottom Left) and Crate 9 (Bottom Right). Each point represents the average E/p for electrons located inside one of twelve ADC cards within one ADC crate.

more understanding of the preshower detector performance, we hope that the electron energy resolution will be improved.

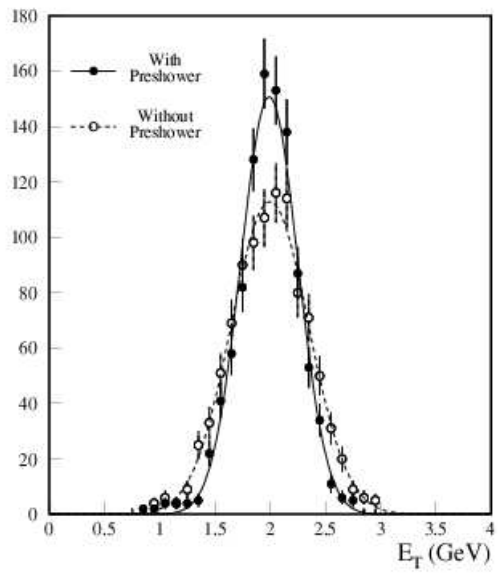

Figure A.6: Simulation of the improvement obtained on the electron energy resolution with the DØ calorimeter including the Central Preshower detector for electrons at $E_T = 2$ GeV.

Appendix B

E/p Simulation

Calorimeter non-uniformity and calorimeter non-linearity are determined from a lineshape comparison of the observed E/p distribution for electrons from $W \to e\nu$ to a Monte Carlo prediction of this distribution [83]. The electron may lose energy to photons either as it is created from the W decay (internal bremsstrahlung) or as it passes through material (external bremsstrahlung). Since the associated photons are usually collinear with the electron, they often form one EM cluster in the calorimeter, so that the energy response is relatively unaffected by the bremsstrahlung process, while the electron momentum p measured by the tracker is typically lower than the electron energy E measured by the calorimeter, producing the long tail in E/p. We divide the E/p distribution into three regions: the low E/p region ($E/p < 0.9$), peak region ($0.9 < E/p < 1.2$) and the high E/p region ($E/p > 1.2$). For events in the low E/p region, the p_T measured by the tracker is mis-measured. Figure B.1 shows the M_T distributions for events with $E/p < 0.9$ (using calorimeter E_T and tracker p_T) superimposed on events with E/p in the peak. The similarity of the two histograms (red dots and black line) indicates that events in the low-end E/p tail are not background events, and it also indicates that the low-end E/p tail is not a result of E_T mismeasurement. The histogram with blue triangles is the M_T distribution calculated using p_T instead of E_T. Since M_T (Cal) for the low E/p events is not shifted, we expecte that M_T (track) is. From Figure B.1, the low-end events are clearly shifted toward higher M_T (track), which indicates that the low E/p events are the result of p_T being mismeasured high.

As mentioned before, the high tail is due to the bremsstrahlung, and we also use a fast Monte Carlo to simulate this bremsstrahlung process as described by Tsai [84]. Electrons are stepped through the material from the beam line through the SMT and CFT, and we randomly choose at each step whether a bremsstrahlung occurred or not. If we step through dt radiation length, then

the probability of creating a bremsstrahlung photon is given by:

$$dt \times \int_{y_{min}=0.001}^{1} p(y)dy \tag{B.1}$$

where y is the fraction of the electron energy given up to the photon, and y_{min} is the minimum value of y we choose to simulate. $p(y)$ is the distribution of y and is given by

$$p(y) = \frac{(1-y)(\frac{4}{3}+3\%)+y^2}{y} \tag{B.2}$$

If we decide that a photon bremsstrahlung occurred, then we generate a photon which takes away the fraction of the electron energy given by y, where y is generated according to $p(y)$. We then adjust the track p_T and continue stepping through the material.

Since we do not know material distribution for Beampipe+SMT+CFT yet, the amount of material is measured from the size of the E/p "tail" relative to the "peak". The value of

$$\frac{\text{number of events with } 1.3 < E/p < 1.8}{\text{number of events with } 0.9 < E/p < 1.2} \tag{B.3}$$

is measured to be $(18.767 \pm 0.173)\%$ in data. For the simulation to reproduce this tail, the amount of material should be 26.5% radiation lengths.

One may also look for anomalous behavior of the amount of material for different ranges of electron E_T. A significant disagreement could indicate inadequate modeling of the electron E_T spectrum, the bremsstrahlung and/or the tracker p_T measurment. Table B.1 compares the tail fraction between data and Monte Carlo simulation for six electron E_T regions, there is no significant pattern of disagreement between data and simulation.

For events in the peak region, the peak position is determined by the electron energy scale and track momentum response, the width is determined by the electron energy resolution and track momentum resolution. The electron energy scale and energy resolution are determined as before using the maximum likelihood method, the track momentum response and track momentum resolution are determined using $J/\psi \to \mu\mu$ and $Z \to \mu\mu$ events [85]:

$$\frac{\sigma_{1/p_T}}{1/p_T} = \sqrt{A^2\frac{p_T^2}{L^4} + \frac{B^2}{Lsin(\theta)}} \tag{B.4}$$

$$p_T(\text{final}) = p_T(\text{smear})/C \tag{B.5}$$

Range (GeV)	ratio(data)(%)	ratio(simulation)(%)
$25 \leq E_T < 30$	15.59 ± 0.42	15.10 ± 0.33
$30 \leq E_T < 35$	16.64 ± 0.33	16.30 ± 0.26
$35 \leq E_T < 40$	17.25 ± 0.30	16.87 ± 0.23
$40 \leq E_T < 45$	20.34 ± 0.42	20.11 ± 0.33
$45 \leq E_T < 50$	24.57 ± 0.81	23.91 ± 0.66
$E_T > 55$	33.68 ± 0.97	32.25 ± 0.78

Table B.1: Energy dependence of the size of the tail of E/p spectrum relative to its peak.

and $A = 0.00277 \pm 0.00010$, $B = 0.0258 \pm 0.0008$ and $C = 1.008 \pm 0.002$.

Figure 6.15 shows the E/p lineshape comparison between data and Monte Carlo Simulation. Good agreement between data and MC simulation is observed.

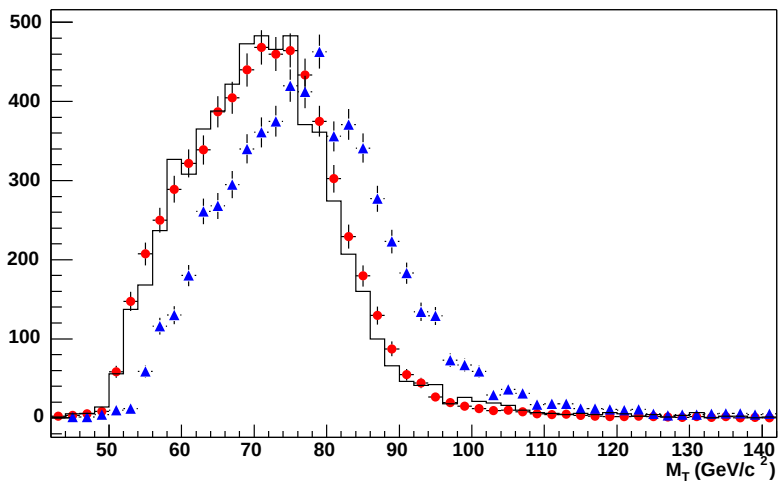

Figure B.1: M_T distributions for W events (Dots for events in peak region, line for events in low E/p region (Using calorimeter E_T) and triangles for events in low E/p region (Using tracke p_T) The histograms are normalized to the number of events with $E/p < 0.9$.

Appendix C

DØ Author List

V.M. Abazov,[33] B. Abbott,[70] M. Abolins,[61] B.S. Acharya,[27] M. Adams,[48] T. Adams,[46] M. Agelou,[17] J.-L. Agram,[18] S.H. Ahn,[29] M. Ahsan,[55] G.D. Alexeev,[33] G. Alkhazov,[37] A. Alton,[60] G. Alverson,[59] G.A. Alves,[2] M. Anastasoaie,[32] S. Anderson,[42] B. Andrieu,[16] Y. Arnoud,[13] A. Askew,[74] B. Åsman,[38] O. Atramentov,[53] C. Autermann,[20] C. Avila,[7] F. Badaud,[12] A. Baden,[57] B. Baldin,[47] P.W. Balm,[31] S. Banerjee,[27] E. Barberis,[59] P. Bargassa,[74] P. Baringer,[54] C. Barnes,[40] J. Barreto,[2] J.F. Bartlett,[47] U. Bassler,[16] D. Bauer,[51] A. Bean,[54] S. Beauceron,[16] M. Begel,[66] A. Bellavance,[63] S.B. Beri,[26] G. Bernardi,[16] R. Bernhard,[47,*] I. Bertram,[39] M. Besançon,[17] R. Beuselinck,[40] V.A. Bezzubov,[36] P.C. Bhat,[47] V. Bhatnagar,[26] M. Binder,[24] K.M. Black,[58] I. Blackler,[40] G. Blazey,[49] F. Blekman,[31] S. Blessing,[46] D. Bloch,[18] U. Blumenschein,[22] A. Boehnlein,[47] O. Boeriu,[52] T.A. Bolton,[55] F. Borcherding,[47] G. Borissov,[39] K. Bos,[31] T. Bose,[65] A. Brandt,[72] R. Brock,[61] G. Brooijmans,[65] A. Bross,[47] N.J. Buchanan,[46] D. Buchholz,[50] M. Buehler,[48] V. Buescher,[22] S. Burdin,[47] T.H. Burnett,[76] E. Busato,[16] J.M. Butler,[58] J. Bystricky,[17] W. Carvalho,[3] B.C.K. Casey,[71] N.M. Cason,[52] H. Castilla-Valdez,[30] S. Chakrabarti,[27] D. Chakraborty,[49] K.M. Chan,[66] A. Chandra,[27] D. Chapin,[71] F. Charles,[18] E. Cheu,[42] L. Chevalier,[17] D.K. Cho,[66] S. Choi,[45] T. Christiansen,[24] L. Christofek,[54] D. Claes,[63] B. Clément,[18] C. Clément,[38] Y. Coadou,[5] M. Cooke,[74] W.E. Cooper,[47] D. Coppage,[54] M. Corcoran,[74] J. Coss,[19] A. Cothenet,[14] M.-C. Cousinou,[14] S. Crépé-Renaudin,[13] M. Cristetiu,[45] M.A.C. Cummings,[49] D. Cutts,[71] H. da Motta,[2] B. Davies,[39] G. Davies,[40] G.A. Davis,[50] K. De,[72] P. de Jong,[31] S.J. de Jong,[32] E. De La Cruz-Burelo,[30] C. De Oliveira Martins,[3] S. Dean,[41] F. Déliot,[17] P.A. Delsart,[19] M. Demarteau,[47] R. Demina,[66] P. Demine,[17] D. Denisov,[47] S.P. Denisov,[36] S. Desai,[67] H.T. Diehl,[47] M. Diesburg,[47] M. Doidge,[39] H. Dong,[67] S. Doulas,[59] L. Duflot,[15] S.R. Dugad,[27] A. Duperrin,[14] J. Dyer,[61] A. Dyshkant,[49] M. Eads,[49] D. Edmunds,[61] T. Edwards,[41] J. Ellison,[45] J. Elmsheuser,[24]

J.T. Eltzroth,[72] V.D. Elvira,[47] S. Eno,[57] P. Ermolov,[35] O.V. Eroshin,[36] J. Estrada,[47] D. Evans,[40] H. Evans,[65] A. Evdokimov,[34] V.N. Evdokimov,[36] J. Fast,[47] S.N. Fatakia,[58] L. Feligioni,[58] T. Ferbel,[66] F. Fiedler,[24] F. Filthaut,[32] W. Fisher,[64] H.E. Fisk,[47] M. Fortner,[49] H. Fox,[22] W. Freeman,[47] S. Fu,[47] S. Fuess,[47] T. Gadfort,[76] C.F. Galea,[32] E. Gallas,[47] E. Galyaev,[52] C. Garcia,[66] A. Garcia-Bellido,[76] J. Gardner,[54] V. Gavrilov,[34] P. Gay,[12] D. Gelé,[18] R. Gelhaus,[45] K. Genser,[47] C.E. Gerber,[48] Y. Gershtein,[71] G. Ginther,[66] T. Golling,[21] B. Gómez,[7] K. Gounder,[47] A. Goussiou,[52] P.D. Grannis,[67] S. Greder,[18] H. Greenlee,[47] Z.D. Greenwood,[56] E.M. Gregores,[4] Ph. Gris,[12] J.-F. Grivaz,[15] L. Groer,[65] S. Grünendahl,[47] M.W. Grünewald,[28] S.N. Gurzhiev,[36] G. Gutierrez,[47] P. Gutierrez,[70] A. Haas,[65] N.J. Hadley,[57] S. Hagopian,[46] I. Hall,[70] R.E. Hall,[44] C. Han,[60] L. Han,[41] K. Hanagaki,[47] K. Harder,[55] R. Harrington,[59] J.M. Hauptman,[53] R. Hauser,[61] J. Hays,[50] T. Hebbeker,[20] D. Hedin,[49] J.M. Heinmiller,[48] A.P. Heinson,[45] U. Heintz,[58] C. Hensel,[54] G. Hesketh,[59] M.D. Hildreth,[52] R. Hirosky,[75] J.D. Hobbs,[67] B. Hoeneisen,[11] M. Hohlfeld,[23] S.J. Hong,[29] R. Hooper,[71] P. Houben,[31] Y. Hu,[67] J. Huang,[51] I. Iashvili,[45] R. Illingworth,[47] A.S. Ito,[47] S. Jabeen,[54] M. Jaffré,[15] S. Jain,[70] V. Jain,[68] K. Jakobs,[22] A. Jenkins,[40] R. Jesik,[40] K. Johns,[42] M. Johnson,[47] A. Jonckheere,[47] P. Jonsson,[40] H. Jöstlein,[47] A. Juste,[47] M.M. Kado,[43] D. Käfer,[20] W. Kahl,[55] S. Kahn,[68] E. Kajfasz,[14] A.M. Kalinin,[33] J. Kalk,[61] D. Karmanov,[35] J. Kasper,[58] D. Kau,[46] R. Kehoe,[73] S. Kermiche,[14] S. Kesisoglou,[71] A. Khanov,[66] A. Kharchilava,[52] Y.M. Kharzheev,[33] K.H. Kim,[29] B. Klima,[47] M. Klute,[21] J.M. Kohli,[26] M. Kopal,[70] V.M. Korablev,[36] J. Kotcher,[68] B. Kothari,[65] A. Koubarovsky,[35] A.V. Kozelov,[36] J. Kozminski,[61] S. Krzywdzinski,[47] S. Kuleshov,[34] Y. Kulik,[47] S. Kunori,[57] A. Kupco,[17] T. Kurča,[19] S. Lager,[38] N. Lahrichi,[17] G. Landsberg,[71] J. Lazoflores,[46] A.-C. Le Bihan,[18] P. Lebrun,[19] S.W. Lee,[29] W.M. Lee,[46] A. Leflat,[35] F. Lehner,[47,*] C. Leonidopoulos,[65] P. Lewis,[40] J. Li,[72] Q.Z. Li,[47] J.G.R. Lima,[49] D. Lincoln,[47] S.L. Linn,[46] J. Linnemann,[61] V.V. Lipaev,[36] R. Lipton,[47] L. Lobo,[40] A. Lobodenko,[37] M. Lokajicek,[10] A. Lounis,[18] H.J. Lubatti,[76] L. Lueking,[47] M. Lynker,[52] A.L. Lyon,[47] A.K.A. Maciel,[49] R.J. Madaras,[43] P. Mättig,[25] A. Magerkurth,[60] A.-M. Magnan,[13] N. Makovec,[15] P.K. Mal,[27] S. Malik,[56] V.L. Malyshev,[33] H.S. Mao,[6] Y. Maravin,[47] M. Martens,[47] S.E.K. Mattingly,[71]

A.A. Mayorov,[36] R. McCarthy,[67] R. McCroskey,[42] D. Meder,[23] H.L. Melanson,[47]
A. Melnitchouk,[62] M. Merkin,[35] K.W. Merritt,[47] A. Meyer,[20] H. Miettinen,[74] D. Mihalcea,[49]
J. Mitrevski,[65] N. Mokhov,[47] J. Molina,[3] N.K. Mondal,[27] H.E. Montgomery,[47] R.W. Moore,[5]
G.S. Muanza,[19] M. Mulders,[47] Y.D. Mutaf,[67] E. Nagy,[14] M. Narain,[58] N.A. Naumann,[32]
H.A. Neal,[60] J.P. Negret,[7] S. Nelson,[46] P. Neustroev,[37] C. Noeding,[22] A. Nomerotski,[47]
S.F. Novaes,[4] T. Nunnemann,[24] E. Nurse,[41] V. O'Dell,[47] D.C. O'Neil,[5] V. Oguri,[3] N. Oliveira,[3]
N. Oshima,[47] G.J. Otero y Garzón,[48] P. Padley,[74] N. Parashar,[56] J. Park,[29] S.K. Park,[29]
J. Parsons,[65] R. Partridge,[71] N. Parua,[67] A. Patwa,[68] P.M. Perea,[45] E. Perez,[17] O. Peters,[31]
P. Pétroff,[15] M. Petteni,[40] L. Phaf,[31] R. Piegaia,[1] P.L.M. Podesta-Lerma,[30] V.M. Podstavkov,[47]
Y. Pogorelov,[52] B.G. Pope,[61] W.L. Prado da Silva,[3] H.B. Prosper,[46] S. Protopopescu,[68]
M.B. Przybycien,[50,†] J. Qian,[60] A. Quadt,[21] B. Quinn,[62] K.J. Rani,[27] P.A. Rapidis,[47]
P.N. Ratoff,[39] N.W. Reay,[55] S. Reucroft,[59] M. Rijssenbeek,[67] I. Ripp-Baudot,[18] F. Rizatdinova,[55]
C. Royon,[17] P. Rubinov,[47] R. Ruchti,[52] G. Sajot,[13] A. Sánchez-Hernández,[30] M.P. Sanders,[41]
A. Santoro,[3] G. Savage,[47] L. Sawyer,[56] T. Scanlon,[40] R.D. Schamberger,[67] H. Schellman,[50]
P. Schieferdecker,[24] C. Schmitt,[25] A.A. Schukin,[36] A. Schwartzman,[64] R. Schwienhorst,[61]
S. Sengupta,[46] H. Severini,[70] E. Shabalina,[48] M. Shamim,[55] V. Shary,[17] W.D. Shephard,[52]
D. Shpakov,[59] R.A. Sidwell,[55] V. Simak,[9] V. Sirotenko,[47] P. Skubic,[70] P. Slattery,[66]
R.P. Smith,[47] K. Smolek,[9] G.R. Snow,[63] J. Snow,[69] S. Snyder,[68] S. Söldner-Rembold,[41]
X. Song,[49] Y. Song,[72] L. Sonnenschein,[58] A. Sopczak,[39] M. Sosebee,[72] K. Soustruznik,[8]
M. Souza,[2] B. Spurlock,[72] N.R. Stanton,[55] J. Stark,[13] J. Steele,[56] G. Steinbrück,[65]
K. Stevenson,[51] V. Stolin,[34] A. Stone,[48] D.A. Stoyanova,[36] J. Strandberg,[38] M.A. Strang,[72]
M. Strauss,[70] R. Ströhmer,[24] M. Strovink,[43] L. Stutte,[47] S. Sumowidagdo,[46] A. Sznajder,[3]
M. Talby,[14] P. Tamburello,[42] W. Taylor,[5] P. Telford,[41] J. Temple,[42] S. Tentindo-Repond,[46]
E. Thomas,[14] B. Thooris,[17] M. Tomoto,[47] T. Toole,[57] J. Torborg,[52] S. Towers,[67] T. Trefzger,[23]
S. Trincaz-Duvoid,[16] B. Tuchming,[17] C. Tully,[64] A.S. Turcot,[68] P.M. Tuts,[65] L. Uvarov,[37]
S. Uvarov,[37] S. Uzunyan,[49] B. Vachon,[5] R. Van Kooten,[51] W.M. van Leeuwen,[31] N. Varelas,[48]
E.W. Varnes,[42] I.A. Vasilyev,[36] M. Vaupel,[25] P. Verdier,[15] L.S. Vertogradov,[33] M. Verzocchi,[57]

F. Villeneuve-Seguier,[40] J.-R. Vlimant,[16] E. Von Toerne,[55] M. Vreeswijk,[31] T. Vu Anh,[15] H.D. Wahl,[46] R. Walker,[40] L. Wang,[57] Z.-M. Wang,[67] J. Warchol,[52] M. Warsinsky,[21] G. Watts,[76] M. Wayne,[52] M. Weber,[47] H. Weerts,[61] M. Wegner,[20] N. Wermes,[21] A. White,[72] V. White,[47] D. Whiteson,[43] D. Wicke,[47] D.A. Wijngaarden,[32] G.W. Wilson,[54] S.J. Wimpenny,[45] J. Wittlin,[58] M. Wobisch,[47] J. Womersley,[47] D.R. Wood,[59] T.R. Wyatt,[41] Q. Xu,[60] N. Xuan,[52] R. Yamada,[47] M. Yan,[57] T. Yasuda,[47] Y.A. Yatsunenko,[33] Y. Yen,[25] K. Yip,[68] S.W. Youn,[50] J. Yu,[72] A. Yurkewicz,[61] A. Zabi,[15] A. Zatserklyaniy,[49] M. Zdrazil,[67] C. Zeitnitz,[23] D. Zhang,[47] X. Zhang,[70] T. Zhao,[76] Z. Zhao,[60] B. Zhou,[60] J. Zhu,[57] M. Zielinski,[66] D. Zieminska,[51] A. Zieminski,[51] R. Zitoun,[67] V. Zutshi,[49] E.G. Zverev,[35] and A. Zylberstejn[17]

[1]Universidad de Buenos Aires, Buenos Aires, Argentina

[2]LAFEX, Centro Brasileiro de Pesquisas Físicas, Rio de Janeiro, Brazil

[3]Universidade do Estado do Rio de Janeiro, Rio de Janeiro, Brazil

[4]Instituto de Física Teórica, Universidade Estadual Paulista, São Paulo, Brazil

[5]Simon Fraser University, Burnaby, Canada, University of Alberta, Edmonton, Canada, McGill University, Montreal, Canada and York University, Toronto, Canada

[6]Institute of High Energy Physics, Beijing, People's Republic of China

[7]Universidad de los Andes, Bogotá, Colombia

[8]Charles University, Center for Particle Physics, Prague, Czech Republic

[9]Czech Technical University, Prague, Czech Republic

[10]Institute of Physics, Academy of Sciences, Center for Particle Physics, Prague, Czech Republic

[11]Universidad San Francisco de Quito, Quito, Ecuador

[12]Laboratoire de Physique Corpusculaire, IN2P3-CNRS, Université Blaise Pascal, Clermont-Ferrand, France

[13]Laboratoire de Physique Subatomique et de Cosmologie, IN2P3-CNRS, Universite de Grenoble 1, Grenoble, France

[14]CPPM, IN2P3-CNRS, Université de la Méditerranée, Marseille, France

[15]Laboratoire de l'Accélérateur Linéaire, IN2P3-CNRS, Orsay, France

[16]LPNHE, Universités Paris VI and VII, IN2P3-CNRS, Paris, France

[17]DAPNIA/Service de Physique des Particules, CEA, Saclay, France

[18]IReS, IN2P3-CNRS, Université Louis Pasteur, Strasbourg, France and Université de Haute Alsace, Mulhouse, France

[19]Institut de Physique Nucléaire de Lyon, IN2P3-CNRS, Université Claude Bernard, Villeurbanne, France

[20]RWTH Aachen, III. Physikalisches Institut A, Aachen, Germany

[21]Universität Bonn, Physikalisches Institut, Bonn, Germany

[22]Universität Freiburg, Physikalisches Institut, Freiburg, Germany

[23]Universität Mainz, Institut für Physik, Mainz, Germany

[24]Ludwig-Maximilians-Universität München, München, Germany

[25]Fachbereich Physik, University of Wuppertal, Wuppertal, Germany

[26]Panjab University, Chandigarh, India

[27]Tata Institute of Fundamental Research, Mumbai, India

[28]University College Dublin, Dublin, Ireland

[29]Korea Detector Laboratory, Korea University, Seoul, Korea

[30]CINVESTAV, Mexico City, Mexico

[31]FOM-Institute NIKHEF and University of Amsterdam/NIKHEF, Amsterdam, The Netherlands

[32]University of Nijmegen/NIKHEF, Nijmegen, The Netherlands

[33]Joint Institute for Nuclear Research, Dubna, Russia

[34]Institute for Theoretical and Experimental Physics, Moscow, Russia

[35]Moscow State University, Moscow, Russia

[36]Institute for High Energy Physics, Protvino, Russia

[37]Petersburg Nuclear Physics Institute, St. Petersburg, Russia

[38]Lund University, Lund, Sweden, Royal Institute of Technology and Stockholm University, Stockholm, Sweden and Uppsala University, Uppsala, Sweden

[39]Lancaster University, Lancaster, United Kingdom

[40]Imperial College, London, United Kingdom

[41]University of Manchester, Manchester, United Kingdom

[42]University of Arizona, Tucson, Arizona 85721, USA

[43]Lawrence Berkeley National Laboratory and University of California, Berkeley, California 94720, USA

[44]California State University, Fresno, California 93740, USA

[45]University of California, Riverside, California 92521, USA

[46]Florida State University, Tallahassee, Florida 32306, USA

[47]Fermi National Accelerator Laboratory, Batavia, Illinois 60510, USA

[48]University of Illinois at Chicago, Chicago, Illinois 60607, USA

[49]Northern Illinois University, DeKalb, Illinois 60115, USA

[50]Northwestern University, Evanston, Illinois 60208, USA

[51]Indiana University, Bloomington, Indiana 47405, USA

[52]University of Notre Dame, Notre Dame, Indiana 46556, USA

[53]Iowa State University, Ames, Iowa 50011, USA

[54]University of Kansas, Lawrence, Kansas 66045, USA

[55]Kansas State University, Manhattan, Kansas 66506, USA

[56]Louisiana Tech University, Ruston, Louisiana 71272, USA

[57]University of Maryland, College Park, Maryland 20742, USA

[58]Boston University, Boston, Massachusetts 02215, USA

[59]Northeastern University, Boston, Massachusetts 02115, USA

[60]University of Michigan, Ann Arbor, Michigan 48109, USA

[61]Michigan State University, East Lansing, Michigan 48824, USA

[62]University of Mississippi, University, Mississippi 38677, USA

[63]University of Nebraska, Lincoln, Nebraska 68588, USA

[64]Princeton University, Princeton, New Jersey 08544, USA

[65]Columbia University, New York, New York 10027, USA

[66]University of Rochester, Rochester, New York 14627, USA

[67]State University of New York, Stony Brook, New York 11794, USA

[68]Brookhaven National Laboratory, Upton, New York 11973, USA

[69]Langston University, Langston, Oklahoma 73050, USA

[70]University of Oklahoma, Norman, Oklahoma 73019, USA

[71]Brown University, Providence, Rhode Island 02912, USA

[72]University of Texas, Arlington, Texas 76019, USA

[73]Southern Methodist University, Dallas, Texas 75275, USA

[74]Rice University, Houston, Texas 77005, USA

[75]University of Virginia, Charlottesville, Virginia 22901, USA

[76]University of Washington, Seattle, Washington 98195, USA

[*]Visitor from University of Zurich, Zurich, Switzerland

[†]Visitor from Institute of Nuclear Physics, Krakow, Poland

BIBLIOGRAPHY

[1] S.L. Glashow, Nucl. Phys. **B22** 579 (1961); A. Salam and J.C. Ward, Phys. Rev. Lett. **13** 168 (1994); S. Weinberg, Phys. Rev. Lett. **19** 1264 (1967).

[2] D. Karlen, Plenary talk "Experimental Status of the Standard Model" at the International Conference on High Energy Physics, ICHEP98, Cancouver, July 1998.

[3] Particle Data Group, Phys. Rev. **D66** (2002); V.M. Abazov *et al.*, DØ Collaboration, Nature **429**, 638 (2004).

[4] M. Herrero, "The Standard Model", hep-ph/9812242.

[5] D. Perkins, "Introduction to High Energy Physics".

[6] V. Barger and R. Phillips, "Collider Physics", Addison Wesley, 1993.

[7] E. Fermi, Nuovo Cimento 11 (1934); Z. Phys. **88** (1934).

[8] R.M. Barnett *et al.*, Phys. Rev. **54**, 1 (1996).

[9] CERN-PPE/95-172, LEP Electroweak Working Group, 1995.

[10] J. Collins, D. Soper, and G. Sterman, Nucl. Phys. **B250**, 199 (1985); J. Collins and D. Soper, Nucl. Phys. **B193**, 381 (1981); Nucl. Phys. **B197**, 446 (1982); Nucl. Phys. **B213**, 545(E) (1983).

[11] C. Davies, B. Webber, and W.J. Stirling, Nucl. Phys. **B256**, 413 (1985); C. Davies and W.J. Stirling, Nucl. Phys. **B244**, 337 (1984).

[12] P.B. Arnold and R. Kauffman, Nucl. Phys. **B349**, 381 (1991).

[13] G.A. Ladinsky and C.P. Yuan, Phys. Rev. **D50**, 4239 (1994).

[14] E. Mirkes, Nucl. Phys., **B387**, 3 (1992).

[15] G. Steinbruck, Ph.D. Thesis, University of Oklahoma, 1999, "Measurement of the Angular Distribution of Electrons from W Boson Decays at DØ" (unpublished).

[16] B. Abbott *et al.* (DØ Collaboration), Phys. Rev. Lett. **80** (1998); B. Abbott *et al.* (DØ Collaboration), Phys. Rev. **D58** (1998); B. Abbott *et al.* (DØ Collaboration), Phys. Rev. Lett. **84** (2000); B. Abbott *et al.* (DØ Collaboration), Phys. Rev. **D62** (2000); V. Abazov *et al.* (DØ Collaboration), Phys. Rev. **D66** (2002).

[17] U. Baur *et al.*, Phys. Rev. **D53** 1098 (1996); U. Baur *et al.*, Phys. Rev. **D57**, 199 (1998); U. Baur *et al.*, Phys. Rev. **D59**, 013002 (1999).

[18] T. Sjőstrand, L. Lőnnblad, S. Mrenna and P. Skands, PYTHIA 6.206, hep-ph/0108264.

[19] W. Beenakker *et al.*, "WW Cross Sections and Distributions" in "Physics at LEP-II"; G. Altarelli *et al.*, CERN 96-01, 70.

[20] The LEP Electroweak Working Group, http://lepewwg.web.cern.ch/LEPEWWG/plots/winter2004. R. Strőhmer, "Review of the Properties of the W Boson at LEP, and the Precision Determination of its Mass", hep-ph/0401146.

[21] D. Green, Lectures in Particle Physics;

[22] K. Hagiwara *et al.*, Phys. Rev. **D66** 010001 (2002).

[23] G. Arnison *et al.* (UA1 Collaboration), Phys. Lett. **B122** 102 (1983); M. Banner *et al.* (UA2 Collaboration), Phys. Lett. **B122** 476 (1983).

[24] F. Abe *et al.* (CDF Collaboration), Phys. Rev. **D52**, 2624 (1995); Phys. Rev. Lett. **76**, 3070 (1996).

[25] B. Abbott *et al.* (DØ Collaboration), Phys. Rev. **D60**, 052003 (1999).

[26] T. Affolder *et al.* (CDF Collaboration), Phys. Rev. Lett. **85**, 3347 (2000).

[27] V. M. Abozov *et al.* (DØ Collboration), Phys. Rev. **D66**, 032008 (2002).

[28] The CDF Collaboration and the DØ Collaboration, "Combination of CDF and DØ Results on W Boson Mass and Width".

[29] The LEP Collaborations ALEPH, DELPHI, L3, OPAL, the LEP Electroweak Working Group, the SLD Electroweak and Heavy Flavour Groups, hep-ex/0312023.

[30] Q. Xu *et al.*, DØ Note **3863**, "Direct Measurement of the W Boson Decay Width in $p\bar{p}$ Collisions at $\sqrt{s} = 1.8$ TeV".

[31] J. Thompson, "Introduction to Colliding Beams at Fermilab", FERMILAB-TM-1909 (1994); Run II Handbook, http://www-bd.fnal.gov/runII/; Accelerator Concepts, V3.0 (2002).

[32] S. Abachi *et al.* (DØ Collaboration), Nucl. Instr. and Methods, **A338**, 185 (1994).

[33] S. Abachi *et al.* (DØ Collaboration), Phys. Rev. Lett. **74**, 2632 (1995); F. Abe *et al.* (CDF Collaboration), Phys. Rev. Lett. **74**, 2626 (1995).

[34] DØ Collaboration, DØ Note **1996**, "The DØ Upgrade: The Detector and Its Physics"; V. Abazov *et al.* (DØ Collaboration), in preparation for submission to Nucl. Instr. and Methods.

[35] DØ Upgrade Collaboration, "DØ Silicon Tracker Technical Design Report", http://www-d0.fnal.gov/trigger/stt/smt/smt_tdr.ps.

[36] DØ Collaboration, DØ Note **4164**, "Central Fiber Tracker Technical Design Report".

[37] DØ Collaboration, DØ Note **3014**, "Design Report of the Central Preshower Detector for the DØ Upgrade".

[38] DØ Collaboration, DØ Note **2894**, "The DØ Upgrade: Forward Preshower, Muon System and Level 2 Trigger".

[39] S. Abachi *et al.* (DØ Collaboration), Nucl. Instr. and Methods, **A324**, 53 (1993).

[40] L. Groer, DØ Note **4240**, "DØ Calorimeter Upgrades for Tevatron Run II".

[41] DØ Collaboration, "Calorimeter Electronics", http://www-d0.fnal.gov/hardware/cal.

[42] R. Zitoun, DØ Note **3997**, "Study of the Non Linearity of the DØ Calorimeter Readout Chain"; J. Kotcher, "Upgrade Plans for the DØ Calorimeter"; J. Kourlas, "Calorimeter Electronics for the DØ Upgrade".

[43] Q. Zhu, Ph.D. thesis, New York University, 1994, "Measurement of the W Boson Mass in Proton-Antiproton Collisions at $\sqrt{s} = 1.8$ TeV" (unpublished).

[44] T.C. Heuring, Ph.D. thesis, State University of New York at Stony Brook, 1993, "Electrons in the DØ Calorimeter: A Study of the Systematic Biases in the Measurement of the W Mass" (unpublished).

[45] C. Brown *et al.* (DØ Collaboration), Nucl. Instr. and Methods, **A279** 331 (1989).

[46] DØ Collaboration, "DØ Run II Level 1 Trigger Framework Technical Design Report", http://www.pa.msu.edu/hep/d0/ftp/l1/framework/l1fw_tdr_05june98.txt.

[47] D. Edmunds *et al.*, DØ Note **3402**, "Technical Design Report for the Level 2 Global Processor".

[48] DØ Collaboration, DØ Note **3266**, "Description of DØ L3 Trigger Software".

[49] M. Adams et. al., DØ Note **3651**, "Level 2 Calorimeter Preprocessor Technical Design Report".

[50] DØ Integrated Luminosity: http://www-d0.fnal.gov/runcoor/runplans/runplan.html#plots; Tevatron Integrated Luminosity: http://www-d0.fnal.gov/runcoor/RUN/run2_lumi.html.

[51] http://www-d0.fnal.gov/computing/algorithms/calgo/jet_met/runsel.html.

[52] Jet/Met Group, "Run Selection version 3.0", http://www-d0.fnal.gov/d0upgrad/d0_private/software/jetid/jetid-certif.html.

[53] http://www-d0.fnal.gov/computing/algorithms/#intro.

[54] Application Software Group, "GEANT: Detector Description and Simulation Tool", CERN Program Library Long Writeup W5013, http://wwwasd.web.cern.ch/wwwasd/geant/.

[55] D. Chapin *et al.*, DØ Note **4403**, "Measurement of $Z \to ee$ and $W \to e\nu$ Production Cross Sections with $|\eta| < 2.3$".

[56] D. Adams, DØ Note **2958**, "Finding Tracks"; H. Greenlee, DØ Note **4303**, "The DØ Kalman Track Fit".

[57] A. Khanov, DØ Note **3778**, "HTF: histogramming method for finding tracks: The algorithm description". G. Hesketh, DØ Note **4079**, "Central Track Extrapolation Through the DØ Detector". H. Greenlee, DØ Note **4180**, "Motion of a Charged Particle in a Magnetic Field"; H. Greenlee, DØ Note **4293**, "The DØ Interacting Propagator".

[58] http://www-d0.fnal.gov/trigger/stt/doc/svtstat_970307/svtbeam.html.

[59] A. Schwartzman and M. Narain, DØ Note 3907, "Primary Vertex Selection".

[60] V. Buescher and J. Zhu, DØ Note **4171**, "em_cert: EM Certification Tools".

[61] S. Eno *et al.*, DØ Note **4097**, "Status of the Fast Simulatin PMCS, v01-96-00".

[62] R. Zitoun, http://www-d0.fnal.gov/hardware/cal/caltf/results/cal_noise_layer_eta.dat; http://www-d0.fnal.gov/hardware/cal/caltf/results/cal_zsup_noise_energy.dat.

[63] B. Abbott, DØ Note **2469**"Effects of Zero Suppression and Underlying Event on the Measured Jet Energies".

[64] P. Cornebise *et al.*, DØ Note **3731**, "Run II Calorimeter System"; R. Chiche *et al.*, DØ Note **3914**, "Optimisation of the D0 Online Calorimeter Calibration for RunII".

[65] K.M. Chan *et al.*, DØ Note **3535**, "Electron and Photon Energy Resolution".

[66] S. Crepe-Renaudin, DØ Note **4023**, "Energy corrections for geometry effects for electrons in Run II".

[67] A. Mendes and S. Kermiche, Talk at CALGO meeting (08/03/2004), "Status report on EM scale studies with $Z \to ee$".

[68] J. Zhu, DØ Note **4323**, "Determination of Electron Energy Scale and Energy Resolution using P14 $Z \to ee$ Data".

[69] T.C. Awes *et al.*, Nucl. Instr. and Meth. **A311**, 130 (1992).

[70] http://www-d0.fnal.gov/phys_id/jes/d0_private/certified/v4.2/note.ps.

[71] J. Alitti *et al.* (UA2 Collaboration), Phys. Lett. **B276**, 354 (1992).

[72] Ian Adam, Ph.D. thesis, Columbia University, 1997, "Measurement of the W Boson Mass with the DØ Detector Using the Electron Et Spectrum" (unpublished); Eric Flattum, Ph.D. thesis, Michigan State University, 1997, "A Measurement of the W Boson Mass in $p\bar{p}$ Collisions at 1.8 TeV" (unpublished).

[73] S. Alekhine, Phys. Rev. **D63** 094022 (2001).

[74] S. Fu, "Electronic Upgrade of the Run II DØ Calorimeter and the Performance", http://www-d0.fnal.gov/hardware/cal/talks/IEEE03CR_shfu.pdf.

[75] S. Fu and L. Groer, "Coherent Noise Studies", Calorimeter Operation Meeting, http://www-d0.fnal.gov/d̃0upgrade/d0_private/software/calorimeter/talks020423/.

[76] J. Stark, "Correction of the energy sharing problem in the calorimeter data", http://www-clued0.fnal.gov/s̃tark/esp_note.ps.

[77] J. Stark, "Correction of the tower two problem in the calorimeter data", http://www-clued0.fnal.gov/s̃tartk/tower2/note.ps.

[78] L. Duflot and M. Ridel, DØ Note **3927**, "An Energy Flow Algorithm for DØ".

[79] J.-R. Vlimant *et al.*, DØ Note **4146**, "Technical description of the T42 algorithm for the calorimeter noise suppression"; U. Bassler and G. Bernardi, DØ Note **4124**, "Towards a Coherent Treatment of Calorimeter Energies: Missing Transverse Energy, Jets, EM Objects and the T42 Algorithm".

[80] G. Bernardi *et al.*, DØ Note **4335**, "Improvements from the T42 Algorithm on Calorimeter Object Reconstruction".

[81] P. Petroff, Calorimeter Workshop, 2004, "What's wrong in the calorimeter?", http://www-d0.hef.kun.nl///askArchive.php?base=agenda&categ=a04823&id=a04823s8t15/transparencies.

[82] M. Wetstein, "ϕ Calibration studies", http://www-d0.hef.kun.nl///fullAgenda.php?ida=a041386.

[83] D.P. Saltzberg, Ph.D. thesis, University of Chicago, 1994, "Measurement of the W Boson Mass" (unpublished); A.S. Gordon, Ph.D. thesis, Harvard University, 2000, "Measurement of the W Boson Mass Width teh Collider Detector at Fermilab" (unpublished).

[84] Y.-S. Tsai, Rev. Mod. Phys., **45**, 815 (1974).

[85] P. Telford, L. Wang and N. Hadley, DØ Note **4297**, "Retuning of pmcs_chprt to P13 and P14 data".